

Electronic Thesis and Dissertation Repository

---

2-6-2018 2:30 PM

## Optimization of Design Procedures for Delta Relaxation Enhanced Magnetic Resonance

Daniel J. Martire, *The University of Western Ontario*

Supervisor: Chronik, Blaine A., *The University of Western Ontario*

A thesis submitted in partial fulfillment of the requirements for the Master of Science degree in Physics

© Daniel J. Martire 2018

Follow this and additional works at: <https://ir.lib.uwo.ca/etd>



Part of the [Medical Biophysics Commons](#), and the [Other Physics Commons](#)

---

### Recommended Citation

Martire, Daniel J., "Optimization of Design Procedures for Delta Relaxation Enhanced Magnetic Resonance" (2018). *Electronic Thesis and Dissertation Repository*. 5257.  
<https://ir.lib.uwo.ca/etd/5257>

This Dissertation/Thesis is brought to you for free and open access by Scholarship@Western. It has been accepted for inclusion in Electronic Thesis and Dissertation Repository by an authorized administrator of Scholarship@Western. For more information, please contact [wlsadmin@uwo.ca](mailto:wlsadmin@uwo.ca).

# Abstract

Delta relaxation enhanced magnetic resonance (dreMR) is a magnetic resonance imaging (MRI) method that produces contrast based on longitudinal relaxation dispersion. Through modulation of the magnetic field using an actively-shielded, field-cycling insert coil, this technique increases probe specificity and suppresses remaining signal. However, significant improvements are needed. This thesis addresses two advancements in dreMR with a focus on optimizing design procedures. A general procedure was developed to design split power solenoid magnets. The procedure was then applied to the design of a switched-field exposure system. A coil was constructed and the method was validated. This procedure can be used to optimize dreMR coil primary windings. Next, a simulation tool was developed to model tissue magnetization as a function of time and magnetic field. Polarization sequences were discovered that maximize dispersion-based contrast. These optimized design procedures may add to future developments in dreMR technology.

## Keywords

Magnetic resonance imaging; field-cycling; targeted contrast agent; relaxivity; delta relaxation enhanced MRI; solenoid magnet design; pulse sequence optimization; Bloch equation simulation; contrast-to-noise ratio; T1 dispersion.

## Acknowledgments

First and foremost, I would like to express my gratitude to my supervisor, Dr. Blaine Chronik, for his belief in me and for introducing me to this topic. The opportunity to work in this lab has been invaluable to my growth as a student and scientist.

To my fellow lab mates, thank you for all your support, laughs, and coffee chats. I wish you all the best in your research and professional endeavors. Thank you specifically to Will Handler and Colin McCurdy for assistance with coding and idea generation. Thank you to Brian Dalrymple, Frank Van Sas, Justin Peterson, and Ryan Chaddock for help with construction. Thank you to Yonathan Araya for your help with and long discussions of field-cycling research. Thank you to Tim Scholl and Tamie Poepping for serving on my advisory committee and providing their guidance.

A special thank you to my friends and family for their constant support, and to my girlfriend, Lauren Siegel, for her love, patience, and unconditional support.

# Table of Contents

Abstract.....	i
Acknowledgments.....	ii
Table of Contents.....	iii
List of Tables .....	vii
List of Figures .....	ix
List of Abbreviations .....	xi
Chapter 1.....	1
1 Introduction.....	1
1.1 Basic MRI Concepts .....	1
1.2 MRI Hardware .....	2
1.2.1 Radiofrequency and Gradient coils.....	3
1.2.2 Main Magnet.....	3
1.3 Relaxation and Bloch Equations.....	4
1.4 Contrast Mechanisms and $T_1$ Dispersion.....	6
1.5 Design Concepts .....	9
1.5.1 Fabry factor.....	9
1.5.2 Static Coil Design .....	11
1.5.3 Pulsed Coil Design.....	11
1.5.4 Fast-field Cycling Magnetic Resonance Imaging.....	12
1.6 Delta Relaxation Enhanced Magnetic Resonance .....	13
1.6.1 Hardware.....	14
1.6.2 DreMR Subtraction Sequence.....	15
1.7 Thesis Overview .....	16

1.8	References.....	18
Chapter 2.....		
2	Validated and Verified Design Study of Split Thick Power Solenoids .....	23
2.1	Device Testing and Motivation.....	23
2.2	Methods.....	25
2.2.1	Field Efficiency and Inductance .....	25
2.2.2	Exposure Region and Field Uniformity .....	26
2.2.3	Engineering Considerations and Performance Limitations .....	27
2.2.4	Design Method.....	28
2.2.5	Construction.....	29
2.2.6	Experimental Testing .....	29
2.3	Results.....	31
2.3.1	Coil Design .....	31
2.3.2	Experimental Validation .....	39
2.4	Discussion.....	42
2.5	Conclusions.....	45
2.6	References.....	45
Chapter 3.....		
3	Improved Contrast in DreMR Imaging at 0.5T through Optimized Polarization Sequences.....	48
3.1	Theory.....	48
3.1.1	DreMR Theory.....	51
3.2	Methods.....	52
3.2.1	General Simulation Approach.....	52
3.2.2	Verification of the Model.....	58
3.2.3	Field-cycled T <sub>1</sub> -Weighted Image Optimization.....	59

3.2.4	Improvement to Normalization.....	60
3.2.5	Optimization of DreMR Subtraction Method.....	61
3.3	Results.....	62
3.3.1	Verification of the Model.....	62
3.3.2	Field-cycled T <sub>1</sub> -weighted Image Optimization.....	66
3.3.3	Improvement to Normalization.....	69
3.3.4	Optimization of DreMR Subtraction Method.....	70
3.4	Discussion.....	75
3.5	Conclusions.....	79
3.6	References.....	79
Chapter 4	.....	82
4	Conclusion.....	82
4.1	Limitations.....	82
4.1.1	Chapter 2 Limitations.....	82
4.1.2	Chapter 3 Limitations.....	83
4.2	Future Directions.....	83
4.3	References.....	85
Appendices	.....	86
A.	Derivation of Solutions to Time-Varying Bloch Equations.....	86
A.1	Longitudinal Solution.....	86
A.2	Transverse Solution.....	87
B.	Numerical Analysis.....	87
B.1	Definitions.....	87
B.1.1	Error.....	87
B.1.2	Stability.....	88
B.1.3	Stiffness.....	89

B.1.4 Tolerance .....	90
B.2 Solving for Longitudinal Magnetization .....	91
B.2.1 Analytical Expressions .....	91
B.2.2 Numerical Methods .....	92
B.2.3 Analysis of Algorithms .....	95
B.3 Evaluation of Longitudinal Magnetization Methods .....	96
B.3.1 Case 1 .....	97
B.3.2 Case 2 .....	98
B.3.3 Case 3 .....	99
B.3.4 Case 4 .....	100
B.3.5 Case 5 .....	101
B.3.6 Discussion .....	101
B.4 Solving for Transverse Magnetization .....	103
B.5 Evaluation of Transverse Magnetization Methods .....	105
B.5.1 Case 1 .....	107
B.5.2 Case 2 .....	107
B.5.3 Case 3 .....	108
B.5.4 Case 4 .....	109
B.5.5 Discussion .....	110
C. References for Appendices .....	111
Curriculum Vitae .....	112

## List of Tables

Table 2.1: Design summary of electromagnetic and geometric parameters .....	37
Table 2.2: Error and uncertainty in the field map experiment .....	40
Table 2.3: Comparison of design and experimental performance .....	42
Table 3.1: Mean signal intensity and standard deviation for the image set .....	64
Table 3.2: Evaluation of image sets and simulations.....	66
Table 3.3: Contrast-to-noise ratio and sequence parameters. ....	69
Table 3.4: Normalization factors for the numerical and analytical method .....	70
Table 3.5: Sequence parameters for the sequences shown. ....	71
Table 3.6: Noise, SNR, and CNR for the sequences shown.....	72
Table 3.7: Sequence parameters for the sequences shown .....	73
Table 3.8: Noise, SNR, and CNR for the sequences shown.....	73
Table B.1: Data summary for case 1 .....	98
Table B.2: Data summary for case 2.....	98
Table B.3: Data summary for case 3.....	100
Table B.4: Data summary for case 4.....	101
Table B.5: Data summary for case 5.....	101
Table B.6: Data summary for case 1.....	107
Table B.7: Data summary for case 2.....	107
Table B.8: Data summary for case 3.....	109

Table B.9: Data summary for case 4..... 110

# List of Figures

Figure 1.1: Schematic of a uniform current density, split solenoid coil .....	10
Figure 1.2: Normalized Fabry factor .....	10
Figure 1.3: dreMR insert coil.....	14
Figure 2.1: Field uniformity as calculated over a 6cm diameter sphere.....	32
Figure 2.2: Dissipated power in [kW] for uniform current density solenoids .....	33
Figure 2.3: Maximum central magnetic field .....	34
Figure 2.4: Maximum dB/dt .....	35
Figure 2.5: 3D drawing of the switched field exposure system.....	38
Figure 2.6: Close-up of the windings during construction .....	38
Figure 2.7: Field uniformity map over the yz-plane of the testing region.....	41
Figure 3.1: Relaxation dispersion profiles of Ablavar.....	54
Figure 3.2: Example field-shift sequence .....	56
Figure 3.3: Flowchart of the general simulation approach .....	58
Figure 3.4: Schematic of the magnetization preparation sequences .....	59
Figure 3.5: Phantom image, obtained using field-cycling .....	63
Figure 3.6: Simulations showing how the magnetizations .....	68
Figure 3.7: Simulations showing the optimal dreMR subtraction .....	71
Figure 3.8: Simulations showing the optimal dreMR subtraction .....	73
Figure 3.9: Simulated phantom images for the sequences shown .....	74

Figure 3.10: Simulated phantom images for the sequences shown .....	75
Figure 3.11: $R_1$ curves for bound agent and fat from 0 to 1 T .....	77
Figure B.1: Test sequences for evaluating longitudinal magnetization .....	97
Figure B.2: Percent error of different methods with respect to the analytical solution .....	97
Figure B.3: Percent error of different methods with respect to the analytical solution .....	98
Figure B.4: Absolute residual error for case 2 .....	99
Figure B.5: True step size for the ODE methods of case 2 .....	99
Figure B.6: Percent error of different methods with respect to the ode45 solution .....	100
Figure B.7: Percent error of different methods with respect to the ode45 solution .....	100
Figure B.8: Percent error of different methods with respect to the ode45 solution .....	101
Figure B.9: Test sequences for evaluating transverse magnetization .....	106
Figure B.10: Absolute error of different methods with respect to .....	107
Figure B.11: Relative (left) and absolute (right) error of different methods .....	107
Figure B.12: True step size for the ODE methods of an extended case 2 .....	108
Figure B.13: Absolute error of different methods with respect to .....	108
Figure B.14: True step size for the ODE methods of an extended case 3. ....	109
Figure B.15: Relative (top) and absolute (bottom) error of different methods .....	109

## List of Abbreviations

$B_0$	Main magnetic field
$C$	Contrast
CNR	Contrast-to-noise ratio
dB/dt	Time rate of change of the magnetic field
dreMR	Delta Relaxation Enhanced Magnetic Resonance
DSV	Diameter of spherical volume
FFC	Fast-field-cycling
MRI	Magnetic resonance imaging
$nF$	Normalization factor
NMR	Nuclear magnetic resonance
NMRD	Nuclear magnetic resonance dispersion
ODE	Ordinary differential equation
PBS	Phosphate buffer saline
PMRI	Pre-polarized magnetic resonance imaging
$r_1$	Longitudinal relaxivity
$R_1$	Longitudinal relaxation rate
$R_2$	Transverse relaxation rate
RF	Radiofrequency
rms	Root-mean square
ROI	Region of interest
RSA	Rabbit serum albumin
$S$	Signal
SNR	Signal-to-noise ratio
$T_1$	Longitudinal relaxation time constant
$T_2$	Transverse relaxation time constant
$T_R$	Repetition time
TSR	Tissue-suppression-ratio

## Chapter 1

### 1 Introduction

Magnetic resonance imaging (MRI) is an imaging modality with a wide variety of contrast mechanisms due to the MR signal being dependent on many imaging and physiological parameters. This thesis focuses on developments made to the field-cycling imaging technique known as delta relaxation enhanced magnetic resonance (dreMR). This chapter introduces the concepts necessary for understanding the developments presented. For a more in-depth review of MRI, the following textbook is recommended: “*Magnetic Resonance Imaging: Physical Principles and Sequence Design*” by E.M. Haacke et al<sup>1</sup>.

#### 1.1 Basic MRI Concepts

When protons are in the presence of an external magnetic field, a net magnetization will form parallel to that field due to interaction with the magnetic moments. A detectable quantity of magnetization is possible due to the abundance of protons in biological tissue. The equilibrium magnetization,  $M_0$ , depends on the proton density,  $\rho_0$ , the gyromagnetic ratio,  $\gamma$ , the external magnetic field,  $B_0$ , and the temperature,  $T$ ,

$$M_0 = \frac{\rho_0 \gamma^2 \hbar^2 B_0}{4kT} \quad (1.1)$$

where  $\hbar$  is Planck’s constant divided by  $2\pi$  and  $k$  is Boltzmann’s constant. The individual protons will precess around the main field direction at a specific angular frequency, given by

$$\omega_0 = \gamma B_0 \quad (1.2)$$

where  $\gamma$  is approximately  $2.675 \times 10^8 \frac{\text{rad}}{\text{s T}}$  for the hydrogen proton (so that  $\frac{\gamma}{2\pi} = 42.577 \frac{\text{MHz}}{\text{T}}$ ), and  $B_0$  is the magnitude of the main magnetic field (by convention along the z-axis). This frequency, known as the Larmor frequency, is in the radiofrequency (RF) range.

Obtaining a nuclear magnetic resonance (NMR) signal requires the bulk magnetization,  $\vec{M}(\vec{r}, t) = (M_x, M_y, M_z)$ , to be excited out of its equilibrium state by an application of an RF pulse at the Larmor frequency, perpendicular to the main magnetic field. Given the appropriate RF pulse strength and time, the longitudinal component of the magnetization,  $M_z$ , will be tipped into the transverse direction,  $M_{xy}$ . As the magnetization precesses around the external magnetic field, a changing magnetic flux is produced in the xy-plane which can be detected by an RF receive coil. The resulting time-dependent NMR signal is proportional to the angular precession frequency and the magnitude of the bulk magnetization. It follows that the signal,  $S$ , depends on the square of the static magnetic field  $B_0$

$$S \propto \frac{\gamma^3 B_0^2 \rho_0}{T} \quad (1.3)$$

## 1.2 MRI Hardware

There are three main hardware components in MRI: the main magnet, gradient coils, and radiofrequency coils. RF and gradient coils and their respective fields are not a point of focus in this thesis, therefore, they will only be described briefly.

### 1.2.1 Radiofrequency and Gradient coils

The RF coils serve two purposes in MRI. The first is to excite the magnetization away from thermal equilibrium, using an RF transmit coil. The second is to detect the MR signal through the use of an RF receive coil. The two tasks could be achieved through a single RF coil, but are often separated into two components such that each component can be optimized for high performance. Hoult et al. gives a general review of RF coils<sup>2</sup>.

Gradient coils perform the task of providing spatial information to the signal, allowing images to be formed. The three gradient coils provide a linear gradient to the z-component of the magnetic field along the three Cartesian axes. These fields are rapidly switched during imaging to spatially encode the frequency and phase of the magnetization. Gradient coil design has been accomplished using a variety of methods<sup>3-8</sup>.

### 1.2.2 Main Magnet

The static magnetic field provides the electromagnetic environment under which two important processes are achieved for imaging. The first is to create magnetization by polarizing the magnetic moments in the sample. The second is to provide a torque through which precession of the spins can occur.

The main magnetic field must be strong, homogeneous, and temporally stable. The most common clinical field strengths are 1.5 T and 3.0 T, which are typically achieved using superconducting systems. Lvovsky and Jarvis highlight trends and accompanying challenges of designing superconducting magnets for MRI<sup>9</sup>. Resistive magnet systems are also used for research purposes, as described in Section 1.5.4. The main field must be uniform enough such that the local variation across a voxel due to inhomogeneities is much

less than that imposed by the gradient fields, otherwise image distortion can occur. Furthermore, field inhomogeneity leads to faster dephasing of the spins, resulting in decreased signal.

### 1.3 Relaxation and Bloch Equations

There are two relaxation mechanisms with which thermal equilibrium of magnetization is reestablished after being perturbed. After rotation of the magnetization into the transverse plane, the longitudinal magnetization will relax back to its equilibrium magnetization value with an exponential time constant,  $T_1$ . This is referred to as longitudinal- or  $T_1$ -relaxation.  $T_1$  is the time required for the  $z$ -component to reach  $(1-1/e)$  of maximum value,  $M_0$ . Another useful way to refer to this mechanism is by the relaxation rate,  $R_1$ , which is the inverse of  $T_1$ . In the absence of an external magnetic field, there is no net magnetization vector of the nuclear spins. When a static magnetic field is present, thermal motion of molecules and precession of the spins causes rapid fluctuations of the local magnetic field. This results in preferential transitions of the spins from high-energy states to low-energy states, leading to bulk magnetization, where the energy is given to the surrounding lattice. This process is referred to as dipolar coupling and is the predominant spin-lattice relaxation mechanism of spin- $1/2$  particles. The probability of a transition of a spin to a lower state is proportional to the value of the spectral density of the magnetic oscillations at the Larmor frequency. Protons in a highly mobile environment, such as free water, have a wide distribution of tumbling rates such that the value of the spectral density at any given frequency is low. Protons that have restricted mobility, such as water in hydration layers around proteins, have a spectral density function peaked around zero

because the dipolar interactions fluctuate more slowly. There is a greater fraction of protons oscillating near the Larmor frequency, making them more efficient at spin-lattice relaxation. It is because the spectral energy density varies with frequency that  $T_1$  changes with the strength of the static magnetic field.

The relaxation mechanism describing the behaviour of transverse magnetization is called  $T_2$ -relaxation. The transverse magnetization loses phase coherence exponentially over time due to small variations in the local magnetic field and through spin-spin interaction. This leads to a reduction of the detected signal.  $T_2$  is the time constant for when the transverse magnetization falls to  $1/e$  of its initial value. The inverse,  $R_2$ , is the transverse relaxation rate.

The Bloch equations are a set of phenomenological ordinary differential equations (ODE) that describe the time evolution of the macroscopic nuclear magnetization,  $\vec{M}$ , of a sample<sup>10</sup>. In vector form, the equation is

$$\frac{d\vec{M}}{dt} = \gamma\vec{M} \times \vec{B} + \frac{1}{T_1}(M_0 - M_z)\hat{z} - \frac{1}{T_2}\vec{M}_\perp, \quad (1.4)$$

where  $\vec{M}_\perp = M_x\hat{x} + M_y\hat{y}$  is the transverse component of the magnetization. In component form, the equations are

$$\frac{dM_z}{dt} = \gamma(B_y M_x - B_x M_y) + \frac{(M_0 - M_z)}{T_1} \quad (1.5a)$$

$$\frac{dM_x}{dt} = \gamma(B_z M_y - B_y M_z) - \frac{M_x}{T_2} \quad (1.5b)$$

$$\frac{dM_y}{dt} = \gamma(B_x M_z - B_z M_x) - \frac{M_y}{T_2}. \quad (1.5c)$$

For the constant field case, where  $\vec{B} = B_0 \hat{z}$ , the solutions to these equations in the laboratory frame following the application of a 90° RF pulse (that is, the magnetization at time zero immediately following the pulse is  $\vec{M}(0^+) = [M_0, 0, 0]$ ) are

$$M_z(t) = M_0(1 - e^{-t/T_1}) \quad (1.6a)$$

$$M_{xy}(t) = M_{xy}(0)e^{-i\varphi(t)}e^{-t/T_2} \quad (1.6b)$$

where  $M_{xy} = M_x + iM_y$ , and  $\varphi(t) = \omega_0 t + \varphi(t_0)$ .

For a repeated spin-echo experiment, if the signal was measured at echo time,  $T_E$ , and repetition time,  $T_R$ , the signal would be proportional to the transverse magnetization

$$M_{\perp} = M_0 \left(1 - e^{-\frac{T_R}{T_1}}\right) e^{-\frac{T_E}{T_2}}, \quad (1.7)$$

where the echo has refocused the time independent transverse relaxation effects.

## 1.4 Contrast Mechanisms and $T_1$ Dispersion

The three fundamental forms of image contrast in MRI are proton density,  $T_1$  relaxation, and  $T_2$  relaxation. It is clear from Equation (1.7) that sensible choices of  $T_R$  and

$T_E$  would allow for enhancement of any of the three variables in the final signal. The focus of this thesis is on the  $T_1$  contrast mechanism.  $T_1$ -weighted imaging is achieved with the choice of a very short echo time. This minimizes transverse effects, but cannot neglect the effect of spin density.

There are several factors that can affect the  $T_1$  of a sample, such as the molecular makeup of the tissue, the magnetic field strength, and the local cellular environment. The intrinsic differences in relaxation times across tissues is often enough to generate sufficient contrast such that information can be provided on anatomy, function, and metabolism of tissues *in vivo*<sup>11,12</sup>. This mechanism also extends to the discrimination of pathological tissue<sup>13</sup>. However, some diseased tissue does not significantly alter relaxation, limiting the sensitivity and specificity of diagnosis<sup>12,14</sup>. Limited contrast can also occur at certain field strengths due to the tendency of  $T_1$  values to converge at higher fields<sup>15,16</sup>.

The contrast between normal and pathological tissue can be enhanced using contrast agents, which shorten  $T_1$  and  $T_2$  relaxation times<sup>12,17</sup>. Contrast agents are not imaged directly, rather they work by increasing the relaxation rate of local hydrogen protons<sup>12</sup>. There are both positive and negative contrast agents. Positive contrast agents typically contain paramagnetic metal ions, such as gadolinium. This leads to a positive contrast effect, meaning an increase in signal intensity, or brightness, in  $T_1$ -weighted images<sup>18</sup>. Gadolinium makes for an effective contrast agent because it has seven unpaired electrons in its outer shell, making it strongly paramagnetic. The gyromagnetic ratio of an electron is much larger than a proton, therefore the dipole-dipole interactions are much stronger because the magnitude of the magnetic moments influences the local field fluctuations. Negative contrast agents are iron particle based and create a negative contrast

effect, meaning a decrease in signal intensity, or darkness, in T<sub>2</sub>-weighted images. Relaxivity is defined as the increase in relaxation rate per unit increase in concentration of the contrast agent<sup>17</sup>:

$$r_i = \frac{R_{i,observed} - R_{i,buffer}}{[CA]}, i = 1,2. \quad (1.8)$$

A class of contrast agents that are designed to target specific molecules can be used to image processes at the cellular and molecular level<sup>18</sup>. Some targeted contrast agents can also have functional properties, for example by showing increased relaxivity upon binding with the target molecule. This is common amongst gadolinium-based contrast agents, which show contrast enhancement in both the bound and unbound states<sup>19-21</sup>. Ablavar (Gadofosveset trisodium, Lantheus Medical Imaging, Inc. N. Billerica, MA, USA) is a blood pool contrast agent that binds to serum albumin, the most abundant protein in blood plasma<sup>22,23</sup>. Through detection of the bound state of Ablavar, the localization of albumin is possible, which may be useful for assessment of tumour angiogenesis or myocardial infarction<sup>24</sup>.

While Ablavar in its unbound state still shows an increase in relaxivity, only in its bound state does it exhibit strong T<sub>1</sub> dependence on magnetic field<sup>20</sup>. It is possible to distinguish between dispersive and non-dispersive tissues using a contrast mechanism called T<sub>1</sub> dispersion<sup>25-27</sup>. Integral to this mechanism is the ability to modulate the main magnetic field throughout imaging in order to probe T<sub>1</sub> values at different field strengths. Various names have been given to the different methods through which T<sub>1</sub> dispersion can be achieved, including, but not limited to: fast-field-cycling magnetic resonance imaging (FFC-MRI)<sup>27</sup>, MR relaxometry<sup>26,28</sup>, prepolarized MRI (PMRI)<sup>25,29,30</sup>, and dreMR<sup>31-33</sup>. A

literature review of these methods with a focus on design concepts is given in the following sections.

## 1.5 Design Concepts

### 1.5.1 Fabry factor

The relationship between the field at the center of a solenoid coil,  $B_0$ , and the resistive power of the coil,  $P$ , is characterized by the Fabry formula<sup>34,35</sup>:

$$B_0 = \mu_0 \sqrt{\frac{P\lambda}{\rho a_1}} G_0(\alpha, \beta, \gamma). \quad (1.9)$$

where  $\mu_0$  is the magnetic permeability of free space,  $\lambda$  is the filling factor of the coil windings, and  $\rho$  is the resistivity. The geometry of the coil is described by  $a_1$ ,  $\alpha$ ,  $\beta$ , and  $\gamma$ , which are the inner radius, ratio of outer radius to inner radius, ratio of half the length of the coil to inner radius, and ratio of half the length of the axial gap to inner radius, respectively. A schematic diagram is shown in Figure 1.1. The geometrical term of Equation (1.9) is the Fabry factor. For a uniform current density solenoid, this factor is  $G_0(\alpha, \beta, \gamma) = G(\alpha, \beta) - G(\alpha, \gamma)$ , where

$$G(\alpha, \xi) = \sqrt{\frac{\xi}{2\pi(\alpha^2 - 1)}} \ln \frac{\alpha + \sqrt{\alpha^2 + \xi^2}}{1 + \sqrt{1 + \xi^2}}. \quad (1.10)$$

The Fabry factor is a maximum when  $(\alpha, \beta, \gamma) = (\sim 3, \sim 2, 0)$ , although, practical coil design can limit how attainable this aspect ratio is due to thermal properties, coil stresses, size, and cost.

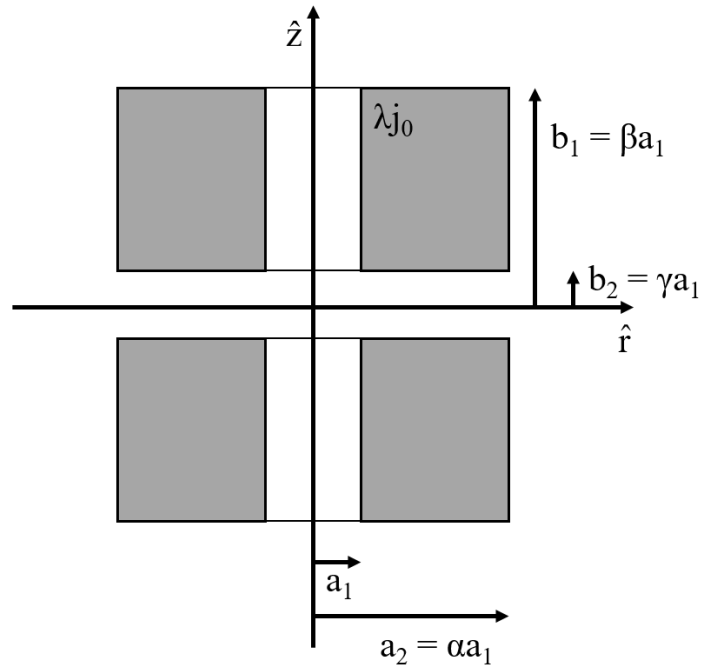


**Figure 1.1:** Schematic of a uniform current density ( $j_0$ ), split solenoid coil with rectangular cross-section and inner radius,  $a_1$ . The outer radius, height, and gap are  $a_2 = \alpha a_1$ ,  $b_1 = \beta a_1$ , and  $b_2 = \gamma a_1$ , respectively.

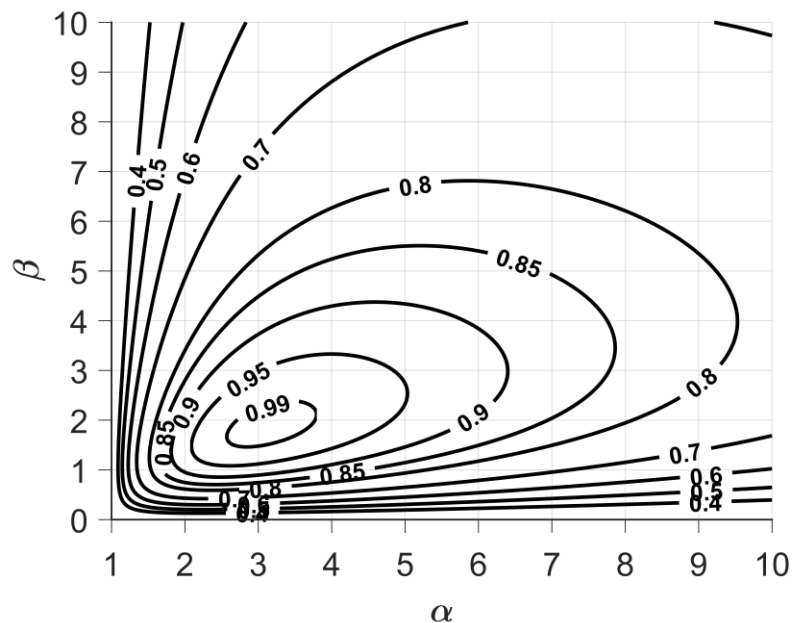


**Figure 1.2:** Normalized Fabry factor for a rectangular coil with uniform current density as a function of parameters  $\alpha$  and  $\beta$  (for  $\gamma = 0$ ). The function has a maximum at  $(\alpha, \beta) \cong (3, 2)$ .

### 1.5.2 Static Coil Design

The design of thick power solenoid magnets is primarily focused on maximizing magnetic flux density from an applied electrical power, in addition to achieving a certain field uniformity over a specified volume. A well-regarded early method for the design of coils that produce static, homogeneous fields was based on the spherical harmonic expansion of the central field<sup>34,36-38</sup>. By setting coefficients of higher spatial derivatives of the field at the center of the coil to zero, the radii, locations, and current density of the coil system could be determined. For example, the classic Helmholtz pair separates two identical thin solenoids by a distance equal to their radius and cancels out the second-order coefficient to achieve improved homogeneity, causing the field to vary as the fourth power of the distance. For thick solenoids of rectangular cross-section, the field can be corrected up to the eighth-order through combination of inner- and outer-notches, radially dividing the coil to have different current densities, and with the use of further correction coils<sup>38</sup>. Higher orders can also be corrected but the methods increase in complexity and decrease power efficiency<sup>37</sup>. While central expansion is a common method of modern coil design, there have been massive developments in numerical approaches such as target field methods<sup>39</sup>, subset selection<sup>40</sup>, simulated annealing<sup>29</sup>, linear programming<sup>41</sup>, and non-linear optimization<sup>42</sup>.

### 1.5.3 Pulsed Coil Design

A third important design criterion for magnet design is the ability to rapidly switch the magnetic field ( $dB/dt$ ). Field-cycled NMR is a technique used to study  $T_1$  as a function of magnetic field strength, with various design methods<sup>43-46</sup> and applications<sup>47-49</sup>. The

commercially successful method of Schweikert et al. allows optimization of power efficiency, uniformity, and switching rate with a current density close to the Kelvin distribution<sup>43</sup>. However, the helical structure, and continuously varying wire thickness can lead to issues in construction, power dissipation, and thermal stress<sup>44</sup>. A field-cycled NMR magnet must be strong to produce sufficient nuclear magnetization, but also very homogeneous such that during detection there is not excessive loss of phase coherence of precessing spins. Since the detection frequency is always the same, the coil must modulate the magnetic field during polarization to observe relaxation behaviour at different field strengths. Additionally, field switching must be rapid enough to ensure that measurements are not confounded by a wash of multiple relaxation times. Designing a system that meets these specifications is challenging and can only be permitted with good cooling efficiency, limited bore diameter, and versatile supply of power<sup>48</sup>. This problem can be lessened in part by splitting the performance responsibilities across two or more magnets.

#### 1.5.4 Fast-field Cycling Magnetic Resonance Imaging

The application of fast-field-cycling to MRI was demonstrated by Carlson et al. in a technique dubbed MR relaxometry imaging<sup>26,28</sup>. A pulsed electromagnet composed of a thick split solenoid of 10 cm radius, maximum variation of 45 mT, and switching rate of 6 T/s was inserted into a 64 mT permanent magnet. The two coils were used in tandem during the polarizing and relaxation portion of the sequence by modulation of the main magnetic field to make  $T_1$  measurements of biological tissues. The stringent homogeneity requirements were the responsibility of the permanent magnet, in contrast to the pulsed magnet, which had a homogeneity up to 30%. It is typical in field-cycling techniques for the RF coils to be tuned to a narrow frequency range corresponding to the resonance

frequency of protons at the field strength of one of the magnets. Therefore, during the RF excitation and acquisitions portion of the sequence, the pulsed electromagnet must be disabled.

Another method, called prepolarized magnetic resonance imaging, uses a standalone system composed of two separate and dynamically controllable resistive magnets<sup>40,50</sup>. The polarizing magnet is responsible for increasing the magnetization of the sample and must be strong, but not necessarily uniform. The inhomogeneity can be on the order of tens of percent depending on the application, since it only leads to slight shading across the image. This reduces cost and also allows for higher polarizing fields to be achieved<sup>28</sup>. The readout magnet, used during signal detection, has a relatively low magnetic field strength, which must be both stable and uniform. PMRI has been used to image small animals, human extremities, and differentiate between fat and protein-rich tissues by means of detecting quadrupole dips in tissue  $T_1$  dispersion curves<sup>25,29,30</sup>.

## 1.6 Delta Relaxation Enhanced Magnetic Resonance

DreMR is a field-cycling method that facilitates the generation of image contrast related to the  $T_1$  dispersion profile of activatable contrast agents in the bound state, while suppressing signal from unbound agent and normal biological tissue<sup>31</sup>. This technique uses an actively-shielded, auxiliary, field-cycling coil inserted into a clinical MR system, without permanent modification to the host system<sup>51,52</sup>. This coil is used to cycle the field during the polarization section of the imaging sequence, but is electrically isolated during signal detection. A previously designed and constructed dreMR coil is shown in Figure

1.3.00

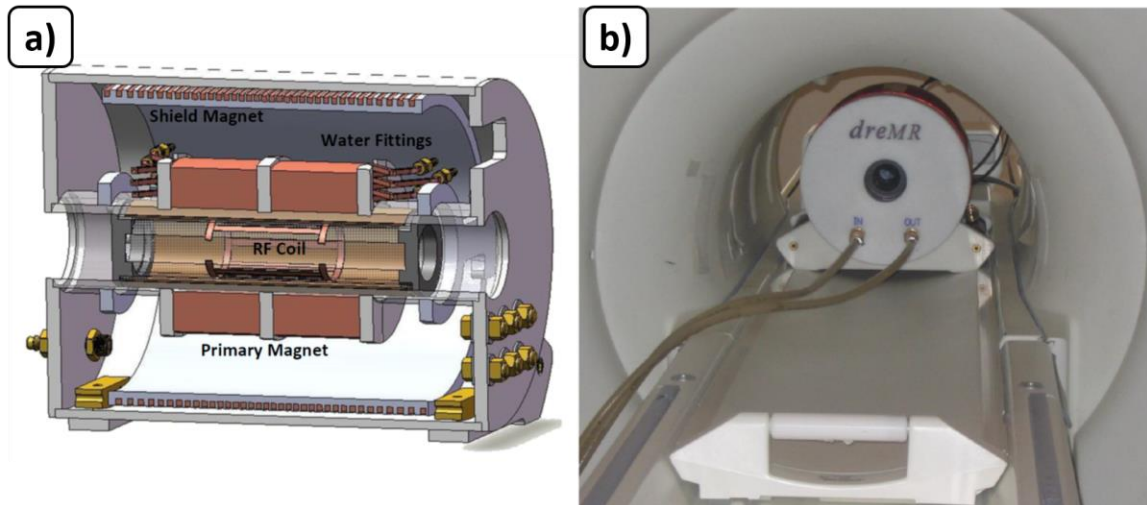


**Figure 1.3:** dreMR insert coil. a) A computer aided drawing of a dreMR system. b) The dreMR insert on the patient bed of an MRI machine.

### 1.6.1 Hardware

The important aspects of the dreMR coil are maximizing field efficiency, good thermal management, ramping quickly, and minimizing inductive coupling with the MR system. To increase the signal-to-noise ratio (SNR) in the dreMR image, the field shift should be as large as possible<sup>31</sup>. The heat that is dissipated into the resistive windings can limit the maximum field shift and duty cycle of the coil, as observed by Hoelscher et al.<sup>33</sup>, therefore the coils should be engineered to have excellent cooling capacity<sup>6</sup>. The switched fields of the insert coil will deposit energy in the cryostat of the host MR system in the form of undesirable eddy currents, which can lead to image distortion and frequency shift errors<sup>53</sup>. Correction strategies have been implemented via dynamic frequency adjustment during readout and post-processing<sup>54,55</sup>, however Harris et al. maintain that a combination of hardware and software strategies is preferred<sup>52</sup>. Active shielding of the coil is generally achieved with a single layer secondary coil at a radius larger than the primary windings,

with current flowing in the opposite direction to reduce the magnetic field external to the combined dreMR system. In the prototype dreMR coil, a target-field method was used to design the shield<sup>51</sup>, but significant improvements have since been made using the boundary element method<sup>52,56</sup>.

## 1.6.2 DreMR Subtraction Sequence

The simplest implementation of dreMR is a weighted subtraction of two  $T_1$ -weighted images. In the positive-shift image, the dreMR coil applies a magnetic field in the same direction as the static field of the host MR system. In the negative-shift image, the coil is used to decrease the main magnetic field. This allows for the acquisition of images where polarization has occurred at field strengths with large differences in  $R_1$  for dispersive tissues, but with relatively minor differences for non-dispersive tissues. Additionally, modulation of the main magnetic field also affects the equilibrium magnetization of the samples. Therefore, to obtain true  $T_1$ -dispersion-based contrast the field-cycled images are normalized to account for the differences in equilibrium magnetization at these two fields. Subtraction of the two images would produce an image with signal intensity from only the field dependent tissues.  $T_1$  dispersion adds an extra dimension of information over conventional imaging methods, which may provide increased diagnostic potential to MRI<sup>15,25</sup>. DreMR has been used to directly image protein in human extremities<sup>57</sup>, measure relaxation rates of various murine tissue<sup>58</sup>, imaging murine tumor models<sup>59</sup>, as well as quantify contrast agent concentration<sup>33</sup>.

DreMR is associated with many advantages compared to conventional imaging methods. In contrast-enhanced  $T_1$ -weighted images, it can be difficult to distinguish

between enhancement caused by agent in its bound state or from the accumulation of agent in the unbound state<sup>18,24</sup>. This is particularly relevant in heterogeneous samples in which variations in proton density and relaxation rate, partial volume effects, and varying concentration of unbound agent prevent unambiguous localization of the bound agent<sup>33</sup>. Richardson et al. demonstrated the feasibility of determining the concentration of serum albumin in vitro by measuring longitudinal and transverse relaxation rates both pre- and post-injection of Ablavar<sup>24</sup>. The method was successfully validated at 3.0 T and 4.7 T, but the mathematical model breaks down at lower fields. Furthermore, there are several disadvantages of traditional T<sub>1</sub>-weighted subtraction imaging, such as positional changes between the two sets of images, magnetic field and temperature drifts, and other long time-scale systematic errors<sup>52</sup>. DreMR subtraction images are captured with interleaved sampling of positive and negative shift images, such that any systematic errors affect the images equally. The resulting dreMR image will have reduced SNR compared to traditional T<sub>1</sub>-weighted images, but with greater contrast-to-noise ratio (CNR) between tissues.

## 1.7 Thesis Overview

Although dreMR has several advantages, advancements are still required to further improve and extend applications of this technique. Since the dreMR coil is a resistive magnet, there are limits on field shift amplitude and duty cycle, both of which reduce SNR efficiency. Ideally, the hardware would achieve higher field- and power-efficiency with increased cooling capacity and improved field uniformity over a larger imaging region, while maintaining low inductive coupling with the host system. Moreover, further research is required to determine the optimal polarization sequence for a given application, which may be qualitatively different than the dreMR subtraction sequence described earlier.

Since dreMR requires the use of a host MR scanner, the most common implementation is with commercial 1.5 T scanners<sup>31,33,52,54,55,58,60</sup>. However, there is evidence that dreMR may have significant advantages at a lower field. Most gadolinium-based contrast agents show larger  $R_1$  values at 0.5 T than at 1.5 T<sup>61</sup>. Therefore, the reduced SNR at lower fields may be compensated by signal averaging due to smaller  $T_R$  time. There are also larger ratios of  $R_1$  values of bound agent compared to unbound agent and normal biological tissue at 0.5 T, allowing the potential to provide better dispersion-based contrast. Furthermore, there are general advantages of imaging at lower field, such as reduced system cost, reduced specific absorption rate, reduced effects from local field inhomogeneities or differences in susceptibility, and less acoustic noise<sup>62</sup>.

To realize these improvements to dreMR, several steps must be taken regarding hardware and sequence design. Chapter 2 presents a method to design pulsed solenoid magnets. This can be applied to the design optimization of the primary windings of a dreMR coil. Previous studies were typically limited by hardware, so it is important to make this process rigorous and validated, since previous design methods for dreMR coils are not well-documented. The main objectives of Chapter 2 are to develop a general design method and to validate this method by designing, constructing, and testing an electromagnet before use in designing a new dreMR coil. The intention here is to determine and overcome obstacles related to primary coil design, so that potentially expensive and time-consuming mistakes can be avoided in the future. The application to validate the design method developed in Chapter 2 is a single-axis, switched magnetic field exposure system to test the effects of time-varying magnetic fields on medical devices. The added novelty of this task is that some international device testing standards require the use of said benchtop

coils, but provide no method to design one. This chapter provides a straightforward and detailed method to do so.

DreMR theory must be generalized to lower field strengths, where there may exist non-linear relationships between relaxation rate and magnetic field. Although research on sequence design through imaging experiments is necessary to refine current techniques<sup>58</sup>, an effective way to discover and optimize new imaging techniques is through simulation. Chapter 3 provides a general simulation algorithm that is flexible enough to be used for several different applications. As a model for tissue magnetization under time-varying magnetic fields, the tool is able to accurately predict contrast between tissues and thus optimize dreMR pulse sequences by evaluation of the contrast. The simulation tool is capable of taking into consideration hardware constraints in sequence optimization. Inversely, and importantly, the tool can be used to provide the hardware requirements to achieve maximum contrast for a given imaging application. This can be coupled with the algorithm of Chapter 2 to design a dreMR coil magnet that is tailored to a specific application.

## 1.8 References

1. Haacke EM, Brown RW, Thompson MR, Venkatesan R. Magnetic resonance imaging: physical principles and sequence design. 1999. *New York A John Wiley Sons*. 1999.
2. Hoult DI. The NMR receiver: A description and analysis of design. *Prog Nucl Magn Reson Spectrosc*. 1978;12(1):41-77. doi:10.1016/0079-6565(78)80002-8.
3. Wong EC, Jesmanowicz A, Hyde JS. Coil Optimization for Mri by Conjugate-Gradient Descent. *Magn Reson Med*. 1991;21(1):39-48. doi:DOI 10.1002/mrm.1910210107.
4. Turner R. Minimum inductance coils. *J Phys E*. 1988;21(10):948-952. doi:10.1088/0022-3735/21/10/008.
5. Turner R. Gradient coil design: A review of methods. *Magn Reson Imaging*.

- 1993;11(7):903-920. doi:10.1016/0730-725X(93)90209-V.
6. Handler WB, Harris CT, Scholl TJ, et al. New head gradient coil design and construction techniques. *J Magn Reson Imaging*. 2014;39(5):1088-1095. doi:10.1002/jmri.24254.
  7. Chronik BA, Rutt BK. Constrained Length Minimum Inductance Gradient Coil Design. *Magn Reson Med*. 1998;39:270-278.
  8. Crozier S, Doddrell D. Gradient-coil design by simulated annealing. *J Magn Reson Ser A*. 1993;103:354. doi:10.1006/jmra.1993.1178.
  9. Lvovsky Y, Jarvis P. Superconducting systems for MRI-present solutions and new trends. *IEEE Trans Appl Supercond*. 2005;15(2 PART II):1317-1325. doi:10.1109/TASC.2005.849580.
  10. Bloch F. Nuclear induction. *Phys Rev*. 1946;70(7-8):460-474. doi:10.1103/PhysRev.70.460.
  11. Bottomley PA, Foster TH, Argersinger RE, Pfeifer LM. A review of normal tissue hydrogen NMR relaxation times and relaxation mechanisms from 1-100 MHz: Dependence on tissue type, NMR frequency, temperature, species, excision, and age. *Med Phys*. 1984;11(4):425-448. doi:10.1118/1.595535.
  12. Strijkers GJ, Mulder WJM, Tilborg GAF Van, Nicolay K. MRI Contrast Agents: Current Status and Future Perspectives. *Anticancer Agents Med Chem*. 2007;7:291-305.
  13. Bottomley PA, Hardy CJ, Argersinger RE, Allen-Moore G. A review of <sup>1</sup>H nuclear magnetic resonance relaxation in pathology: are T1 and T2 diagnostic? *Med Phys*. 1987;14(1):1-37. doi:10.1118/1.596111.
  14. Wood ML, Hardy PA. Proton Relaxation Enhancement. *J Magn Reson Imaging*. 1993;3(1):149-156.
  15. Rinck P, Fischer H, Vander Elst L, Van Haverbeke Y, Muller R. Field-cycling relaxometry: medical applications. *Radiology*. 1988;168(3):843-849.
  16. Koenig SH, Brown RD, Adams D, Emerson D, Harrison CG. Magnetic-Field Dependence of 1/T1 of Protons in Tissue. *Invest Radiol*. 1984;19(2):76-81. doi:10.1097/00004424-198403000-00002.
  17. Lauffer RB. Paramagnetic Metal Complexes as Water Proton Relaxation Agents for NMR Imaging: Theory and Design. *Chem Rev*. 1987;87(5):901-927. doi:10.1021/cr00081a003.
  18. Makowski MR, Wiethoff AJ, Jansen PCHP, Botnar M. Molecular Imaging With Targeted Contrast Agents. 2010;20(4):247-259.
  19. Caravan P. Strategies for increasing the sensitivity of gadolinium based MRI contrast agents. *Chem Soc Rev*. 2006;35(6):512. doi:10.1039/b510982p.
  20. Eldredge HB, Spiller M, Chasse JM, Greenwood MT, Caravan P. Species dependence on plasma protein binding and relaxivity of the gadolinium-based MRI contrast agent MS-325. *Invest Radiol*. 2006;41(3):229-243.

doi:10.1097/01.rli.0000199293.86956.48.

21. Overoye-Chan K, Koerner S, Looby RJ, et al. EP-2104R: A fibrin-specific gadolinium-based MRI contrast agent for detection of thrombus. *J Am Chem Soc.* 2008;130(18):6025-6039. doi:10.1021/ja800834y.
22. Clarkson RB. Blood-pool MRI contrast agents: Properties and characterization. *Top Curr Chem.* 2002;221(Contrast Agents I: Magn.Reson.Imaging):201-235.
23. Caravan P, Cloutier NJ, Greenfield MT, et al. The interaction of MS-325 with human serum albumin and its effect on proton relaxation rates. *J Am Chem Soc.* 2002;124(12):3152-3162. doi:ja017168k [pii].
24. Richardson OC, Bane O, Scott MLJ, et al. Gadofosveset-based biomarker of tissue albumin concentration: Technical validation in vitro and feasibility in vivo. *Magn Reson Med.* 2015;73(1):244-253. doi:10.1002/mrm.25128.
25. Ungersma SE, Matter NI, Hardy JW, et al. Magnetic resonance imaging with T1 dispersion contrast. *Magn Reson Med.* 2006;55(6):1362-1371. doi:10.1002/mrm.20910.
26. Carlson W, Goldhaber DM, Brito A, Kaufman BSL. MR Relaxometry Imaging. *IRadiology.* 1992;184(3):635-639.
27. Lurie DJ, Aime S, Baroni S, et al. Fast field-cycling magnetic resonance imaging. *Comptes Rendus Phys.* 2010;11(2):136-148. doi:10.1016/j.crhy.2010.06.012.
28. Carlson JW, Crooks LE, Arakawa M, Goldhaber DM, Kramer DM, Kaufman L. Switched Field Magnetic Resonance Imaging. In: *Medical Imaging VI: International Society for Optics and Photonics.* ; 1992:22-27.
29. Gilbert KM, Handler WB, Scholl TJ, Odegaard JW, Chronik BA. Design of field-cycled magnetic resonance systems for small animal imaging. *Phys Med Biol.* 2006;51(11):2825-2841. doi:10.1088/0031-9155/51/11/010.
30. Matter NI, Scott GC, Grafendorfer T, MacOvski A, Conolly SM. Rapid polarizing field cycling in magnetic resonance imaging. *IEEE Trans Med Imaging.* 2006;25(1):84-93. doi:10.1109/TMI.2005.861014.
31. Alford JK, Rutt BK, Scholl TJ, Handler WB, Chronik BA. Delta relaxation enhanced mr: Improving activation - Specificity of molecular probes through R1 dispersion imaging. *Magn Reson Med.* 2009;61(4):796-802. doi:10.1002/mrm.21933.
32. Araya YT. Delta Relaxation Enhanced Magnetic Resonance - Development and Application of a Field-Cycling Contrast Mechanism. 2013;(May):100.
33. Hoelscher UC, Lothar S, Fidler F, Blaimer M, Jakob P. Quantification and localization of contrast agents using delta relaxation enhanced magnetic resonance at 1.5 T. *Magn Reson Mater Physics, Biol Med.* 2012;25(3):223-231. doi:10.1007/s10334-011-0291-6.
34. Montgomery DB. *Solenoid Magnet Design. The Magnetic and Mechanical Aspects of Resistive and Superconducting Systems.* New York: Wiley; 1969.

35. Kratz R, Wyder P. *Principles of Pulsed Magnet Design*. Berlin: Springer; 2002. doi:10.1017/CBO9781107415324.004.
36. Garrett MW. Axially symmetric systems for generating and measuring magnetic fields. Part I. *J Appl Phys*. 1951;22(9):1091-1107. doi:10.1063/1.1700115.
37. Garrett MW. Thick cylindrical coil systems for strong magnetic fields with field or gradient homogeneities of the 6th to 20th order. *J Appl Phys*. 1967;38(6):2563-2586. doi:10.1063/1.1709950.
38. Kabat D, Cesnak L. Optimisation of inner-notch corrected highly homogeneous superconducting solenoids and their comparison with other coil configurations. *J Phys E Sci Instrum*. 1979;12(Kabat 1975):0-5.
39. Turner R. A target field approach to optimal coil design. *J Phys D Appl Phys*. 1986;19:47-51. papers://e10472a9-d7b6-4cc3-b1fd-411b2c1ecba0/Paper/p1226.
40. Morgan PN, Conolly SM, Macovski A. Resistive homogeneous MRI magnet design by matrix subset selection. *Magn Reson Med*. 1999;41(6):1221-1229. doi:10.1002/(SICI)1522-2594(199906)41:6<1221::AID-MRM19>3.0.CO;2-E.
41. Xu H, Conolly SM, Scott GC, Macovski A. Homogeneous Magnet Design Using Linear Programming. 2000;36(2):476-483.
42. Lugansky LB. Optimal coils for producing uniform magnetic fields. *J Phys E*. 1987;20(7):932-932. doi:10.1088/0022-3735/20/7/528.
43. Schweikert KH, Krieg R, Noack F. A high-field air-cored magnet coil design for fast-field-cycling NMR. *J Magn Reson*. 1988;78(1):77-96. doi:10.1016/0022-2364(88)90158-8.
44. Kruber S, Farrher G, Anzardo E. New magnet design for fast-field-cycling nuclear magnetic resonance. *IEEE Lat Am Trans*. 2013;11(1):251-256. doi:10.1109/TLA.2013.6502812.
45. Grossl G, Winter F, Kimmich R. Optimisation of magnet coils for NMR field-cycling experiments. *J Phys E Sci Instrum*. 1985;18(1 1):3-5.
46. Lips O, Privalov AF, Dvinskikh SV, Fujara F. Magnet Design with High B0 Homogeneity for Fast-Field-Cycling NMR Applications. *J Magn Reson*. 2001;149(1):22-28. doi:10.1006/jmre.2000.2279.
47. Noack F. NMR field-cycling spectroscopy: principles and applications. *Prog Nucl Magn Reson Spectrosc*. 1986;18(3):171-276. doi:10.1016/0079-6565(86)80004-8.
48. Kimmich R, Anzardo E. *Field-Cycling NMR Relaxometry*. Vol 44.; 2004. doi:10.1016/j.pnmrs.2004.03.002.
49. Kimmich R. Field cycling in NMR relaxation spectroscopy: Applications in biological, chemical and polymer physics. *Bull Magn Reson*. 1979;1(4):195-218. [http://nmr-ulm.de/resources/Kimmich\\$2C+Bulletin.pdf](http://nmr-ulm.de/resources/Kimmich$2C+Bulletin.pdf).
50. Morgan P, Conolly S, Scott G, Macovski a. A readout magnet for prepolarized MRI. *Magn Reson Med*. 1996;36(4):527-536. doi:10.1002/mrm.1910360405.
51. Alford JK, Scholl TJ, Handler WB, Chronik BA. Design and Construction of a

- Prototype High-Power B0 Insert Coil for Field-Cycled Imaging in Superconducting MRI Systems. *Concepts Magn Reson Part B Magn Reson Eng.* 2009;35(3):121-132. doi:10.1002/cmr.b.
52. Harris CT, Handler WB, Araya Y, et al. Development and optimization of hardware for delta relaxation enhanced MRI. *Magn Reson Med.* 2014;72(4):1182-1190. doi:10.1002/mrm.25014.
  53. Boesch C, Gruetter R, Martin E. Temporal and Spatial Analysis of Fields Generated by Eddy Currents in Superconducting Magnets: Optimization of Corrections and Quantitative Characterization of Magnet and Gradient Systems. *Magn Reson Med.* 1991;20:268-284.
  54. Hoelscher UC, Jakob PM. Eddy current compensation for delta relaxation enhanced MR by dynamic reference phase modulation. *Magn Reson Mater Physics, Biol Med.* 2013;26(2):249-259. doi:10.1007/s10334-012-0335-6.
  55. de Rochefort L, Lee E, Polello M, Durrasse L, Ferrante G, Rutt BK. Characterization and Compensation of Eddy Current Induced by Insertable dreMR Magnet. In: *International Society for Magnetic Resonance in Medicine.* ; 2012.
  56. Harris CT, Haw DW, Handler WB, Chronik BA. Shielded resistive electromagnets of arbitrary surface geometry using the boundary element method and a minimum energy constraint. *J Magn Reson.* 2013;234:95-100. doi:10.1016/j.jmr.2013.06.010.
  57. Alford J, Sorensen AG, Benner T, et al. Direct Protein Imaging of Inflammation in the Human Hand. *Proc Int Soc Magn Reson Med.* 2011;19:2011.
  58. Araya Y, Martinez-Santesteban F, Handler WB, Harris CT, Chronik BA, Scholl TJ. Nuclear Magnetic Relaxation Dispersion of Murine Tissue for Development of T1 (R1) Dispersion Contrast Imaging. *NMR Biomed.* 2017;(e3789). doi:https://doi.org/10.1002/nbm.3789.
  59. Alford JK, Farrar CT, Yang Y, et al. Direct Albumin Imaging in Mouse Tumour Model. In: *International Society for Magnetic Resonance in Medicine.* Vol 19. ; 2011.
  60. Lee E, de Rochefort L, Ferrante G, Rutt BK. Next generation delta relaxation enhanced MRI with  $\pm 0.36T \Delta B$ . In: *20th Annual Meeting of ISMRM.* Melbourne, Australia; 2012.
  61. Wang Y, Spiller M, Caravan P. Evidence for weak protein binding of commercial extracellular gadolinium contrast agents. *Magn Reson Med.* 2010;63(3):609-616. doi:10.1002/mrm.22214.
  62. Macovski A. MRI: A charmed past and an exciting future. *J Magn Reson Imaging.* 2009;30(5):919-923. doi:10.1002/jmri.21962.

## Chapter 2

### 2 Validated and Verified Design Study of Split Thick Power Solenoids

In this chapter, a software tool is developed to design pulsed solenoid magnets for various applications. Aspects of the design method combine and adapt features of several of the previously mentioned methods (Section 1.5) and employs them in a systematic yet iterative approach to choosing coil parameters. These features include the formalism to describe coils<sup>1,2</sup>, engineering choices<sup>3,4</sup>, and strategies for improving homogeneity<sup>5</sup>. This chapter covers the general design of split thick power solenoids, and applies the method to the creation of a medical device testing platform; a topic related to MRI safety<sup>6</sup>. The motivation and design criteria are examined in detail. The general design method is presented with a description and navigation of design parameter space and performance parameter space. An example design study is conducted for a single-axis, switched magnetic field (dB/dt) exposure system. To validate the design method and simulation code, a suitable coil is constructed and verified to perform as specified.

#### 2.1 Device Testing and Motivation

In a conventional MR system, gradient coils require active shielding to reduce power deposition in nearby conductive surfaces<sup>7,8</sup>. The primary concerns are the structures of the MR system itself, however the rapidly switched gradient fields can also induce eddy-currents in nearby medical devices. This is of growing concern due to the rising number of people with implanted medical devices and their need for MRI scans<sup>9</sup>. These eddy-currents can cause image artifacts by affecting the local magnetic field near the device<sup>10,11</sup>.

Mechanical vibration of the device can occur from the magnetic moment of the eddy currents interacting with the static magnetic field<sup>12,13</sup>. Heating of the device can occur due to resistive losses<sup>14,15</sup>. Additionally, there is concern for malfunction of active implants, such as pacemakers, due to induced voltages on internal circuitry<sup>16</sup>. All of these unwanted interactions are potentially harmful to the patient and thus only devices which are deemed MR conditional or MR safe are allowed into the scanner<sup>17</sup>. For these reasons, it is beneficial to conduct device testing to ensure the compatibility of these devices while in the MR environment.

There are several standards in place on the evaluation, measurement, and reporting of medical device tests<sup>18-20</sup>. ISO/TS 10974:2012 states that the dB/dt root-mean-square (rms) value, pulse shape and width, test duration, and other requirements of gradient-based tests are not always achievable in a clinical MR system, and suggests the use of a separate laboratory electromagnet. This is further evidenced by McCurdy et al. in which surveys of rms gradient strength and slew rate were shown to be much less than what was stated by the manufacturer on clinically-relevant test protocols<sup>21</sup>. The benefit of an external test platform is it avoids the operating expense and difficulties of testing in an MR scanner. Because a coil can be specifically designed for this purpose, the size, power, and cooling requirements would be considerably less. Moreover, it would have the advantage of being able to generate arbitrary pulse sequences, which could operate for longer and with improved performance than clinical MRI scanners, as required for these tests.

Of the aforementioned hazardous effects on medical devices due to switched magnetic fields, only the heating and functional effects can be easily replicated in a standalone electromagnet (as the others require testing in-situ). The devices under consideration are

semi- or permanently implanted devices with medium-sized surface areas of conductive material that may or may not have external leads. This includes active devices such as pacemakers, drug pumps, cochlear implants, and inactive devices such as orthopedic implants.

## 2.2 Methods

The following sections give an overview of the design criteria and other necessary considerations, the design method as applied to a switched field exposure system, construction of a suitable coil, and experimental testing.

### 2.2.1 Field Efficiency and Inductance

Induction heating of a device is proportional to the power dissipated in a conductor, which is proportional to the square of the switching rate of the magnetic field<sup>22</sup>. The voltages induced over a device via Faraday's law are proportional to the dB/dt. Peak dB/dt is calculated as the maximum change in magnetic field over the smallest ramp time with units of T/s. Therefore, it is important to have both a large field shift and high dB/dt for these tests. In consideration of the ohmic resistance,  $R$ , and inductance,  $L$ , of the electromagnet, the time required for a power supply with max voltage output,  $V_m$ , to ramp to max current,  $I_m$ , is

$$t_{rise} = -\frac{L}{R} \cdot \ln\left(1 - \frac{RI_m}{V_m}\right). \quad (2.1)$$

The maximum and rms switching rate are

$$\left(\frac{dB}{dt}\right)_m = \eta \frac{I_m}{t_{rise}}, \quad (2.2a)$$

$$\left(\frac{dB}{dt}\right)_{rms} = (2\pi f) \cdot \eta I_{rms}, \quad (2.2b)$$

where  $\eta$  is the field-efficiency with units of T/A,  $f$  is the frequency of the magnetic field in Hz, and the rms current is  $I_{rms}$ . For best performance, the field-efficiency needs to be maximized, the inductance minimized, and to some extent the magnet resistance needs to be minimized too (proportional to the dissipated power,  $P$ , in the coil).

To emulate and surpass the field strength and dB/dt of a gradient coil, the worst-case test configurations were considered. On a 3.0 T Siemens Prisma scanner, the reported system maximum slew rate and gradient strength are 200 T/m/s and 80 mT/m, respectively<sup>23</sup>. The worst case would occur when the test device is oriented perpendicular to the changing magnetic field at 30 cm from isocenter (limited by the size of the bore), and thus would be approximately 60 T/s and 24 mT. However, ISO/TS 10974 requires conditions which exceed these values for dB/dt testing. Therefore, the target for minimum dB/dt and field shift for the proposed coil were 100 T/s and 30 mT.

### 2.2.2 Exposure Region and Field Uniformity

It is desirable to have a large exposure region so that multiple concurrent device tests could occur. This would increase throughput and reduce cost (to the device manufacturer, and perhaps the receiving patient). Moreover, for radiated field tests (functional tests) the voltages induced on devices with extrinsic leads is proportional to the flux, which is limited by the radius of the coil<sup>18</sup>. The magnetic field would not have a spatial gradient (like a gradient coil), but would be relatively uniform such that devices are

exposed to the same conditions regardless of placement. A homogeneous field would also increase measurement precision, simplify analysis, and yield higher field efficiency. The inhomogeneity,  $H$ , of a coil over some volume,  $v$ , is defined as the range of the field over a surface,  $S$ , relative to the field in the center,  $B_0$ . This indicates that the maximum deviation of any point within  $v$  with respect to any other point will be less than or equal to  $H$ .

$$H_v = \frac{\Delta B_S}{B_0} \cdot 100\% \quad (2.3)$$

A practical way to improve the field uniformity of a solenoid is use of a central, axial gap. However, this should be limited due to the negative effects on field shift and  $\text{dB}/\text{dt}$ <sup>24</sup>. For the proposed coil, the preferred clear bore diameter was at least 24 cm, with a region of 5% inhomogeneity to be as large as possible in the xy-plane.

### 2.2.3 Engineering Considerations and Performance Limitations

The main limitations on the performance of a pulsed magnet are the mechanical stress, thermal management, and the source of power<sup>25</sup>. Mitigation of the first two boundary conditions can be achieved through appropriate engineering choices. The choice of power supply can be based on the desired performance of the coil, but is often limited by the realities of cost and availability<sup>1</sup>. The tensile strength of the coil bore helps to relieve mechanical stress. Forces and torques are relatively minor for coils of this application (given the combination of coil size, number of windings, type and strength of produced field, and external magnetic environment), and will not be considered further. A thermally conductive epoxy was used during construction, which provides compressive strength and aids in heat dissipation. The coil was cooled with forced water using a recirculating chiller with an approximate cooling capacity of 6 kW (Lytron Inc., Kodiak Chiller RC045).

Hollow conductors are an excellent strategy for cooling and have been used previously to build gradient coils and other resistive electromagnets<sup>3</sup>. But ultimately, for this application, thermal management was just accepted and was not included in the design process beyond these basic engineering choices.

## 2.2.4 Design Method

The windings of the solenoids are modeled as singular filamentary loops of copper wire, of which each loop is discretized into an array of smaller wire elements. The entire coil is described by thousands of these elements, from which calculations of magnetic fields and inductance are achieved using the Biot-Savart law and Neumann's formula, respectively<sup>8</sup>. Magnetic field calculations using the filamentary approach are accurate as long as the distance between the source and observation point are large compared to the wire diameter<sup>25</sup>. However, the geometry of the coil is described in terms of inner radius, finite wire cross-section, number of radial layers ( $NR$ ), number of axial windings ( $NZ$ ), and the gap size. Resistance calculations take into account the wire cross-section as well as coil temperature, but do not consider frequency effects.

In this chapter, a tool was developed to design pulsed solenoid magnets. The tool was used to design a switched-field exposure system for testing medical devices. The design parameter space (inner radius, wire size,  $NR$ ,  $NZ$ , gap) was narrowed down until a suitable coil design was chosen based on the performance parameter space ( $B$ ,  $H$ ,  $dB/dt$ ). The process went as follows. First, a range for inner radius were determined by finding where performance was too low and too high. Then a selection was made based on material availability. Wire gauge and fill factor were chosen based on previous experience in

constructing resistive magnets. The geometry was then systematically varied while partially setting the gap. The performance constraints were applied and the candidate coils were examined. A suitable coil was chosen and the design parameters were iteratively fine-tuned.

### 2.2.5 Construction

The actual manufactured coil is described in Section 2.3.1, with a design summary in Table 2.1. The coil was wound upon a PVC former with a clear bore inner diameter of 25.3 cm. The copper wires were double insulated with Kapton tape then wound in pairs onto the coil with a small jog after each full turn. A short electrical connection was used to connect the two layers in series. Brass manifolds were used to manage electrical and hydraulic inputs and outputs. During the winding process a low-viscosity epoxy (Epoxies, Etc., 50-3100, with catalyst 150) was applied to set the windings in place. Afterwards, thermocouples were placed at several points on the solenoid so that heating could be monitored during operation. An electrostatically shielded wire loop circumscribes the coil around the center of the coil, with a coaxial output connector attached. This loop senses the changing magnetic field produced throughout the entire central cross-section of the coil via Faraday induction.

### 2.2.6 Experimental Testing

A field map was conducted using a 3-axis Hall probe (Senis AG, Model F3A), a DC power supply (Keysight Technologies, Model 6032A), and a rigid positioning apparatus. The current was set to 20.0 A in current-controlled mode and measurements of the magnetic field were taken in centimeter increments across the yz-plane of the exposure

region. The range of measurements spanned from -1 to 14 cm in the axial direction, and from -10 to 12 cm radially, with respect to the coil center. To generate a map of the entire exposure region, some data were mirrored, and the final number of data points increased from 368 to 725. A simulated field map was made of the modeled coil and calculated at the same points. The two maps were compared by means of the reduced chi-squared test. Since the Biot-Savart law breaks down when the observation point is close to the source point, the region for evaluating the two field maps was set to [-10, 10] cm in the y and z direction.

The field strength and dB/dt were calculated from Hall probe measurements at the isocenter, when the coil was driven at 350 V, 90 A, and 2500 Hz, with a triangular waveform. Waveforms were captured using a LabView program (National Instruments), written by Jack Hendricks, from which field efficiency was calculated as the peak-to-peak voltage divided by the input current, and dB/dt was calculated from the slope of the waveform. The coil was cooled by tap water during the field map and performance experiments.

The coil inductance and resistance were measured at frequencies of 12 Hz, 1 kHz, and 10 kHz with an LCR meter (Instek, LCR 817). A second calculation of dB/dt was done using Equations (2.1) and (2.2a), with experimental values used for inductance resistance, current, and voltage.

## 2.3 Results

### 2.3.1 Coil Design

For this coil, calculations were based upon square, hollow, copper wires of 5 mm by 5 mm with a 3-mm-diameter hole, and an available power amplifier with maximum voltage and current of 350 V and 430 A, respectively (Copley Controls Corp, Model 266 High Power Amplifier). It was decided to model each coil turn as composed of two electrically parallel conductors. The effect this has on performance is to double the dB/dt and reduce the resistance, at the expense of halving the field shift. This effectively doubles the wire width in the axial direction. By also allowing for wire insulation and a small fill factor, the effective wire dimensions were 5.3 mm by 10.6 mm. Initial calculations revealed that the inner radius of the coil should be between 12 and 15 cm. Above 15 cm, none of the minimum criteria could be achieved, and below 12 cm the performance was much higher than necessary. The wires were wound onto a PVC tube with outer diameter of 27.2 cm specifically because of the availability of a tube of that size. Customarily, the ideal coil radius would be precisely determined from the design optimization, however, it was sufficient for this application to simply choose from within an acceptable range.

After settling on an inner radius, a grid search of dimensional parameters,  $NR$  and  $NZ$ , was conducted to systematically vary the geometry of possible coils. During the search, a simultaneous optimization of the gap was done, for each individual coil, which would yield the best uniformity over a 6-cm-diameter of spherical volume (DSV) using a bounded, nonlinear, function minimization *fminbnd* in MATLAB (R2016b, MathWorks). The axial gap was created by smoothly separating the two halves of the coil (as opposed to simply removing windings from the coil center). Figure 2.1 shows the field inhomogeneity

for all coils with no gap and after gap optimization. The gaps (on the order of centimeters) improves the uniformity of the coils by an order of magnitude. The coils become increasingly more uniform as length increases, but this will eventually approach some limit and will not validate the increased power dissipated in the coil, as illustrated in Figure 2.2. The constraints for minimum field shift and dB/dt were applied and the remaining region of parameter space was used to choose a coil design. Figure 2.3 and Figure 2.4 show the field shift and dB/dt for the restricted view of parameter space.

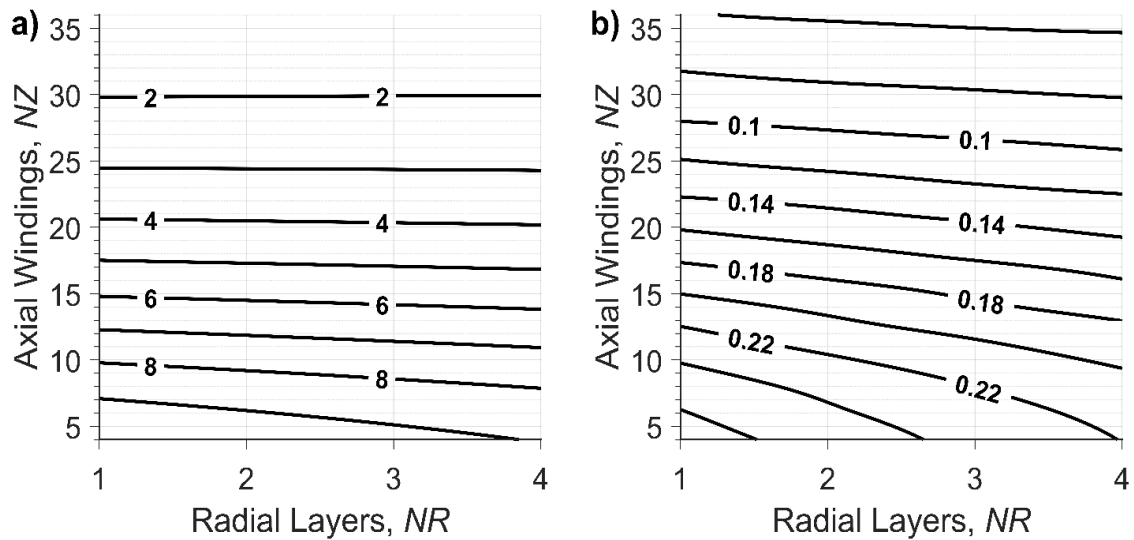


**Figure 2.1:** Field uniformity as calculated over a 6-cm-diameter sphere in percent deviation from the central field for coils with (a) no central gap and (b) optimized gap. The distance between contour lines is 1% in (a) and 0.02% in (b).

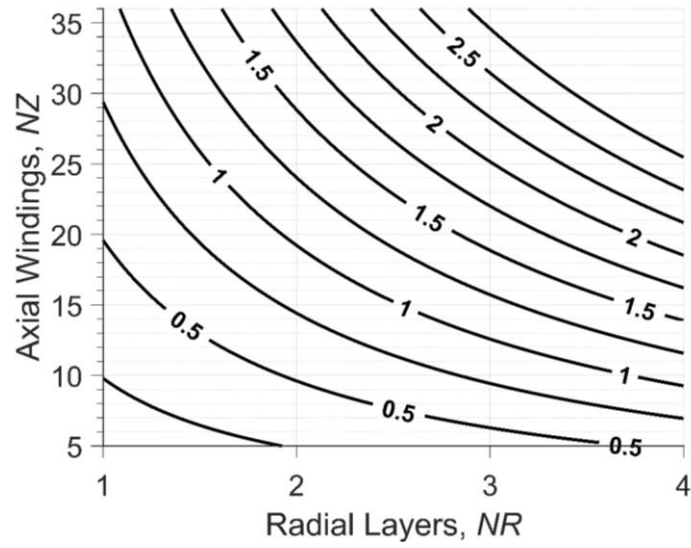


**Figure 2.2:** Dissipated power in [kW] for uniform current density solenoids, based on coil resistance and current of 250 A. In the calculated region, the dissipated power increases with total number of windings.

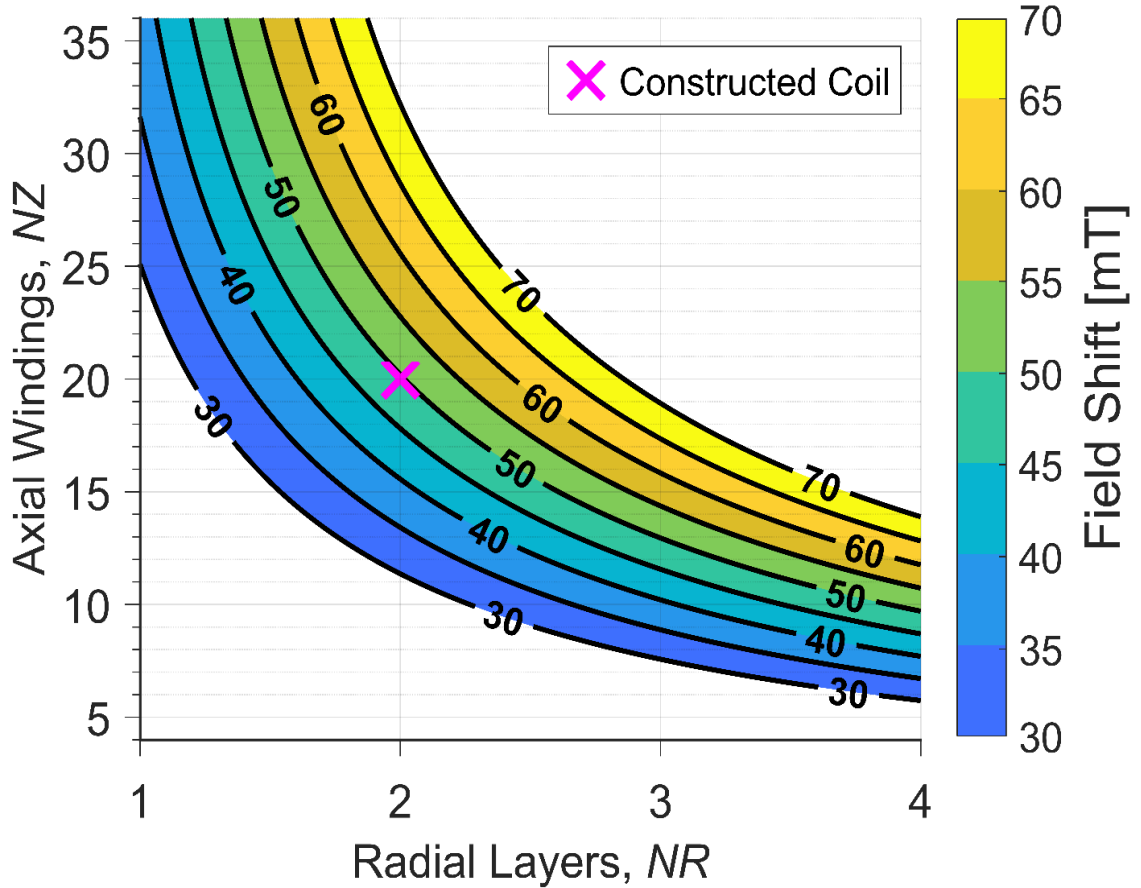


**Figure 2.3:** Maximum central magnetic field in [mT] for uniform current density solenoids with current of 430 A. All coils have an inner radius of 13.6 cm and have an axial gap individually adjusted to achieve best field uniformity over a 6 cm DSV. The dependence of central field as a function of radial layers and axial windings is shown. The distance between contour lines is 5 mT. White regions of parameter space were rejected for failing to meet the minimum performance targets: 100 T/s for dB/dt and 30 mT for field shift. The X marker indicates that the constructed coil had 2 radial layers of 20 winding pairs.

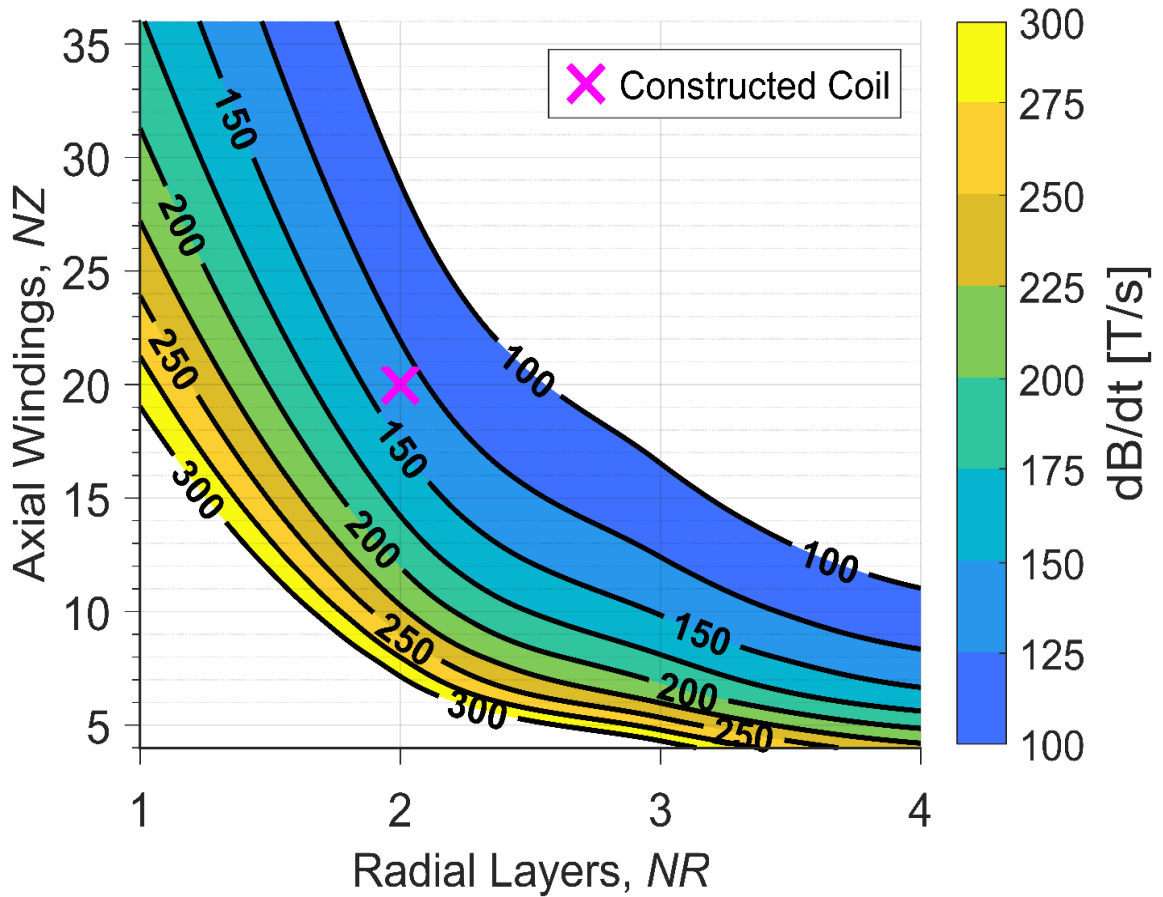


**Figure 2.4:** Maximum dB/dt in [T/s] for uniform current density solenoids, with 430 A and 350 V. All coils have an inner radius of 13.6 cm and have an axial gap adjusted to achieve best field uniformity over a 6 cm DSV. The dependence of dB/dt as a function of coil geometry is shown. The distance between contour lines is 25 T/s. White regions of parameter space were rejected for failing to meet the minimum performance targets: 100 T/s for dB/dt and 30 mT for field shift. The X marker indicates that the constructed coil had 2 radial layers of 20 winding pairs.

Of the remaining parameter space, all coils meet the minimum requirements, however for all coils with three layers there was a coil with two layers that outperformed in both dB/dt and field shift. On the other hand, for single layer coils to have equivalent performance as double layer coils, the coils require a high number of axial windings, and thus have significantly high amounts of dissipated power. Additionally, the coil length doubles and makes the system unwieldy. The chosen coil had 2 layers of 22 axial wire-pairs. After choosing the coil, the gap size was readjusted in the following way. The DSV under 1% inhomogeneity was calculated as a function of increasing gap. The region size steadily increased to a maximum which occurred with a gap of 6.1 cm. The largest radius in the xy-plane under 5% inhomogeneity occurred with a gap of 2.4 cm, and decreased linearly with gaps larger than this. The intersection of the two lines occurred at 5.41 cm, where both regions were 9 cm. This was the gap chosen for this coil. A summary of the design for the coil is shown in Table 2.1. This coil has a calculated dB/dt and field shift, both well above the minimum target, at values of 136 T/s and 51 mT, respectively. The dissipated power calculated using rms current is 1 kW; much lower than the 6 kW cooling capacity of the chiller. A computer aided design drawing of the coil chosen for construction is shown in Figure 2.5, drawn by Justin Peterson.

Minor imperfections and wire twisting during the construction process caused unwanted voids between windings. This led to the inability to place all 22 windings on the coil. Consequently, the constructed coil had 2 layers of 20 windings. Figure 2.6 shows the coil in three stages of development: during construction; a partially completed but uncovered coil, having resistance and inductance measured; and the completed coil undergoing field measurements.

**Table 2.1:** Design summary of electromagnetic and geometric parameters for the gradient field exposure system.

Property	Value	Units
Coil Geometry		
Inner Radius	13.60	[cm]
Outer Radius	14.66	[cm]
Radial Layers	2	
Axial Windings <sup>a</sup>	20	
Gap Length	5.41	[cm]
Total Length	26.61	[cm]
Radial Wire Width	5.3	[mm]
Axial Wire Width <sup>a</sup>	10.6	[mm]
Performance		
Resistance	16.6	[mΩ]
Inductance	300	[μH]
Efficiency	0.118	[mT/A]
DSV 1% <sup>b</sup>	9.0	[cm]
XY-Plane 5% <sup>b</sup>	18.0	[cm]
dB/dt <sup>c</sup>	136	[T/s]
Field Shift	51	[mT]
dB/dt, rms <sup>d, e</sup>	65	[T/s]
Field Shift, rms <sup>e</sup>	30	[mT]
Power <sup>e</sup>	1.04	[kW]
Power Supply		
Current, max	430	[A]
Current, rms	250	[A]
Voltage, max	350	[V]

<sup>a</sup> Parallel wire-pairs (40 individual windings)

<sup>b</sup> Largest diameter below listed inhomogeneity

<sup>c</sup> Rise time of 0.37 ms

<sup>d</sup> Frequency of 350 Hz

<sup>e</sup> Dissipated power, using rms current

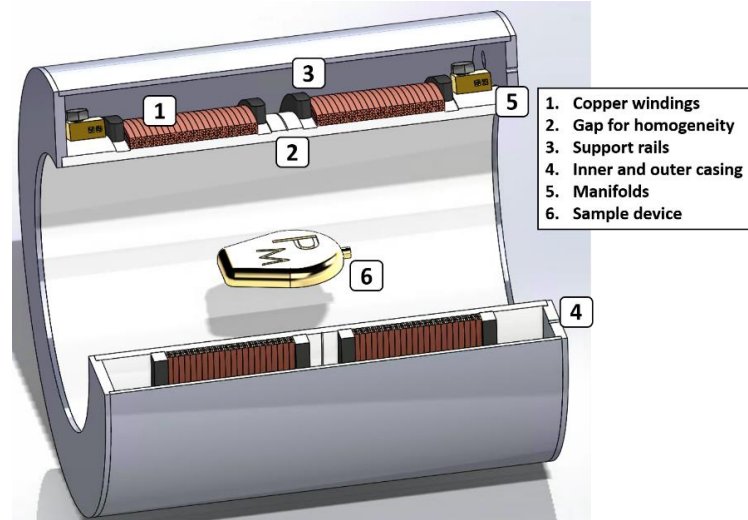


**Figure 2.5:** 3D drawing of the switched field exposure system. In the center is a sample medical device that would require MR compatibility testing. Electrical and hydraulic connections to the manifolds are not shown.

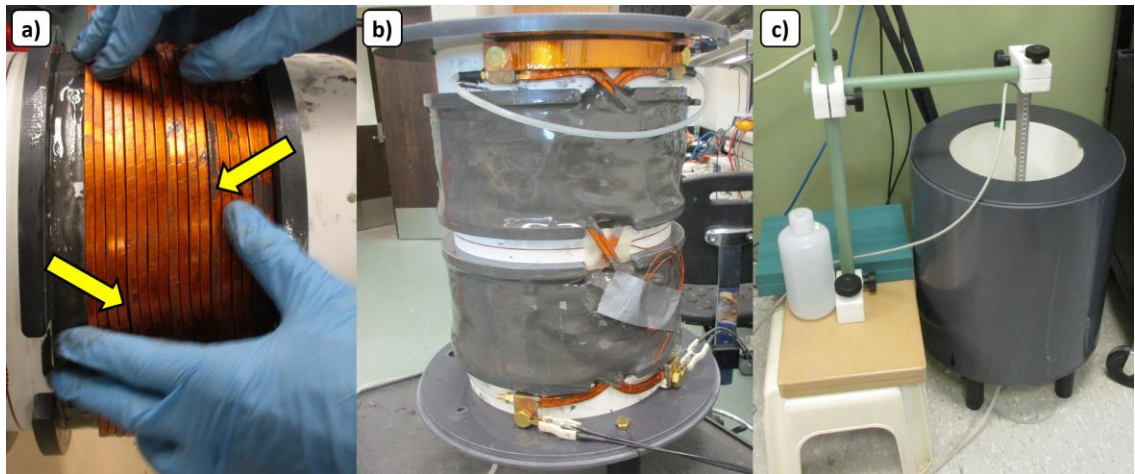


**Figure 2.6:** a) Close-up of the windings during construction. Voids can be seen between windings due to wire-twisting (arrows). b) Side view of the uncovered coil undergoing inductance and resistance measurements. The copper band at the top connects the two layers. Water hoses attached to the manifolds provide cooling through the hollow wires. The dB/dt monitoring winding is located between the upper and lower coil windings. c) The completed coil with positioning apparatus.

### 2.3.2 Experimental Validation

There were several sources of error identified in the field map experiment. These sources, the estimated uncertainty and mean absolute error are summarized in Table 2.2. The experimental central magnetic field strength was 2.25 mT. The simulated field map was normalized to this value (accounting for one fitted parameter). The uncertainty in the x-position accounts for the possibility of a one-degree error in the angle of the positioning system, however the mean value is still small because of symmetry across the yz-plane. The constructed coil was modeled as having all ten windings on each half pushed towards the center as much as possible, such that the gap would still be 5.41 cm. However, there is error in the model that occurs due to the voids between windings and the extra space. The error due to spatial variance of the coil windings was estimated by generating several similar coils, with slightly different wire positions and fill factors. The simulated fields were subtracted from the field of the original-model coil, after normalizing to the same central field, then averaged. This accounts for another fitted parameter for the reduced chi-squared test.

Figure 2.7 shows both the experimental and simulated field maps in the yz-plane. Contour lines on the maps show 1%, 5%, and 10% deviation of field from the central value. The region in the xy-plane less than 5% inhomogeneity is 18 cm (indicated by the arrow), and 17.4 cm for the constructed coil (although with a small asymmetry). Similarly, the DSV under 1% is 9 cm and 8.6 cm. Both regions have a percent deviation of less than 5% from the modeled coil.

**Table 2.2:** Error and uncertainty in the field map experiment. The error in the model was estimated by varying the fill factor of the windings, due to the extra space allowed by dropping a winding-pair during construction. The error in x-position was a function of position. The mean absolute error from each source is shown. The central magnetic field was 2.25 mT.

Source of Error	Uncertainty	Mean Absolute
x-position	$\pm 1\text{-}5$ mm	0.0002
y-position	$\pm 1$ mm	0.003
z-position	$\pm 1$ mm	0.004
Power supply	$\pm 0.05$ A	0.006
Hall probe	statistical	0.0005
Model	wire spacing	0.02

The chi-squared and reduced chi-squared between the simulated and experimental field map were  $\chi^2 = 432$  and  $\chi_r^2 = 0.98$ , respectively. The probability that repeated field map experiments would yield a  $\chi_r^2$  larger than 0.98, with 439 degrees of freedom is  $0.58^{26}$ . Note that for a perfect match of a data set to its parent distribution, the  $\chi_r^2$  is 1 and the probability is 0.5. The errors were larger than the residuals 74% of the time, just larger than the standard 68% confidence interval. These values indicate a good fit to the model, but that the error is slightly overestimated. This is due to the discrepancy between the modeled and constructed coil dominating the other sources of error by an order of magnitude.

The performance properties of the coil are summarized in Table 2.3. Uncertainty in current and voltage were taken from the sensitivity listed in the amplifier specification sheet (Copley Controls Corp, Model 266). The uncertainty in time was  $\pm 1$   $\mu$ s based on the sampling rate of data collection. The calculated resistance is lower than the 12 Hz measured resistance because it does not take into account the extra connections required during

construction and electrical set up. The resistance increases with frequency because of skin depth and impedance, which were also not modeled. Skin depth also has a small influence on inductance, which is why the value drops slightly with increased frequency; however, the results show good agreement. This is especially true considering the frequency range of testing will be below 3000 Hz.

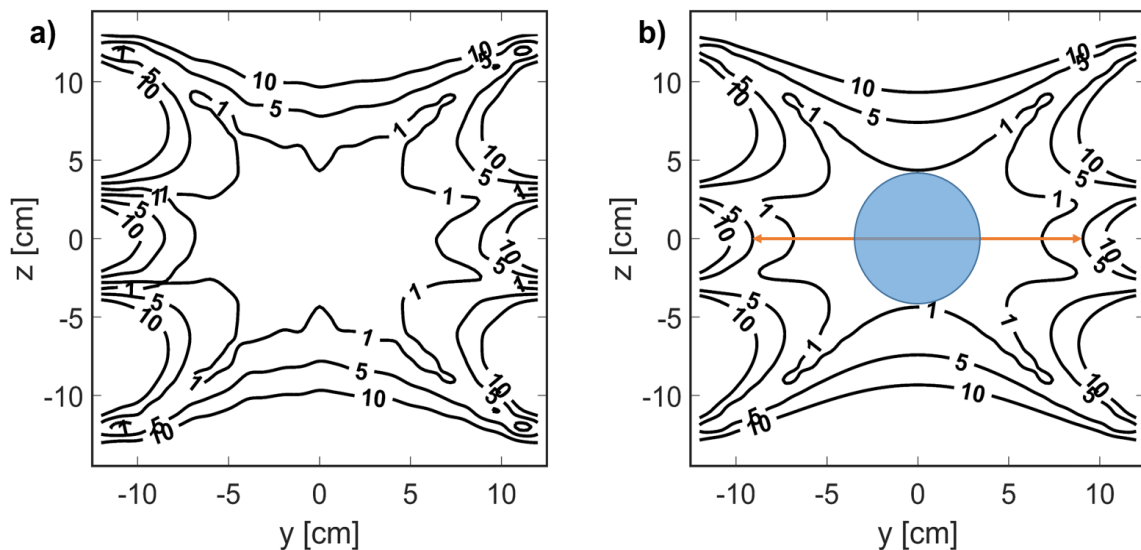


**Figure 2.7:** Field uniformity map over the  $yz$ -plane of the testing region, normalized to the central value. a) The measured field map for the constructed coil, and b) the predicted field map for the modeled coil. Contour lines show 1%, 5%, and 10% deviation from the  $z$ -component of the magnetic field at the center. The arrow indicates the region of less than 5% inhomogeneity in the  $xy$ -plane is 18 cm. The circle indicates the central spherical region of less than 1% inhomogeneity has a 9 cm diameter.

Within the estimated uncertainty, there is agreement in coil efficiency, and thus maximum field strength. The originally calculated value of  $dB/dt$  was high because the modeled resistance is too low. However, when  $dB/dt$  is calculated again with the experimental value for resistance, the results agree within the uncertainty.

**Table 2.3:** Comparison of design and experimental performance.

Property	Designed Coil	Constructed Coil		
Frequency	DC	12 Hz	1 kHz	10 kHz
Resistance [mΩ]	16.6	21.2	54.2	306
Inductance [μH]	300	306	301	291
Efficiency [mT/A]	0.118	0.116 ± 0.004		
Field Shift [mT]	51	50 ± 2		
dB/dt [T/s]	127 ± 5 <sup>a</sup>	124 ± 4		

<sup>a</sup> Calculated using experimental value of resistance.

## 2.4 Discussion

The constructed coil has demonstrated the ability to easily design a pulsed magnet that will accurately achieve performance specifications. The chosen coil had 2 layers of 22 wire-pairs, but the constructed coil only had 20 wire-pairs. The reason was not because the fill factor was too small, but because of an unanticipated excess in wire twisting due to the engineering choice of having the electrical parallelization of wires to occur in the axial direction. An improved construction method would be to either parallelize the layers instead, or wind in a low-angle helical pitch as opposed to a jogged winding method.

The simulation code was validated by the accuracy of the field shift, dB/dt, and field maps when compared to the modeled coil. The filamentary approach to modeling coil windings is sufficient for applications with slightly relaxed homogeneity requirements, such as this one. Finite cross-section simulation, where square-wires are modeled with many filaments, is more accurate at magnetic field calculations, but at the expense of calculation time. More sophisticated methods to calculate resistance, which could include frequency-based skin effect and proximity effects, could be implemented but are unnecessary for relatively low frequency applications. Future tests should include full

characterization of  $dB/dt$  as a function of frequency with respect to the amplifier, as well as conducting device tests with full thermal monitoring.

The software tool developed in this chapter can be applied to the design of a dreMR coil<sup>27</sup>. In addition to the primary windings, dreMR coils require an active shield to limit the interactions between the primary solenoid and the host MR system. The repeated field-shifts of the dreMR coil can deposit energy in the host cryostat and superconductive windings in the form of eddy-currents, which can lead to field instability and, consequently, frequency errors during image acquisition. The shield is composed of counter-windings at a radius larger than the primary, designed to minimize the self-inductance and inductive coupling with the host system by reducing the fringe field of the dreMR coil. There are published methods detailing the design of active shields for any arbitrary primary magnet<sup>28</sup>, which have been used for shielding dreMR coils<sup>29</sup>. The design of the shield does not greatly influence the design of the primary beyond limiting the outer radius. In fact, the preferred method for designing a dreMR shield is using an accurate model of the constructed primary coil as input into the shield design<sup>29</sup>.

For the dreMR primary, the priorities are maximizing field-efficiency, minimizing dissipated power, and being able to ramp hundreds of milliteslas in tens of milliseconds. There would be no need to parallelize the windings since the required  $dB/dt$  is relatively small. The efficiency of the coil would have to be increased without increasing the resistance. A larger sized wire could not be used (which would reduce resistance) because if wire cross-section increases then total number of wires must decrease, given constant coil dimensions. Therefore, the power-efficiency needs to be maximized under the constraint of limited coil size. The idea here is to use non-uniform current density

distributions to achieve higher power-efficiency with either similar resistance, or increased cooling capacity. One way to achieve this would be to use tightly packed solid wire on the inner layers near the center. The solid wire would have lower resistance than the hollow square wire, but would require their own cooling strategy, which could decrease the fill factor. Another way could be to divide the coil into sections of radially graduated current density<sup>2</sup>. For the design of such a coil, the wire size could not be so easily withdrawn from parameter space as it was for the dB/dt exposure system. A strategy would be to rewrite the formalism to describe the geometry in terms of continuous ratios of the inner radius<sup>1</sup>, as in Section 1.5.1. The bulk cross-section of each coil section (including any gaps or notches) could be determined using the systematic approach described earlier. Once a coil (or very small region of parameter space) is chosen, a transition back to discrete formalism would be done to set the finite wire width and integer number of windings. The final step would be to iteratively adjust the individual parameters until no significant improvements could be made. In this last stage, it is often necessary to make secondary considerations where applicable, including: cost, weight or size of the coil, allowing for margins on performance targets, and minimum inductance load of the power source.

The design of a full dreMR system requires more components than just the primary coil. One needs to take into account the host MR system, the RF coil, a switchbox to ensure electrical isolation during image acquisition, and active shielding<sup>4,29,30</sup>. These additional aspects of a dreMR system are outside the scope of the current work.

## 2.5 Conclusions

Given the increasingly diverse application and performance demand of pulsed magnet coils, there exists no universally ideal coil design. Consideration of conflicting requirements as well as limited resources will inevitably lead to a series of choices and trade-offs to make. The objective of this work was to develop a tool to guide the design of pulsed solenoid magnets. This was demonstrated through the design of a gradient-field exposure system. The properties and performance of the constructed coil agree with the designed coil to within the range of uncertainty. There is a large region of less than 5% homogeneity, which means multiple concurrent device testing is possible. The specifications of the coil exceed the requirements of ISO/TS 10974:2012 and the coil is ready to begin device testing and labelling device MR compatibility.

## 2.6 References

1. Montgomery DB. *Solenoid Magnet Design. The Magnetic and Mechanical Aspects of Resistive and Superconducting Systems*. New York: Wiley; 1969.
2. Kabat D, Cesnak L. Optimisation of inner-notch corrected highly homogeneous superconducting solenoids and their comparison with other coil configurations. *J Phys E Sci Instrum.* 1979;12(Kabat 1975):0-5.
3. Handler WB, Harris CT, Scholl TJ, et al. New head gradient coil design and construction techniques. *J Magn Reson Imaging*. 2014;39(5):1088-1095. doi:10.1002/jmri.24254.
4. Alford JK, Scholl TJ, Handler WB, Chronik BA. Design and Construction of a Prototype High-Power B0 Insert Coil for Field-Cycled Imaging in Superconducting MRI Systems. *Concepts Magn Reson Part B Magn Reson Eng*. 2009;35(3):121-132. doi:10.1002/cmr.b.
5. Garrett MW. Axially symmetric systems for generating and measuring magnetic fields. Part I. *J Appl Phys*. 1951;22(9):1091-1107. doi:10.1063/1.1700115.
6. Schenck JF. Safety of strong, static magnetic fields. *J Magn Reson imaging*. 2000;12(1):2-19.
7. Haacke EM, Brown RW, Thompson MR, Venkatesan R. Magnetic resonance imaging: physical principles and sequence design. 1999. *New York A John Wiley*

Sons. 1999.

8. Jackson JD. Jackson - Classical Electrodynamics 3rd edition. *Am J Phys.* 1999;67:841.
9. Kalin R, Stanton MS. Current clinical issues for MRI scanning of pacemaker and defibrillator patients. *Pacing Clin Electrophysiol.* 2005;28(4):326-328.
10. Graf H, Steidle G, Martirosian P, Lauer U a., Schick F. Metal artifacts caused by gradient switching. *Magn Reson Med.* 2005;54(October 2004):231-234. doi:10.1002/mrm.20524.
11. Bannan K El, Handler WB, Wyenberg C, Chronik BA, Salisbury SP. Prediction of force and image artifacts under MRI for metals used in medical devices. *Mechatronics, IEEE/ASME Trans.* 2013;18(3):954-962.
12. Graf H, Lauer UA, Schick F. Eddy-current induction in extended metallic parts as a source of considerable torsional moment. *J Magn Reson Imaging.* 2006;23(4):585-590.
13. Martire DJ, Wawrzyn K, Handler WB, Chronik BA. Measuring Gradient-Induced Vibration of a Conductive Device using Laser Doppler Vibrometry at 3T. In: *24th Annual Meeting of International Society of Magnetic Resonance in Medicine.* Singapore; 2016.
14. Graf H, Steidle G, Schick F. Heating of metallic implants and instruments induced by gradient switching in a 1.5-Tesla whole-body unit. *J Magn Reson Imaging.* 2007;26(5):1328-1333. doi:10.1002/jmri.21157.
15. El Bannan K, Handler W, Chronik B, Salisbury SP. Heating of metallic rods induced by time-varying gradient fields in MRI. *J Magn Reson Imaging.* 2013;38(2):411-416.
16. Nazarian S, Beinart R, Halperin HR. Magnetic resonance imaging and implantable devices. *Circ Arrhythmia Electrophysiol.* 2013;6(2):419-428. doi:10.1161/CIRCEP.113.000116.
17. Shellock FG, Woods TO, Crues III J V. MR Labeling Information for Implants and Devices: Explanation of Terminology 1. *Radiology.* 2009;253(1):26-30.
18. ISO. ISO/TS 10974 Assessment of the safety of magnetic resonance imaging for patients with an active implantable medical device. 2012.
19. American Society for Testing Materials (ASTM). F2052-15: Standard Test Method for Measurement of Magnetically Induced Displacement Force on Medical Devices in the Magnetic Resonance Environment. 2015. doi:10.1520/F2052-14.2.
20. IEC. IEC 60601-2-33. Medical Electrical Equipment--Part 2-33: Particular requirements for basic safety and essential performance of magnetic resonance equipment for medical diagnosis. 2010.
21. Mccurdy CM, Handler WB, Peterson JC, Chronik BA. Clinically Relevant Gradient and RF Field Exposure Levels for General Neuro MRI Protocols at 3.0 T. In: *25th Annual Meeting of International Society of Magnetic Resonance in Medicine.*

Honolulu, HI; 2017.

22. Davies J, Simpson P. *Induction Heating Handbook*. London, UK: McGraw-Hill Book Company Limited; 1979.
23. MAGNETOM Prisma. Siemens Healthcare GmbH. <https://www.healthcare.siemens.com/magnetic-resonance-imaging/3t-mri-scanner/magnetom-prisma/features#00271890>. Accessed November 20, 2017.
24. Garrett MW. Thick cylindrical coil systems for strong magnetic fields with field or gradient homogeneities of the 6th to 20th order. *J Appl Phys*. 1967;38(6):2563-2586. doi:10.1063/1.1709950.
25. Kratz R, Wyder P. *Principles of Pulsed Magnet Design*. Berlin: Springer; 2002. doi:10.1017/CBO9781107415324.004.
26. Bevington PR, Robinson DK. Data Reduction and Error Analysis for the Physical Sciences, 2nd edn. *Comput Phys*. 1992;7(4):324. doi:10.1063/1.4823194.
27. Alford JK, Rutt BK, Scholl TJ, Handler WB, Chronik BA. Delta relaxation enhanced mr: Improving activation - Specificity of molecular probes through R1 dispersion imaging. *Magn Reson Med*. 2009;61(4):796-802. doi:10.1002/mrm.21933.
28. Harris CT, Haw DW, Handler WB, Chronik BA. Shielded resistive electromagnets of arbitrary surface geometry using the boundary element method and a minimum energy constraint. *J Magn Reson*. 2013;234:95-100. doi:10.1016/j.jmr.2013.06.010.
29. Harris CT, Handler WB, Araya Y, et al. Development and optimization of hardware for delta relaxation enhanced MRI. *Magn Reson Med*. 2014;72(4):1182-1190. doi:10.1002/mrm.25014.
30. Araya YT. Delta Relaxation Enhanced Magnetic Resonance - Development and Application of a Field-Cycling Contrast Mechanism. 2013;(May):100.

## Chapter 3

### 3 Improved Contrast in DreMR Imaging at 0.5T through Optimized Polarization Sequences

In this chapter, a simulation tool was developed to model tissue magnetization under a time-varying magnetic field. A brief review of theory is presented along with new improvements. This tool was validated and verified through numerical analysis and comparison of simulation with in-vitro images. It is then applied to two applications relating to delta relaxation enhanced magnetic resonance<sup>1</sup>. The first is on how to maximize  $T_1$ -weighted contrast between two tissues using field-cycling. The second explores the implementation of dreMR at a field strength lower than the standard clinical 1.5 T strength. Novel polarization sequences of the dreMR subtraction technique are presented which optimize  $T_1$ -dispersion based contrast at 0.5 T. The results demonstrate that the algorithm can be used to optimize pulse sequences that are specific to the application and the tissues involved, and how signal from any given tissue can be suppressed in the final image.

#### 3.1 Theory

Numerical simulation of MRI is an important tool in a variety of research areas. Simulation has been used to optimize pulse sequences, investigate causes of image artifacts, and as a general educational tool. The complete simulation of MRI experiments extends far beyond solving the Bloch equations<sup>2</sup>, making it a computationally demanding task. At the forefront of this task is the accurate simulation of voxels composed of huge number of isochromats to simulate intra-voxel heterogeneity, over a high number of small time steps<sup>3,4</sup>. For this reason, many approaches reduce the problem by considering

analytical solutions with various approximations applied to limiting situations<sup>5-8</sup>. However, because no general closed form solution to the Bloch equations exists, numerical simulation is a necessity. There are several comprehensive simulators that can generate realistic images and can make accurate and efficient predictions of MRI experiments<sup>3,4,9,10</sup>. However, much sparser in the literature is the implementation of solutions to the Bloch equations under field-cycling conditions. In these cases, analytical solutions no longer apply, and the problem tends towards being numerically ill-conditioned<sup>6</sup>.

In field-cycling applications<sup>11</sup>, the z-component of the magnetic field is time-varying. The time-varying Bloch equations are

$$\frac{dM_z(t)}{dt} = R_1(B_z(t)) \cdot (M_0(B_z(t)) - M_z(t)) \quad (3.1)$$

$$\frac{dM_{xy}(t)}{dt} = -i\gamma M_{xy}(t)B_z(t) - R_2(t)M_{xy}(t) \quad (3.2)$$

where  $\gamma$  is the gyromagnetic ratio and  $M_0$  is the equilibrium magnetization. The small number of papers that attempt to solve these equations (usually just Equation (3.1)) typically use simplifications of the field-cycling sequence to adopt analytical solutions. The most common form is a mid-ramp approximation using step-functions, which can unfortunately result in relative error on the order of tens of percent<sup>12-15</sup>.

The general solution to the time-varying Bloch equations can be found by using an integrating factor technique (ignoring RF pulses, gradients, and diffusion, etc.),

$$M_z(t) = e^{-\int_{t_0}^t R_1(\tau) d\tau} \cdot \int_{t_0}^t M_0(\tau) R_1(\tau) \cdot e^{\int_{t_0}^{\tau} R_1(\tau') d\tau'} d\tau + M_z(t_0) e^{-\int_{t_0}^t R_1(\tau) d\tau}, \quad (3.3)$$

$$M_{xy}(t) = M_{xy}(t_0) \cdot e^{-i\varphi(t)} \cdot e^{\int_{t_0}^t R_2(\tau) d\tau} \quad (3.4)$$

where the phase is  $\varphi(t) = \gamma \int_{t_0}^t B_z(\tau) d\tau + \varphi(t_0)$ . In the case where  $\vec{B}(t) = B_0 \hat{z}$ , the equilibrium magnetization and relaxation rates are constants, and the solution for  $\vec{M}(t)$  simplifies to the regular analytical solution (Equation (1.6a)). For the case where  $B_z(t) = B_0 \pm \Delta B$ , and ramp times are neglected, the expression for longitudinal magnetization is

$$M_{z\pm}(t) = M_{0\pm}(1 - e^{-R_{1\pm}t}) + M_z(t_0)e^{-R_{1\pm}t}, \quad (3.5)$$

where  $M_{0\pm} = \kappa(B_0 \pm \Delta B)$  and  $\kappa$  corresponds to the non-field-terms in Equation (1.1), and the relaxation rate is  $R_{1\pm} = R_1(B_z(t))$ . However, making such an approximation unnecessarily decreases the accuracy of the calculation.

The approach taken in this chapter is a focused model of tissue magnetization as a function of time for an arbitrary magnetic field,  $B_z(t)$ . The estimated size of parameter space is upwards of  $10^{12}$ , of which hundreds of thousands of sequences could be calculated and evaluated (Section 3.2.1.3). Therefore, the objectives of the simulations were speed and accuracy. It was sufficient to only consider the longitudinal magnetization, which was done by solving Equation (3.3) numerically.

The derivation and implementation of Equation (3.3), and numerical analysis of other candidate methods for calculating longitudinal magnetization are shown in the Appendices. It was necessary in select cases to have a method to calculate transverse

magnetization, (see the Appendices for derivation, implementation, and analysis), but in general this was not essential to the objectives.

### 3.1.1 DreMR Theory

A simplified review of signal intensity in a dreMR subtraction sequence is summarized below<sup>1</sup>, refer to Section 1.6.2 for a description of this technique. For a sequence that begins with a saturation RF pulse followed by a field-cycled polarization period (ignoring ramp times), the longitudinal magnetization is given as Equation (3.5), where  $M_z(t_0) = 0$ . This is equivalent to

$$M_{z\pm}(t) = M_0 \left( \frac{B_0 \pm \Delta B}{B_0} \right) \cdot (1 - e^{-R_{1\pm}t}). \quad (3.6)$$

To account for the increase in signal due to equilibrium magnetization, the signals must be multiplied by a normalization factor,

$$nF_{a,\pm} = \left( \frac{B_0}{B_0 \pm \Delta B} \right), \quad (3.7)$$

referred to as the analytical normalization factor. This factor works well under the conditions of small ramp times and small field shifts such that the relaxation rate of the tissue has linear slope. This method to normalize tissue magnetization was first proposed by Alford et al.<sup>1</sup> and has since been used in several other dreMR studies<sup>16-22</sup>. After subtraction of the two field-cycled images, the SNR in the final dreMR image is given as

$$SNR_{dreMR} \propto 2 M_0 t \Delta B R_1' \sigma^{-1}, \quad (3.8)$$

where  $\sigma$  is the noise, and the slope of the relaxation rate,  $R'_1$ , is assumed to be linear across the range of field shifts,  $\Delta B$ . Contrary to Equation (3.8), there is not a linear dependence on time. In fact, if the polarization time is set too long, voxel magnetization saturation will lead to decreased SNR. However, the original assumptions behind this equation were such that the product of  $t \cdot (\Delta B R'_1)$  was small, to illustrate that there is linear dependence of SNR with field shift. For samples with strong dependence of relaxation on field strength, such as some targeted contrast agents in their bound state<sup>23</sup>, the SNR is maximized linearly with field shift amplitude and the slope of the relaxation dispersion. For non-dispersive tissues, after the normalization has equalized the influence of equilibrium magnetization, the signal is close to zero. Therefore, the dreMR image contains signal contributions only from dispersive tissues and suppresses signal from non-dispersive tissue.

However, Equation (3.8) and its associated assumptions may not apply at lower field strengths or with different dispersion curves. The analytical normalization factor loses accuracy with finite sequence ramp times and breaks down as negative field shift amplitude approaches the strength of the host scanner. An improvement on the above normalization method was suggested by Hoelscher et al.<sup>14</sup> which takes into account a post-shift wait time, but it still only applies in limiting situations (see Appendix B.3 for numerical analysis and evaluation).

## 3.2 Methods

### 3.2.1 General Simulation Approach

The following sections give an overview of the tissue magnetization model and simulation approach. Then a visual summary is shown in a flow chart.

### 3.2.1.1 Nuclear Magnetic Resonance Dispersion

A prerequisite for simulation of  $T_1$  dispersion based contrast is knowledge of the nuclear magnetic resonance dispersion (NMRD) profiles of the tissues of interest. This can be obtained experimentally<sup>24</sup> or from the literature<sup>19,25,26</sup>. For this project, the relaxation dispersion of gadolinium-based contrast agent, Ablavar, was used to demonstrate how contrast can be optimized between dispersive and non-dispersive tissue. Ablavar is a blood pool contrast agent that exhibits strong  $T_1$  field dependence when bound to its target molecule serum albumin, and relatively little field dependence in its unbound state<sup>27,28</sup>. The use of Ablavar was not of particular interest in this specific agent, but rather due to availability of relaxivity data, which were obtained from the lab of Dr. Timothy Scholl at Western University<sup>18,19</sup>. Figure 3.1 shows the relaxation rates of several tissues highlighted in the proceeding sections: Ablavar bound to rabbit serum albumin (RSA); Ablavar in its unbound state; RSA; and phosphate buffer saline (PBS), into which the previously listed samples were dissolved.

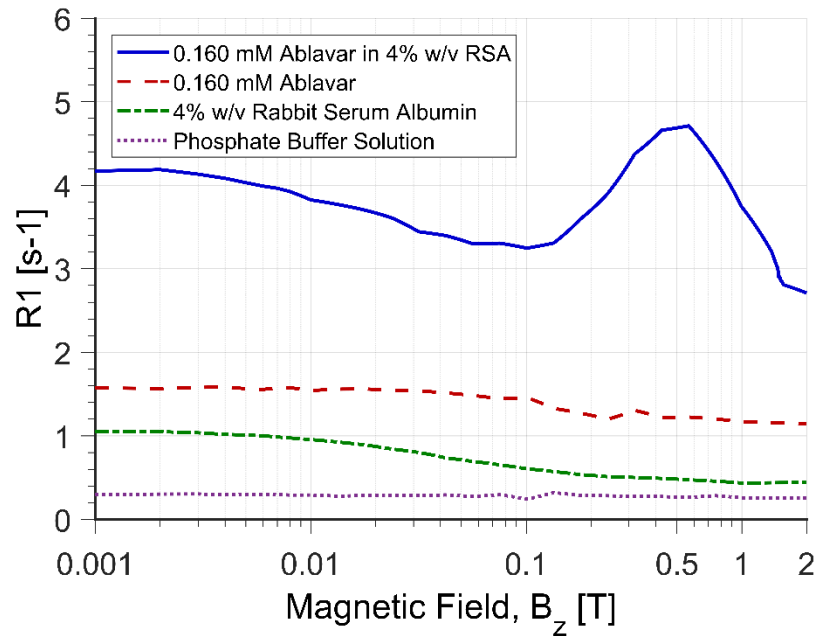


**Figure 3.1:** Relaxation dispersion profiles of Ablavar in the bound and unbound state, rabbit serum albumin, and a buffer solution.

### 3.2.1.2 Define Tissues

The next step is to define samples of interest with a simulated phantom. In general, this could include many voxels of different tissues with various molecular concentrations or partial volumes. It was sufficient for this project to model tissues as individual voxels of isochromatic spin. Relaxivity was determined by subtracting the relaxation rate of the buffer solution from the observed  $R_1$  and dividing by concentration, as shown in Equation (1.8). Relaxivities were scaled linearly by concentration<sup>29</sup>, and relaxation rates were combined to define the dispersion profiles. For the simulations, it was assumed that the binding fraction of the agent to the target molecule was independent of concentration, even though this is not true in general<sup>27</sup>. The equilibrium magnetization was calculated from the Curie equation, shown in Equation (1.1). For all tissues, it was assumed that the proton density was unity.

### 3.2.1.3 Define and Traverse Sequence Space

The polarizing field is a trapezoidal waveform characterized by six parameters. These parameters are:  $b_{Delta}$ , the field shift amplitude;  $t_{Pause}$ , a pre-shift wait time;  $t_{Rise}$ , the ramp-up time;  $t_{Flat}$ , the time spent at  $B_0 \pm \Delta B$ ;  $t_{Down}$ , the ramp-down time; and  $t_{Wait}$ , a post-shift wait time. This is shown in Figure 3.2. Constraints can be placed on these parameters based on hardware or application demands, such as minimum ramp time or a fixed post-shift wait time (which is often required to allow the field to stabilize before detection). For the simulations, sequences were discretized by one millisecond time intervals and one millitesla field shifts. As it is typical for dreMR sequences to begin with a saturation radiofrequency pulse, the initial magnetization of all tissues for all sequences was set to zero.

For small number of parameters, exhaustive grid searches are the simplest implementation of a search algorithm. However, as the size of parameter space increases, brute force methods soon become infeasible. A simulated annealing search algorithm was written in MATLAB (MathWorks, R2017a) to find the polarizing time course which optimized contrast between a set of tissues. The simulations were conducted in a tiered approach of gradually increased number of parameters. The first tier held the ramp and wait times fixed at 0.001 s, while varying field shift amplitude and total time. The second tier added independently variable ramp times. The third tier used all six parameters. Because of the probabilistic nature of simulated annealing, it is possible that the outputted solution is not the precise global optimum. Using a tiered approach lends confidence to the outputted sequences, since it can be verified that the results improve (or remain equal) as the number of parameters increase.

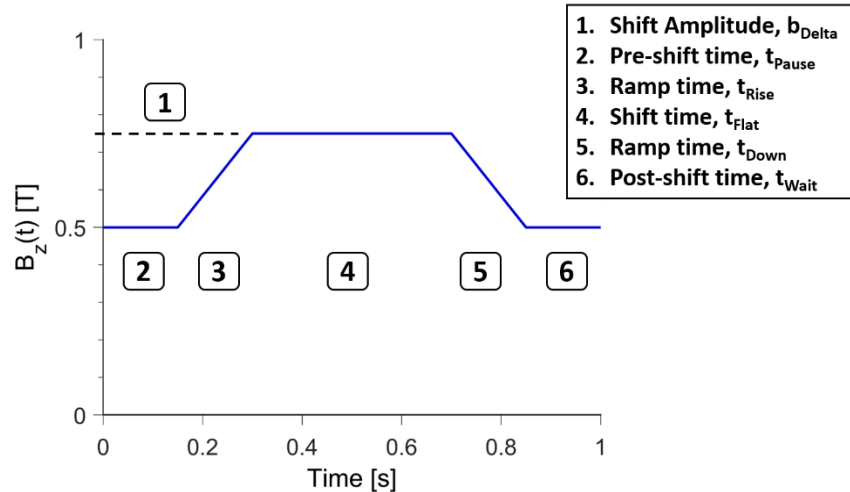


**Figure 3.2:** Example field-shift sequence showing the six parameters by which it is characterized.

### 3.2.1.4 Calculate Magnetization and Signal

The absolute magnetization,  $M_z(t)$ , is numerically calculated for the time-varying magnetic field at the specified sampling rate or tolerance (depending on whether a fixed-step or adaptive-step method is used) and interpolated back onto the original time step. At the end of the polarizing sequence, the magnetization can be run through an imaging module to determine the final MR signal intensity. This includes positional dependence of the voxel, radiofrequency coil homogeneity, acquisition parameters of the applied imaging sequence, and  $T_2$  effects. For the purposes of this work, the signal intensity was considered to be equal to the longitudinal magnetization at the instant before image acquisition. The noise floor was set to an arbitrarily low value, equal to roughly 1% of the tissue equilibrium magnetization. It was assumed that noise was dependent only on the detection field,  $B_0$ , and scaled linearly with it. After calculation, signal intensities and noise were then normalized as applicable to the imaging technique. The method to normalize signals is described in Section 3.2.4.

### 3.2.1.5 Evaluation the Solution

There are several ways to evaluate a sequence. The following examples are related to dreMR subtraction. The SNR in the final dreMR image for a particular voxel is the absolute value of the subtraction of weighted signal intensities,  $S$ , from the positive and negative image, relative to the noise in the final image,  $\sigma_d$ . The CNR is a measure of tissue differentiation and is the subtraction of the SNR for the involved tissues. The tissue-suppression-ratio (TSR) is a measure of the suppression of a tissue, given as the ratio of their signals.

$$SNR_j = \left(\frac{1}{\sigma_d}\right) \cdot |S_{j,pos} - S_{j,neg}| \quad (3.9)$$

$$\sigma_d = \sqrt{\sigma_{pos}^2 + \sigma_{neg}^2} \quad (3.10)$$

$$CNR_{ij} = SNR_i - SNR_j \quad (3.11)$$

$$TSR_{ij} = \left|\frac{S_i}{S_j}\right| \quad (3.12)$$

The primary metric for evaluation of dreMR sequences is the CNR. However, the algorithm could use any cost function to guide its search including weighted combinations of the above metrics. Constraints can also be used to efficiently guide the simulations, such as setting a minimum signal intensity,  $|S_i| \geq S_{min}$ , or specifying the SNR of a tissue to be close to the noise floor,  $SNR_j = 1 \pm \varepsilon$ . After sequence evaluation, the algorithm iterates over parameter space until it converges on a set of optimal parameters. A flowchart of the simulation method is shown in Figure 3.3.

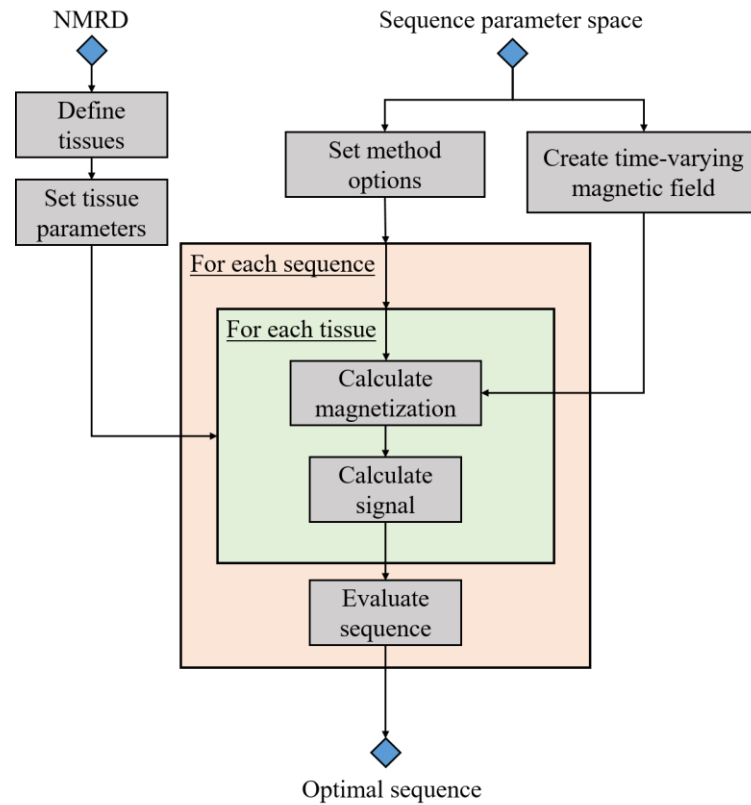


**Figure 3.3:** Flowchart of the general simulation approach.

### 3.2.2 Verification of the Model

Validation of the methods to solve the time-varying Bloch equations were done via numerical analysis and comparison to analytical solutions when applicable (see Appendix B). To verify that the method could be used to accurately predict contrast between tissues, simulations were compared to in-vitro imaging experiments.

Magnitude image data were obtained from Dr. Timothy Scholl of Western University of positive and negative field-shifted in-vitro images taken on a 1.5 T GE Signa scanner (University Hospital, Western University, Canada), using a fast spin-echo sequence and an auxiliary insert coil<sup>17,18</sup>. The two samples were vials of: (A) 0.250 mM Ablavar bound to 0.400 mM RSA, and (B) 0.400 mM RSA. Both were dissolved in PBS

with a pH of 7.4. The following parameters were applied during magnetization preparation: the saturation radiofrequency pulse width was 1 ms, the initial wait time was 10 ms, the field shift amplitude was 224.46 mT in each direction about 1.5 T, the ramp up and ramp down times were both 10 ms, with a 280 ms flat top time for one image set and 580 ms for another (see Figure 3.4). The repetition time was long enough that the amount of transverse magnetization remaining was negligible (no magnetization flipped back into longitudinal axis). Images were acquired with samples at a temperature of 37°C.

Representative images from each set were processed to extract signal intensity. The imaged tissues were modeled and the magnetizations were calculated and scaled, so that direct comparisons with the images could be drawn.

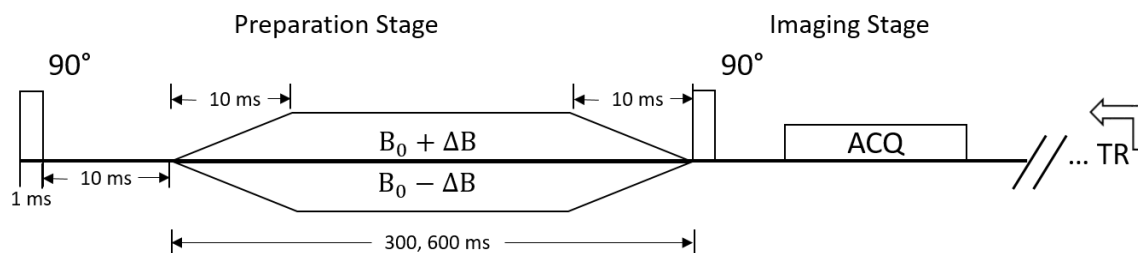


**Figure 3.4:** Schematic of the magnetization preparation sequences used to acquire field-cycled  $T_1$ -weighted images.

### 3.2.3 Field-cycled $T_1$ -Weighted Image Optimization

The objective of the first simulation experiment was to determine how to use  $T_1$  field dependence to maximize  $T_1$ -weighted image contrast between dispersive and non-dispersive tissue. The two tissues of interest were bound contrast agent (see Figure 3.1 for  $R_1$  dispersion profile), and an idealized non-dispersive tissue with a  $T_1$  of 3500 ms. For a magnetization preparation sequence that begins with a  $90^\circ$  RF saturation pulse and

continues with a field-cycled polarization pulse (neglecting ramp time), the equation for longitudinal magnetization is Equation (3.6). The contrast between a dispersive tissue,  $d$ , and a non-dispersive tissue,  $f$ , is

$$C_{df} = M_0 \left( \frac{B_0 \pm \Delta B}{B_0} \right) \cdot \left| e^{-R_1^f t} - e^{-R_{1\pm}^d t} \right|. \quad (3.13)$$

If the magnetic field is constant during a preparation sequence,  $B_z(t) = B_0$ , then the maximum contrast with respect to time is found by setting the partial derivative to zero and solving for time.

$$\frac{\partial(C_{df})}{\partial t} = 0 = M_0 \left[ R_1^d \cdot e^{-R_1^d t} - R_1^f \cdot e^{-R_1^f t} \right] \quad (3.14)$$

$$t_{max} = \frac{1}{(R_1^d - R_1^f)} \cdot \ln \left( \frac{R_1^d}{R_1^f} \right) \quad (3.15)$$

Equation (3.15) is the same expression found when optimizing for  $T_1$  contrast in a spin-echo or inversion recovery sequence<sup>30</sup>. However, the solution for which maximum CNR is found with respect to an arbitrary magnetic field is not straightforward because of the nonlinear dependence of  $R_1$  on  $B_z$ . The simulated annealing algorithm was used to find the polarizing field time-course that would maximize the CNR, using the tiered approach described in Section 3.2.1.3. The maximum field shift and time were limited to 0.5 T and 1 s. The detection field strength was 0.5 T.

### 3.2.4 Improvement to Normalization

In a dreMR subtraction sequence, the individual images must be normalized to account for the change in equilibrium magnetization caused by field cycling. This enables

suppression of non-dispersive tissues. Previous treatment of image normalization used analytical expressions that work only in limited cases of magnetization preparation sequences. The method to achieve proper tissue normalization for an arbitrary sequence requires a numerical treatment. The normalization factor is calculated on a tissue with a relatively non-dispersive  $R_1$  profile. The denominator is the value of the magnetization of that tissue at the end of the given field-cycled sequence. The numerator is the magnetization that tissue would achieve over the same time interval, given no field offset. This factor is then applied to the entire image, such that all signal intensities and noise are multiplied by the same value. The normalization factor for a tissue,  $f$ , with a relatively flat dispersion profile is

$$nF_{f,\pm} = \frac{M_{z,off}^f(t_{final})}{M_{z,on}^f(t_{final})}. \quad (3.16)$$

For a preparation sequence with constant offset field of  $B_0 \pm \Delta B$  with infinitesimal ramp time, the expression simplifies to the analytical normalization factor, in Equation (3.7).

$$nF_{f,\pm} = \frac{M_0(1 - e^{-R_{1,f}t})}{M_{0,\pm}(1 - e^{-R_{1,f}t})} = \frac{M_0}{M_{0,\pm}} = nF_{a,\pm} \quad (3.17)$$

### 3.2.5 Optimization of DreMR Subtraction Method

The objective of the second simulation experiment was to determine how to maximize contrast between bound and unbound contrast agent, normalized to background tissue. The three samples are: (A) 0.160 mM of Ablavar bound to 0.606 mM RSA, (B) 0.160 mM unbound Ablavar, and (C) 0.606 mM RSA, all dissolved in a buffer solution

with an approximately constant  $T_1$  of 3.84 s. The relaxation rate dispersion profiles are shown in Figure 3.1.

The simulated annealing algorithm was used to find the optimal dreMR subtraction sequence at 0.5 T and 1.5 T to maximize contrast between tissues A and B, normalized to tissue C. In one search, a symmetry constraint was placed on the positive and negative sequences, such that all corresponding parameters were identical to each other. This is a four-parameter search space: amplitude, wait time, rise time, and total time. Then to show the optimal sequence, another search was done in which all twelve parameters (six each for the positive and negative shift sequences) were allowed to independently vary. The global constraints on the algorithm were: maximum field shift amplitude,  $|\Delta B_{max}| \leq 0.5$  T, (0.499 in the case of negative shifts at 0.5 T detection field); total time for a shift,  $t_{shift} \leq 1$  s; and to ensure tissue suppression,  $SNR_C \leq 1$ .

### 3.3 Results

#### 3.3.1 Verification of the Model

Images were processed using 3D Slicer software by Colin McCurdy. Voxel intensity and standard deviation of intensity for each vial were calculated by creating a region of interest (ROI) of 56 pixels around the center point. This size was chosen to avoid partial volumes around edge pixels, and to only contain the volumes within the vials. The background noise was determined with an ROI of 3595 pixels in an empty region of space. Figure 3.5 shows the magnitude images for the 300 ms shift sequence, (a) positive shift, (b) negative shift, and the 600 ms shift sequence, (c) positive, (d) negative. The signal

intensity for the bound agent is significantly higher than the vial containing only albumin. Furthermore, the 600 ms sequence has higher intensities than the other image set.

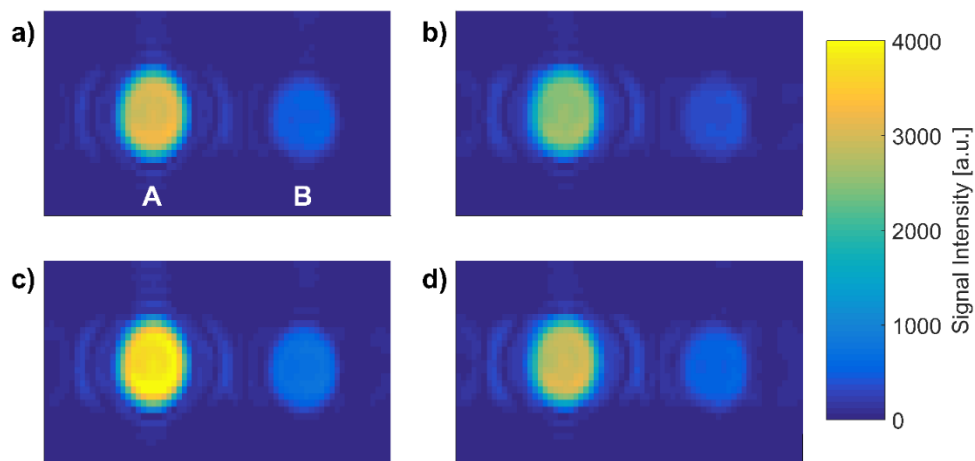


**Figure 3.5:** Phantom image, obtained using field-cycling and a fast spin-echo sequence at 1.5 T. (a) Positive field shift image of amplitude 224.46 mT with shift time of 300 ms; A: Ablavar 0.250 mM and RSA 0.400 mM, B: RSA 0.400 mM. (b) Negative field shift image of same tissues for same shift amplitude and time. (c) Positive field shift image with shift time of 600 ms. (d) Negative field shift image with shift time of 600 ms.

**Table 3.1:** Mean signal intensity and standard deviation for the image set with 300 ms field shift; see Figure 3.5 (a) and (b).

Tissue	Intensity <sup>a</sup>	SD	Simulation <sup>b</sup>
Positive Image			
A <sup>c</sup>	3104.2	109.5	3106.1
B <sup>d</sup>	482.6	38.6	482.6 <sup>b</sup>
Background	12.3	3.5	-
Negative Image			
A <sup>c</sup>	2567.6	86.7	2548.7
B <sup>d</sup>	359.1	32.7	362.5
Background	13.2	3.6	-

<sup>a</sup> Arbitrary units

<sup>b</sup> After scaling by a factor to match Tissue B, pos

<sup>c</sup> Ablavar 0.250 mM and RSA 0.400 mM

<sup>d</sup> RSA 0.400 mM

The signal intensities and standard deviations for Figure 3.5 (a) and (b) are given in Table 3.1. The magnetization of the modeled tissues was calculated for the preparation stage by solving Equation (3.3). In order to make direct comparisons, a single scaling factor was determined from the ratio of the simulated intensity of tissue B, in the positive image of image set one, to the mean intensity of tissue B in Figure 3.5a. This scaling factor was then applied to all tissues for all images (both positive and negative). The simulated intensities are shown in Table 3.1. Error in the scaling factor was derived from the standard error of the mean intensity of tissue B. For this reason, both the image and simulation intensity of tissue B have the exact same value (whereas the others are close, but not exact).

The simulations were evaluated by comparing the values of  $CNR_{AB}$  and  $TSR_{AB}$ , shown in Table 3.2. For the processed images, the uncertainty in the values comes from the standard error in image intensity, and conventional error propagation. For the simulations, the uncertainty in CNR comes from the error of the scaling factor and noise.

The uncertainty in TSR is derived from the absolute error of tissue intensity after scaling. For this reason, and because of the vial chosen for scaling, the  $\text{TSR}_{\text{pos}}$  in image set one is very small. This also accounts for the relatively larger TSR uncertainty for the second image set, since the true factor to scale the simulations is unknown. Note that scaling was only necessary to make direct comparisons to in vitro images, but is not used in general to compare against other simulations. These simulations show excellent agreement with the field-cycled images. This demonstrates that the method to model magnetization could be used to predict magnetization as a function of time for an arbitrary magnetic field, and therefore could be used to optimize  $T_1$ -weighted pulse sequences through evaluation of the generated contrast.

**Table 3.2:** Evaluation of image sets and simulations via contrast-to-noise ratio and tissue-suppression-ratio. Image set 1 had a field shift of 300 ms. Image set 2 had a field shift of 600 ms. Uncertainty in contrast-to-noise for simulations was derived from the error in the scaling factor and the noise. TSR uncertainty was derived from the absolute error of tissue intensity after scaling. Since the scaling factor was determined from Image Set 1, the simulation uncertainty in TSR for this set are small.

	Images	Simulations
Image Set 1		
CNR <sub>pos</sub>	$213 \pm 2$	$214 \pm 3$
CNR <sub>neg</sub>	$168 \pm 1$	$166 \pm 2$
TSR <sub>pos</sub>	$6.43 \pm 0.08$	$6.436 \pm 0.004$
TSR <sub>neg</sub>	$7.15 \pm 0.09$	$7.03 \pm 0.08$
Image Set 2		
CNR <sub>pos</sub>	$218 \pm 2$	$214 \pm 2$
CNR <sub>neg</sub>	$158 \pm 1$	$156 \pm 2$
TSR <sub>pos</sub>	$5.35 \pm 0.05$	$4.4 \pm 0.9$
TSR <sub>neg</sub>	$5.57 \pm 0.06$	$4.6 \pm 0.9$

### 3.3.2 Field-cycled T<sub>1</sub>-weighted Image Optimization

Figure 3.6 shows the sequences that maximize contrast between a highly-dispersive and non-dispersive tissue, under various constraints. The sequence parameters and evaluation are given in Table 3.3. In the case where the magnetic field is held constant at 0.5 T (Figure 3.6a), the optimal polarization time was 0.636 s and the CNR was 72.05 (in arbitrary units). This time was verified analytically using Equation (3.15). Figure 3.6b is the result of allowing shift amplitude to vary, with minimal values for the other parameters. The outcome of the search algorithm was a sequence with a field shift equal to the upper limit for a length of time of 0.744 s, again equal to the analytically determined time. The

CNR in this case was 136.82; a 90% increase. The CNR when allowing all six parameters to vary (Figure 3.6c) was only slightly larger, at 137.19. Since the effective offset field was lower the non-dispersive tissue did not magnetize as high, even though the sequence was slightly longer, whereas the magnetization of the bound agent was the same. This was because the slow rise time meant temporarily faster recovery, since the  $R_1$  is lower at 1.0 T than it is at 0.5 T. The increase in CNR is not significant, but indicates that fast ramp times are not always necessary. The final sequence (Figure 3.6d) yields the most contrast in consideration of signal averaging. The CNR for the individual sequence is 107.69, but when normalized by the square root of the total time it becomes 197.94. However, this does not include the time for image acquisition. This concept of normalizing for sequence time will not be considered further. The values for CNR cannot be directly compared with Section 3.3.1 due to differing values of noise, and in general should only be compared relatively to other values of CNR and SNR.

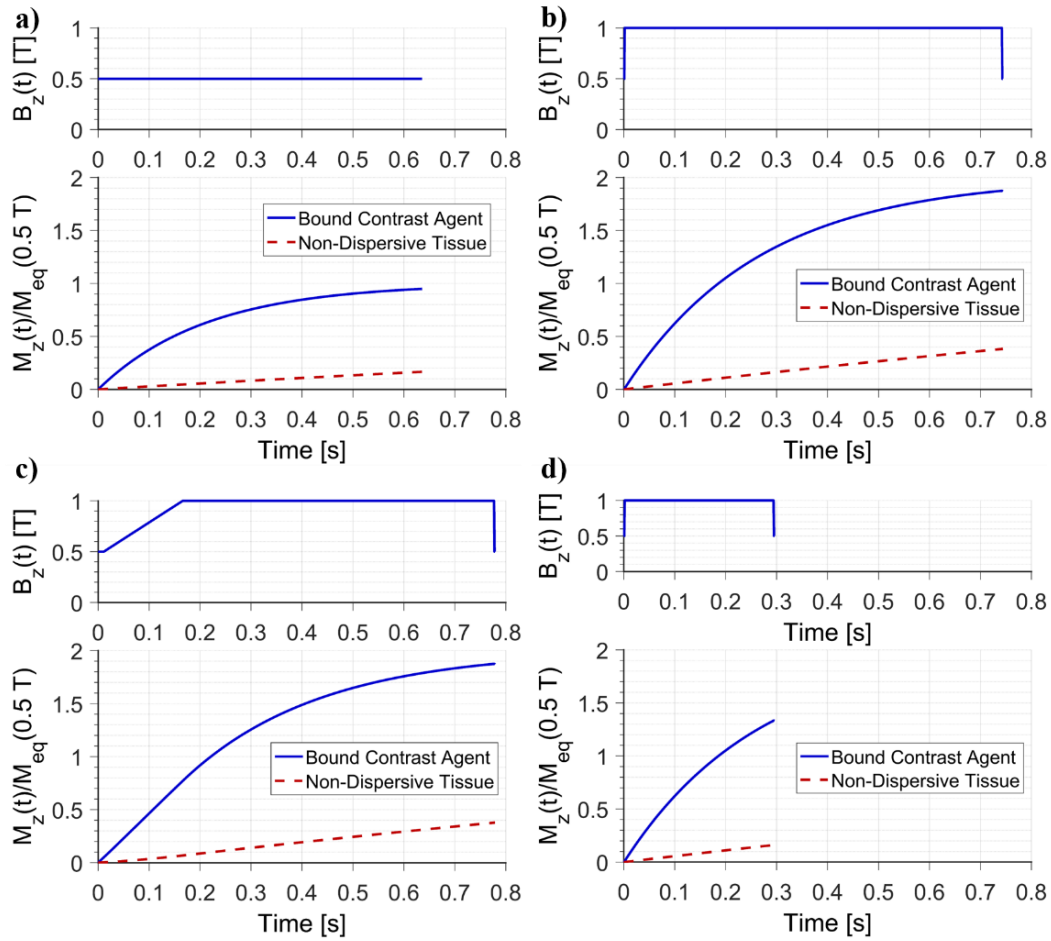


**Figure 3.6:** Simulations showing how the magnetizations of the bound agent (highly dispersive) and the flat tissue develop in time-dependent polarizing fields. In (a), the 0.636 s long waveform at the fixed detection field of 0.5 T is the analytically determined optimal time to polarize these tissues. (b) is the result of allowing the field shift amplitude to vary, but with fixed, minimal ramps and wait times. In (c), all six trapezoid parameters were varied to produce maximum contrast. (d) represents the optimal polarizing field in consideration of signal averaging. The magnetization values are normalized with the equilibrium magnetization at 0.5 T.

**Table 3.3:** Contrast-to-noise ratio and sequence parameters for the sequences shown in Figure 3.6. The noise value was approximately 1.09% of the equilibrium magnetization at 0.5 T.

Sequence	CNR <sup>1</sup>	$\Delta B$ [T]	$t_{\text{pause}}$ [s]	$t_{\text{rise}}$ [s]	$t_{\text{flat}}$ [s]	$t_{\text{down}}$ [s]	$t_{\text{wait}}$ [s]
a	72.05	0'	0'	0'	0.636	0'	0'
b	136.82	0.5	0.001'	0.001'	0.740	0.001'	0.001'
c	137.19	0.5	0.011	0.155	0.611	0.001	0.001
d	197.94"	0.5	0.001	0.001	0.292	0.001	0.001

<sup>1</sup> Arbitrary units

' denotes parameter was fixed for simulation

" CNR is normalized by square root of total shift time. Normal CNR is 107.69.

### 3.3.3 Improvement to Normalization

For the dreMR subtraction sequences to follow, the magnetizations were normalized with respect to serum albumin, representative of unenhanced biological tissue. For two of the sequences shown in Section 3.3.4, the normalization factors using the numerical and analytical methods are shown in Table 3.4. The numerical method multiplies the tissue magnetization by whatever factor is necessary to equal the value of magnetization that occurs when the tissue is exposed to the detection field for the same length of time as the field shift sequence. This results in a relative percent error of zero. Note that complete tissue suppression will only occur when the positive and negative sequences are applied for the same amount of time. The analytical method multiplies the magnetization by a factor determined from the peak shift amplitude. For sequences at 1.5 T, the errors are relatively small. However, the method fails for many sequences at 0.5 T with large negative field shifts, because of division by near-zero.

**Table 3.4:** Normalization factors for the numerical and analytical method. The sequences are described in Section 3.3.4. Also shown are the relative percent errors of the normalized tissue magnetization compared to the magnetization as if it were polarized for the same length of time with no offset field.

Sequence	Normalization Factor		Relative Error [%]	
	Numerical <sup>1</sup>	Analytical <sup>2</sup>	Numerical	Analytical
1.5 T b) <sup>3</sup>				
Positive	0.83479	0.75075	0	10
Negative	1.2909	1.5	0	16
0.5 T b) <sup>3</sup>				
Positive	0.67434	0.5	0	26
Negative	2.5322	500	0	19628

<sup>1</sup> Using tissue C, the non-dispersive serum albumin.

<sup>2</sup> Using Equation (3.7) .

<sup>3</sup> See Figure 3.7b and Figure 3.8b, respectively.

### 3.3.4 Optimization of DreMR Subtraction Method

Figure 3.7 shows the optimal symmetrical (a) and non-symmetrical (b) dreMR subtraction sequences at 1.5 T. In accordance with the literature, the sequences prefer the maximum allowed field shifts<sup>1</sup>. The sequence parameters and evaluations are given in Table 3.5 and Table 3.6, respectively. Interestingly, sequence (a) is very similar to one of the sequences in the image sets analyzed in Section 3.3.1. However, the results should not be quantitatively compared because of different tissue concentrations and values for noise. Sequence (b) is longer and has long ramp down times, but yields a 60% increase in CNR between the bound and unbound agent. For both sequences, the background tissue has signal intensity below the noise floor, as this was a specified constraint for the search.

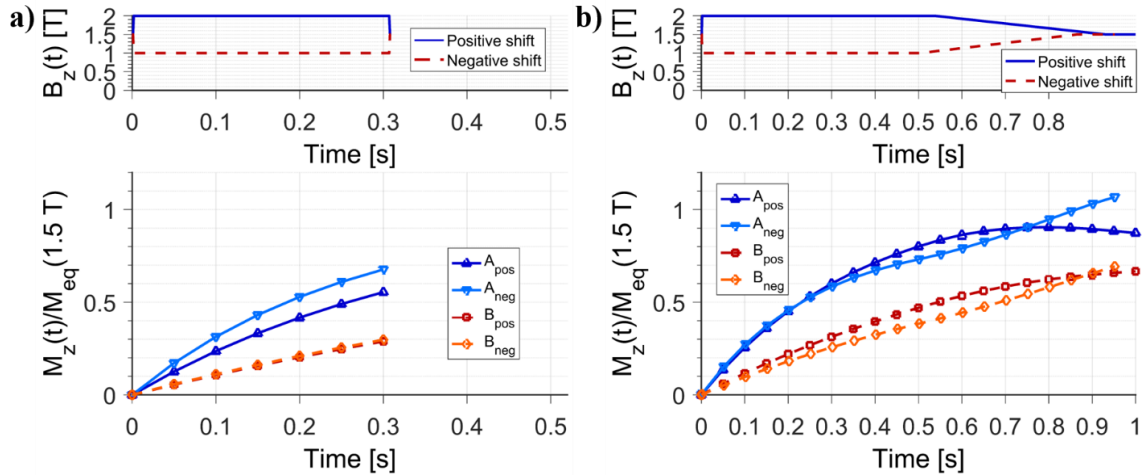


**Figure 3.7:** Simulations showing the optimal dreMR subtraction sequences about 1.5 T to maximize contrast between tissue A, bound contrast agent, and B, unbound agent, normalized with respect to tissue C, serum albumin (not shown). In (a), the two trapezoids are constrained to be symmetrical in shape and to each other. In (b), the only constraints were maximal field shift and length of 0.5 T and 1 s. The magnetization values are normalized with the equilibrium magnetization at 1.5 T.

**Table 3.5:** Sequence parameters for the sequences shown in Figure 3.7.

Sequence	$\Delta B$ [T]	$t_{\text{pause}}$ [s]	$t_{\text{rise}}$ [s]	$t_{\text{flat}}$ [s]	$t_{\text{down}}$ [s]	$t_{\text{wait}}$ [s]
$a_{\text{pos}}^1$	0.5	0.001	0.001	0.305	0.001	0.001
$a_{\text{neg}}^1$	0.5	0.001	0.001	0.305	0.001	0.001
$b_{\text{pos}}$	0.5	0.001	0.001	0.536	0.393	0.069
$b_{\text{neg}}$	0.5	0.001	0.001	0.502	0.361	0.087

<sup>1</sup> No fixed parameters, but a symmetry constraint for trapezoids.

**Table 3.6:** Noise, SNR, and CNR for the sequences shown in Figure 3.7. The noise in the individual images before normalization was 1.09% of the equilibrium magnetization at 1.5T.

Sequence	Noise <sup>1</sup>	SNR <sub>A</sub>	SNR <sub>B</sub>	SNR <sub>C</sub>	CNR <sub>B</sub>	CNR <sub>C</sub>
a	1.83	6.86	0.55	1.E-15	6.32	6.86
b	1.66	11.65	1.58	0.83	10.07	10.82

<sup>1</sup> Noise in the dreMR image, as a percentage of  $M_0$ .

Figure 3.8 shows the optimal symmetrical (a) and non-symmetrical (b) dreMR subtraction sequences at 0.5 T. The sequence parameters and evaluations are given in Table 3.7 and Table 3.8, respectively. Simulated phantom images for these sequences are shown in Figure 3.9 and Figure 3.10. Unlike the symmetrical sequence at 1.5 T, Figure 3.8a shows long ramp times, and gives a CNR of 16.62 between the bound and unbound agent. The long ramp times are necessary for the negative shift sequence. This is because if short ramp times were used, the tissues would not gather any magnetization. This would effectively be the same as a single field-cycled  $T_1$ -weighted image (Section 3.3.2), but would fail the suppression requirements. When a search was conducted for the optimal symmetrical sequence with minimal ramp times (not shown, but looks very similar to Figure 3.7a), the field shifts were  $\pm 0.376$  T for 0.368 s for the individual positive and negative sequences, and the CNR was 4.82. The advantage of being able to have long ramp times is that the coil can support higher values of inductance, which correlates to achieving higher field shifts. The sequence shown in Figure 3.8b is the result of allowing all twelve sequence parameters to vary in the search algorithm. The CNR is 37.73, a 127% increase from the symmetrical sequence. This value is significantly higher than the optimal sequence at 1.5 T, even when adjusting for differences in noise.

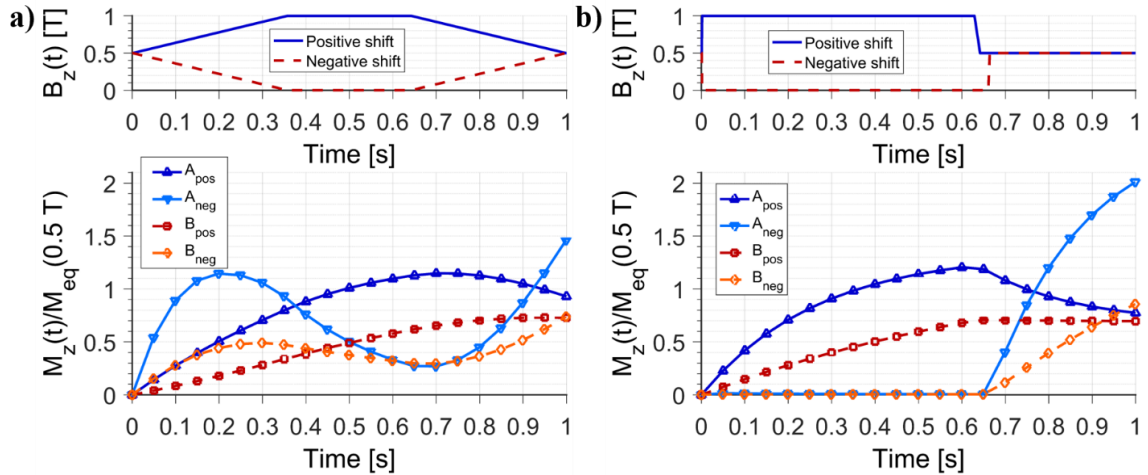


**Figure 3.8:** Simulations showing the optimal dreMR subtraction sequences about 0.5 T to maximize contrast between tissue A, bound contrast agent, and B, unbound agent, normalized with respect to tissue C, serum albumin (not shown). In (a), the two trapezoids are constrained to be symmetrical in shape and to each other. In (b), only the global constraints applied. The magnetization values are normalized with the equilibrium magnetization at 0.5 T.

**Table 3.7:** Sequence parameters for the sequences shown in Figure 3.8.

Sequence	$\Delta B$ [T]	$t_{\text{pause}}$ [s]	$t_{\text{rise}}$ [s]	$t_{\text{flat}}$ [s]	$t_{\text{down}}$ [s]	$t_{\text{wait}}$ [s]
$a_{\text{pos}}^1$	0.499	0.001	0.356	0.286	0.356	0.001
$a_{\text{neg}}^1$	0.499	0.001	0.356	0.286	0.356	0.001
$b_{\text{pos}}$	0.5	0.001	0.001	0.627	0.013	0.358
$b_{\text{neg}}$	0.499	0.001	0.001	0.659	0.003	0.335

<sup>1</sup> No fixed parameters, but a symmetry constraint for trapezoids.

**Table 3.8:** Noise, SNR, and CNR for the sequences shown in Figure 3.8. The noise in the individual images before normalization was 1.09% of the equilibrium magnetization at 0.5T.

Sequence	Noise <sup>1</sup>	$\text{SNR}_A$	$\text{SNR}_B$	$\text{SNR}_C$	$\text{CNR}_B$	$\text{CNR}_C$
a	3.15	17.02	0.40	1.E-15	16.62	17.02
b	2.85	43.40	5.57	0.01	37.73	43.39

<sup>1</sup> Noise in the dreMR image, as a percentage of  $M_0$ .

The simulated phantom images are a useful aid to visualize the results of Table 3.8. Voxel intensity is shown with respect to the noise floor for the positive, negative, and dreMR images of the two sequences showcased at 0.5 T. The values are scaled such that the maximum signal (sequence b, tissue A) is set to unity. There is a reduced SNR in the dreMR image, but increased tissue differentiation.

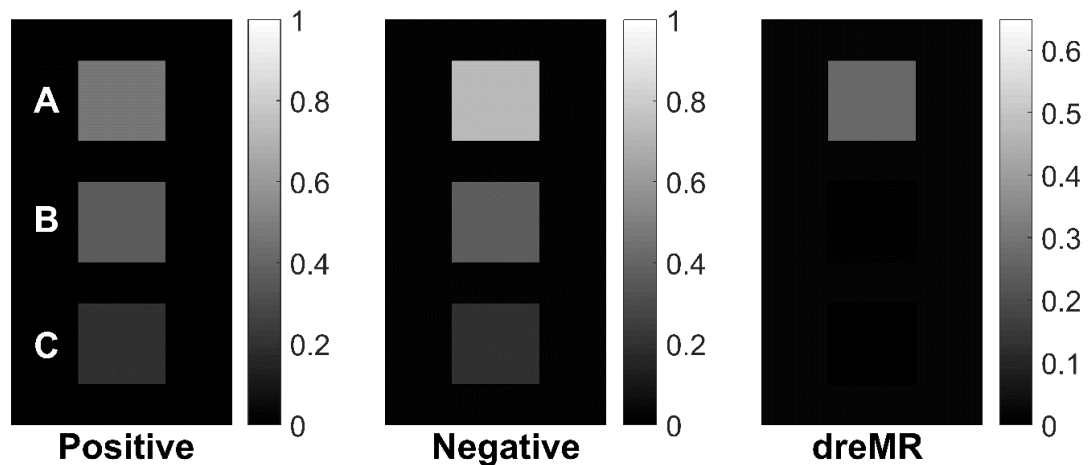


**Figure 3.9:** Simulated phantom images for the sequences shown in Figure 3.8a: the normalized, field-cycled,  $T_1$ -weighted positive and negative shift images, and the dreMR image showing the absolute difference. A: bound contrast agent; B: unbound agent; C: serum albumin. Signal intensity has been normalized with respect to tissue C. The dreMR image has reduced SNR but increased contrast of sample A.

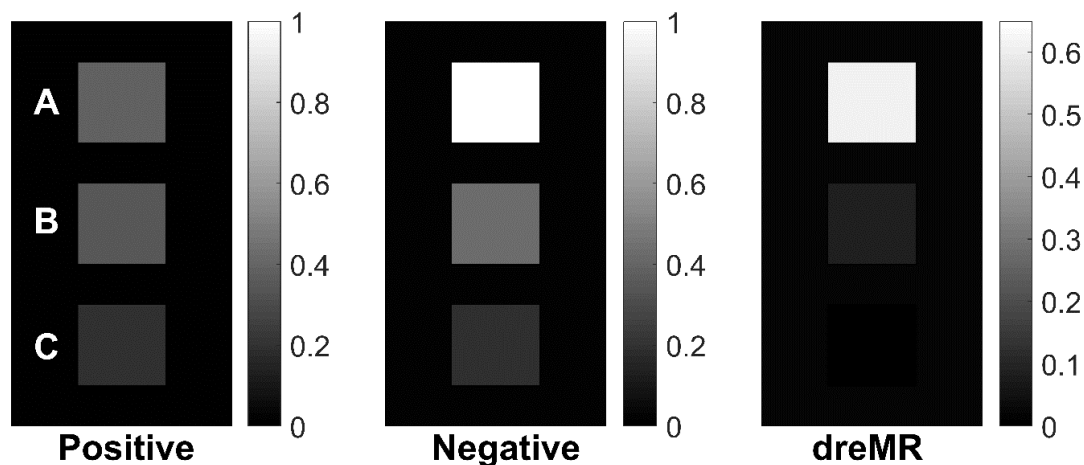


**Figure 3.10:** Simulated phantom images for the sequences shown in Figure 3.8b: the normalized, field-cycled,  $T_1$ -weighted positive and negative shift images, and the dreMR image showing the absolute difference. A: bound contrast agent; B: unbound agent; C: serum albumin. Signal intensity has been normalized with respect to tissue C. The dreMR image has even greater contrast with this sequence than the symmetrical sequence (Figure 3.9).

### 3.4 Discussion

This chapter explored a tool that was developed to model tissue magnetization as a function of time for an arbitrary polarizing magnetic field. In combination with a simulated annealing search algorithm, candidate pulse sequences were evaluated based on the contrast generated between tissues with and without relaxation dependence on magnetic field strength. The only requirement for the model were NMRD data for the tissues, although partial, or even simulated, data could still be used to get approximate results. For generalization to other tissues, or other types of sequences, it may be necessary to acquire information on the spin density,  $T_2$  relaxation, and other tissue properties. Magnetization was calculated via numerical integration of the Bloch equations using methods that were

both fast and numerically accurate. Overall, the model was validated through comparison with in-vitro field-cycled  $T_1$ -weighted images. The excellent quantitative agreement between the simulated and experimental signal intensities indicates that the model can predict relative tissue magnetization with precision. However, more steps are required before the model can be used to make quantifiable predictions. This includes expansion of the model to include an image acquisition module, as well as more imaging experiments.

A study of  $T_1$ -weighted sequences was done to query the optimization of said images through field-cycling. It was shown that maximum contrast was achieved when the tissues were polarized at the highest field allowed, congruent with the work of Rinck et al<sup>31</sup>. This is understandable upon closer inspection of Equation (3.13). The magnetic field term increases monotonically, whereas the exponential terms are bound between zero and one, and vary proportional to the variation of  $R_1$  with field. For the tissues of interest, the variations were relatively small, thus the polarizing field strength was the dominating factor. This will not necessarily be the case between any two tissues. For example, Figure 3.11 shows the relaxation rates and contrast to noise as a function of magnetic field strength for bound Ablavar and fat. The contrast was determined using Equation (3.13), given the optimal times from Equation (3.15). The same value of noise was used as in Section 3.3.2. Negative values of CNR indicate that the signal from fat is higher than the agent. Interestingly, maximum contrast is not generated at the highest magnetic field strength, nor at the field where the  $R_1$  values are the most different (0.59 T). Within the range of fields shown, the optimal contrast occurs at a field strength of 0.868 T, however, the CNR is an order of magnitude smaller than the values shown in Table 3.3.

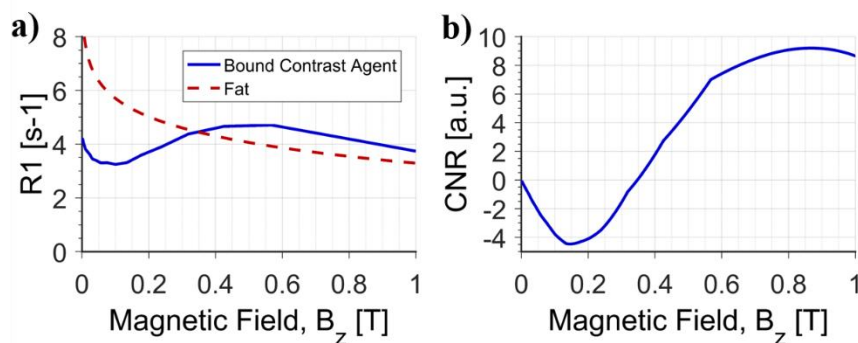


**Figure 3.11:** (a)  $R_1$  curves for bound agent and fat from 0 to 1 T. (b) Contrast to noise ratio as a function of magnetic field strength, calculated at optimal polarization time. Negative values indicate the fat tissue has higher signal intensity.

For implementation of dreMR subtraction sequences at 0.5 T, it was necessary to improve the method to normalize tissue magnetization to account for changes in equilibrium magnetization. It was shown that any given tissue could be exactly suppressed with this method. Best practice is to choose a tissue with  $T_1$  values that are representative of the background tissues across the polarization fields, which will vary by application. Signal normalization may be different in practice; therefore, experiments should be done to verify the method shown here. An example would be to collect field-cycled and conventional images of various tissues in-vitro, and check that when the field-cycled images are normalized, they match the conventional images.

The simulation tool was used to find the optimal dreMR subtraction sequences at two base field strengths. It was demonstrated that contrast can be greatly increased when not limited to symmetrical polarization sequences. The study focused on maximizing signal of a targeted contrast agent in its bound state, while suppressing the signals of the unbound state and of normal biological tissue. The use of contrast agents is not mandatory to realize

the benefits of field-cycling; it is only necessary to have tissues with sufficiently different relaxation dispersion curves. The formalism is general enough to allow any number of tissues to be included, however a more suitable cost function would be required for minimization in the simulated annealing algorithm.

The unexpected looking polarization sequence in Figure 3.8b reveals an underlying feature of the search algorithm. The reason the sequence has a large negative shift for such a long time has nothing to do with generating magnetization. It is to artificially boost the normalization factor. In fact, the same amount of contrast could be generated if the negative sequence was replaced with a constant polarizing field of 0.5 T for 0.335 s (essentially removing the first 664 ms of the already occurring sequence), then multiplying the signal intensities by 2.53 (Table 3.4), since the normalization factor would be unity otherwise. Ultimately, this indicates the ability of the algorithm to locate an optimal region of parameter space given the explicitly imposed and built-in constraints, however, there remains steps to be taken in order to translate the outcomes into practical imaging pulse sequences. The algorithm could be programmed to sense and make adjustments to inefficiencies in the polarization sequence. Sequences that are demanding of the hardware, or not suitable for the application, could be avoided through use of constraints on the search space, or by including appropriate terms in the minimization function of the algorithm. Improvements could be made on the set of parameters that characterize the polarization sequence. For example, a series of boxcar functions<sup>12</sup>, exponential curves, or even the inclusion of inversion RF pulses could be used. However, over-fitting of parameter space can lead to polarization sequences that are not practical, and could come at the expense of increased computational demand.

## 3.5 Conclusions

In this chapter, a procedure was presented to optimize  $T_1$  dispersion contrast. The results indicate the potential for enhanced tissue specificity at lower field strengths than clinical 1.5 T systems. The simulations were necessary to find novel polarization sequences for dreMR subtraction, as the proposed sequences were not straightforwardly derivative of previous theory. The results are integral to the optimal design of an auxiliary insert coil for dreMR imaging. Once a coil has been constructed, further steps are required to verify that the proposed sequences perform as expected, including in-vitro and in-vivo imaging experiments.

## 3.6 References

1. Alford JK, Rutt BK, Scholl TJ, Handler WB, Chronik BA. Delta relaxation enhanced mr: Improving activation - Specificity of molecular probes through R1 dispersion imaging. *Magn Reson Med.* 2009;61(4):796-802. doi:10.1002/mrm.21933.
2. Bloch F. Nuclear induction. *Phys Rev.* 1946;70(7-8):460-474. doi:10.1103/PhysRev.70.460.
3. Benoit-Cattin H, Collewet G, Belaroussi B, Saint-Jalmes H, Odet C. The SIMRI project: A versatile and interactive MRI simulator. *J Magn Reson.* 2005;173(1):97-115. doi:10.1016/j.jmr.2004.09.027.
4. Stöcker T, Vahedipour K, Pflugfelder D, Shah NJ. High-performance computing MRI simulations. *Magn Reson Med.* 2010;64(1):186-193. doi:10.1002/mrm.22406.
5. Haacke EM, Brown RW, Thompson MR, Venkatesan R. Magnetic resonance imaging: physical principles and sequence design. 1999. *New York A John Wiley Sons.* 1999.
6. Balac S, Chupin L. Fast approximate solution of Bloch equation for simulation of RF artifacts in Magnetic Resonance Imaging. *Math Comput Model.* 2008;48(11-12):1901-1913. doi:10.1016/j.mcm.2007.05.021.
7. Madhu PK, Kumar A. Direct Cartesian-Space Solutions of Generalized Bloch Equations in the Rotating Frame. *J Magn Reson Ser A.* 1995;114(2):201-211. doi:http://dx.doi.org/10.1006/jmra.1995.1127.
8. Murase K, Tanki N. Numerical solutions to the time-dependent Bloch equations

- revisited. *Magn Reson Imaging*. 2011;29(1):126-131. doi:10.1016/j.mri.2010.07.003.
9. Cordes C. Efficient Simulation of Magnetic Resonance Imaging. 2015.
  10. Hazra A. Numerical Simulation of Bloch Equations for Dynamic Magnetic Resonance Imaging. 2016.
  11. Lurie DJ, Aime S, Baroni S, et al. Fast field-cycling magnetic resonance imaging. *Comptes Rendus Phys*. 2010;11(2):136-148. doi:10.1016/j.crhy.2010.06.012.
  12. Nieminen JO, Voigt J, Hartwig S, et al. Improved Contrast in Ultra-Low-Field MRI with Time-Dependent Bipolar Prepolarizing Fields: Theory and NMR Demonstrations. *Metrol Meas Syst*. 2013;20(3):327-336.
  13. Hógáin DÓ, Davies GR, Baroni S, Aime S, Lurie DJ. The use of contrast agents with fast field-cycling magnetic resonance imaging. *Phys Med Biol*. 2011;56:105-115. doi:10.1088/0031-9155/56/1/007.
  14. Hoelscher UC, Lothar S, Fidler F, Blaimer M, Jakob P. Quantification and localization of contrast agents using delta relaxation enhanced magnetic resonance at 1.5 T. *Magn Reson Mater Physics, Biol Med*. 2012;25(3):223-231. doi:10.1007/s10334-011-0291-6.
  15. Broche LM, James Ross P, Pine KJ, Lurie DJ. Rapid multi-field T1 estimation algorithm for Fast Field-Cycling MRI. *J Magn Reson*. 2014;238:44-51. doi:10.1016/j.jmr.2013.10.010.
  16. Alford J, Sorensen AG, Benner T, et al. Direct Protein Imaging of Inflammation in the Human Hand. *Proc Int Soc Magn Reson Med*. 2011;19:2011.
  17. Harris CT, Handler WB, Araya Y, et al. Development and optimization of hardware for delta relaxation enhanced MRI. *Magn Reson Med*. 2014;72(4):1182-1190. doi:10.1002/mrm.25014.
  18. Araya YT. Delta Relaxation Enhanced Magnetic Resonance - Development and Application of a Field-Cycling Contrast Mechanism. 2013;(May):100.
  19. Araya Y, Martinez-Santiesteban F, Handler WB, Harris CT, Chronik BA, Scholl TJ. Nuclear Magnetic Relaxation Dispersion of Murine Tissue for Development of T1 (R1) Dispersion Contrast Imaging. *NMR Biomed*. 2017;(e3789). doi:https://doi.org/10.1002/nbm.3789.
  20. Lee E, de Rochefort L, Ferrante G, Rutt BK. Next generation delta relaxation enhanced MRI with  $\pm 0.36T \Delta B$ . In: *20th Annual Meeting of ISMRM*. Melbourne, Australia; 2012.
  21. de Rochefort L, Lee E, Polello M, Durrasse L, Ferrante G, Rutt BK. Characterization and Compensation of Eddy Current Induced by Insertable dreMR Magnet. In: *International Society for Magnetic Resonance in Medicine*. ; 2012.
  22. Martinez-santiesteban FM, Araya Y, Harris C, Handler WB, Chronik BA, Scholl TJ. Improving Contrast of delta relaxation enhanced MR ( dreMR ) Imaging : 2013;21:2013.

23. Lauffer RB. Paramagnetic Metal Complexes as Water Proton Relaxation Agents for NMR Imaging: Theory and Design. *Chem Rev.* 1987;87(5):901-927. doi:10.1021/cr00081a003.
24. Kimmich R, Anoardo E. *Field-Cycling NMR Relaxometry*. Vol 44.; 2004. doi:10.1016/j.pnmrs.2004.03.002.
25. Bottomley PA, Foster TH, Argersinger RE, Pfeifer LM. A review of normal tissue hydrogen NMR relaxation times and relaxation mechanisms from 1-100 MHz: Dependence on tissue type, NMR frequency, temperature, species, excision, and age. *Med Phys.* 1984;11(4):425-448. doi:10.1118/1.595535.
26. Escanyé J., Canet D, Robert J. Nuclear magnetic relaxation studies of water in frozen biological tissues. Cross-relaxation effects between protein and bound water protons. *J Magn Reson.* 1984;58(1):118-131. doi:10.1016/0022-2364(84)90011-8.
27. Eldredge HB, Spiller M, Chasse JM, Greenwood MT, Caravan P. Species dependence on plasma protein binding and relaxivity of the gadolinium-based MRI contrast agent MS-325. *Invest Radiol.* 2006;41(3):229-243. doi:10.1097/01.rli.0000199293.86956.48.
28. Caravan P, Cloutier NJ, Greenfield MT, et al. The interaction of MS-325 with human serum albumin and its effect on proton relaxation rates. *J Am Chem Soc.* 2002;124(12):3152-3162. doi:ja017168k [pii].
29. Caravan P, Parigi G, Chasse JM, et al. Albumin binding, relaxivity, and water exchange kinetics of the diastereoisomers of MS-325, a gadolinium(III)-based magnetic resonance angiography contrast agent. *Inorg Chem.* 2007;46(16):6632-6639. doi:10.1021/ic700686k.
30. Ahrens ET, Rothbächer U, Jacobs RE, Fraser SE. A model for MRI contrast enhancement using T1 agents. *Proc Natl Acad Sci U S A.* 1998;95(15):8443-8448. doi:10.1073/pnas.95.15.8443.
31. Rinck P, Muller R. Field strength and dose dependence of contrast enhancement by gadolinium-based MR contrast agents. *Eur Radiol.* 1999;1004:998-1004. doi:10.1007/s003300050781.

## Chapter 4

### 4 Conclusion

This research optimized hardware design procedures and polarization sequences for delta relaxation enhanced magnetic resonance. Limitations and future directions will be explored below.

#### 4.1 Limitations

##### 4.1.1 Chapter 2 Limitations

The split solenoid magnet design algorithm considered a limited number of parameters, and navigated parameter space using exhaustive grid searches. A grid search has the benefit of understanding the trade-offs between performance properties of the coil, but the disadvantage is the speed of the algorithm. The limitations of this approach would occur when the design parameter space becomes so large that a heuristic navigation cannot realistically take place. In this case, one could employ more sophisticated search algorithms in a modular fashion as required, while still following the general design guide.

A second limitation identified in this chapter is that the coil designs are currently restricted to solenoidal geometry. This is not an issue for application towards small animal dreMR imaging, as the limited bore size achievable with solenoids is commensurate with the sample size<sup>1,2</sup>. However, for clinical use of dreMR, coils of semi-planar geometry are a promising solution<sup>3</sup>.

### 4.1.2 Chapter 3 Limitations

Given restrictions on time and scope of this project, there was limited access to nuclear magnetic resonance dispersion data and corresponding imaging experiment data. As a result, the simulation tool that was developed is not quantitative. This has two consequences. The first is that there is difficulty in comparing the results of simulated contrast-to-noise ratio to other imaging studies. The second is that it is not generalizable within itself to other tissues or to qualitatively different pulse sequences, as these would require independent validation.

## 4.2 Future Directions

The formalism developed in Chapter 2 requires expansion to include additional design parameters such as: inner- and outer-notches, non-uniform current densities, or additional coil components. For application towards dreMR coil design, the necessities for improved performance and integration with other system components (such as shielding coils, the host MR system, eddy current compensation coils, RF coils) require a more generalized design space. Another potential use of this tool is the design of a medical device test platform for eddy-current induced vibration. In addition to a pulsed solenoid magnet, similar to the one designed, this new system would require a perpendicular static magnetic field that is an order of magnitude stronger in amplitude. The challenges here are limiting the time-varying forces and torques that would be induced on the system components themselves.

A recommended next step for the simulation tool developed in Chapter 3 is the extension to a comprehensive MRI simulator. Imaging modules that include RF pulses,

spatial gradients, and image reconstruction techniques would be necessary. The data library on tissue properties could be expanded to include information on proton density,  $T_2$  relaxation, temperature dependence, and relaxivity data on other contrast agents and biological tissues. A more thorough understanding of errors in relaxation rate data would be beneficial (from both collection and fitting of the data). Finally, more varied imaging experiments would help tease out invalid model assumptions and reveal dependence of the scaling factors on the imaging parameters. The improved simulation tool could be used for several applications related to dreMR, such as: simulation of contrast in-vivo; identifying the cause and effects of image artifacts that occur in dreMR imaging<sup>4</sup>; exploring and optimizing different pulse sequences for dreMR imaging<sup>5,6</sup>, such as inversion recovery sequences or fat suppression techniques; and even the design of new contrast agents<sup>7</sup>.

The overall objectives of this project were to advance dreMR technology by optimization of design procedures. Chapter 2 provides a coded, validated, design optimization for the primary windings of a dreMR coil. The dB/dt coil that was constructed is an example of an unshielded dreMR coil. The addition of an active shield is simple, due to the proven methods that have been published<sup>8</sup>. Chapter 3 provides the design specifications for a given application. The sequences outputted by the search algorithm indicate several requirements of the proposed coil. The field shift is related to the coil efficiency. The ramp times correlate with the inductance of the coil, as well as provide information that could help in choosing a power supply or amplifier for the coil. The power dissipated in the coil and cooling requirements could be determined from the time-varying polarization sequence. This tool could even lend knowledge to the homogeneity requirements of the coil through more sophisticated simulated phantom images. The

synthesis of these works facilitates an optimal coil design. An example approach is as follows. First is the selection of the desired imaging applications. This could range from targeting different pathology, to variations of the tissue sets of interest (including different contrast agents), to different imaging sequences. Next, all applications would follow the general simulation approach of Chapter 3 to optimize the dreMR sequences. For each simulation, the coil performance requirements would be extracted and aggregated. This information would be used in the design algorithm of Chapter 2 to find and optimize a versatile field-cycling dreMR coil magnet.

### 4.3 References

1. Alford JK, Farrar CT, Yang Y, et al. Direct Albumin Imaging in Mouse Tumour Model. In: *ISMRM*. Vol 19. ; 2011.
2. Araya Y, Martinez-Santesteban F, Handler WB, Harris CT, Chronik BA, Scholl TJ. Nuclear Magnetic Relaxation Dispersion of Murine Tissue for Development of T1 (R1) Dispersion Contrast Imaging. *NMR Biomed*. 2017;(e3789). doi:<https://doi.org/10.1002/nbm.3789>.
3. Harris CT, Handler WB, Chronik BA. A practical insert design for dreMR imaging in the human torso. In: *ISMRM*; 2012:2576.
4. Benoit-Cattin H, Collewet G, Belaroussi B, Saint-Jalmes H, Odet C. The SIMRI project: A versatile and interactive MRI simulator. *J Magn Reson*. 2005;173(1):97-115. doi:10.1016/j.jmr.2004.09.027.
5. Alford J, Rutt B, Scholl T, Handler W, Chronik B. Delta relaxivity enhanced MR (dreMR): Theory of T1-slope weighted contrast. *Proc 16th Sci Meet Int Soc Magn Reson Med*. 2008;Toronto(2006):1443. /MyPathway2008/1443.
6. Araya Y, Martinez F, Harris C, Handler W, Chronik B, Scholl T. Direct Albumin Imaging using a Delta Relaxation Magnetic Resonance Double Inversion Recovery Fast Spin Echo Sequence. In: *5th Annual World Molecular Imaging Congress*. Dublin, Ireland; 2012:SS1.
7. Hógáin DÓ, Davies GR, Baroni S, Aime S, Lurie DJ. The use of contrast agents with fast field-cycling magnetic resonance imaging. *Phys Med Biol*. 2011;56:105-115. doi:10.1088/0031-9155/56/1/007.
8. Harris CT, Handler WB, Araya Y, et al. Development and optimization of hardware for delta relaxation enhanced MRI. *Magn Reson Med*. 2014;72(4):1182-1190. doi:10.1002/mrm.25014.

## Appendices

### A. Derivation of Solutions to Time-Varying Bloch Equations

#### A.1 Longitudinal Solution

For a time-varying main magnetic field, the longitudinal Bloch equation is

$$\frac{dM_z(t)}{dt} = R_1(B_z(t)) \cdot [M_0(B_z(t)) - M_z(t)]. \quad (\text{A.1})$$

This can be rewritten in the form

$$\frac{dM_z(t)}{dt} + M_z(t)R_1(t) = R_1(t)M_0(t). \quad (\text{A.2})$$

To solve this, multiply both sides by the integrating factor  $u(t) = e^{\int_{t_0}^t R_1(\tau)d\tau}$ , since  $R_1$  is a function of field, which is a function of time. Note that

$$\frac{d}{dt} \left( e^{\int_{t_0}^t R_1(\tau)d\tau} \right) = R_1(t) \cdot e^{\int_{t_0}^t R_1(\tau)d\tau} \quad (\text{A.3})$$

such that multiplication of Equation (A.2) by the integrating factor becomes

$$\frac{d}{dt} \left[ M_z(t) \cdot e^{\int_{t_0}^t R_1(\tau)d\tau} \right] = R_1(t) \cdot e^{\int_{t_0}^t R_1(\tau)d\tau} \cdot M_0(t). \quad (\text{A.4})$$

The solution is obtained by integrating both sides with respect to time.

$$\begin{aligned} M_z(t) &= e^{-\int_{t_0}^t R_1(\tau)d\tau} \cdot \int_{t_0}^t M_0(\tau) R_1(\tau) \cdot e^{\int_{t_0}^{\tau} R_1(\tau')d\tau'} d\tau \\ &+ M_z(t_0) e^{-\int_{t_0}^t R_1(\tau)d\tau} \end{aligned} \quad (\text{A.5})$$

For a constant magnetic field,  $M_0$  and  $R_1$  are constant and the solution simplifies to the usual analytic solution to the Bloch equation.

$$M_z(t) = M_0 R_1 e^{-R_1(t-t_0)} \cdot \int_{t_0}^t e^{-R_1(\tau-t_0)} d\tau + M_z(t_0) e^{-R_1(t-t_0)}$$

$$M_z(t) = M_0 \cdot e^{-R_1(t-t_0)} e^{-R_1 t_0} \cdot (e^{R_1 t} - e^{R_1 t_0}) + M_z(t_0) e^{-R_1(t-t_0)}$$

$$M_z(t) = M_0 (1 - e^{-R_1(t-t_0)}) + M_z(t_0) e^{-R_1(t-t_0)} \quad (\text{A.6})$$

## A.2 Transverse Solution

The solution to the transverse equation is trivial given an integrating factor of

$u(t) = e^{\int_{t_0}^t R_2(\tau) d\tau}$ . The solution is

$$M_{xy}(t) = M_{xy}(t_0) \cdot e^{-i\varphi(t)} \cdot e^{\int_{t_0}^t R_2(\tau) d\tau}, \quad (\text{A.7})$$

where the phase is  $\varphi(t) = \gamma \int_{t_0}^t B_z(\tau) d\tau + \varphi(t_0)$ .

## B. Numerical Analysis

### B.1 Definitions

#### B.1.1 Error

Round-off error is the difference between the exact mathematical value and the representation of the number by the computer in floating point precision. In a 64-bit representation, 52 bits are used to represent the fractional part of a number. This means that a number represented in this system has at least 15 digits of precision. The MATLAB

function *eps* returns the distance from 1.0 to the next larger double-precision number, that is,  $\text{eps} = 2^{-52}$ , which is approximately  $2.22045 \times 10^{-16}$ .

For some value  $y$  and its approximation  $y^*$ , the absolute forward error is defined as the absolute difference between  $y$  and  $y^*$ . The relative error, if  $y$  is non-zero, is the absolute error divided by the magnitude of  $y$ . The percent error is the relative error times 100%. All three terms have their uses. For example, consider the case of a very small absolute error, but an even smaller value of  $y$ . Here, the presenting the absolute value would be misleading, and the relative value would give a better representation of the accuracy of the approximation. The residual error for an initial-value-problem is

$\delta(t) = \|y'(t) - f(t, y(t))\|$ , and measures how far the computed trajectory is from satisfying the differential equation<sup>1,2</sup>. If the residual is small, it can be said that the numerical solution gives the exact solution to a nearby problem<sup>3</sup>.

The local truncation error of a particular iteration is the difference between the exact solution and the solution of the numerical method at that iteration, assuming no previous errors were introduced. The global error is the maximum error of the method over the entire range of the approximation, assuming only that the method gives the exact result at the initial value.

### B.1.2 Stability

A method is said to be consistent if, in the limit that the step size approaches zero, the local truncation error approaches zero. A method is said to be convergent if in the limit

that the step size approaches zero, the difference between the approximation at each step and the exact answer approaches zero.

The concept of stability used in dynamical systems – a property of a problem, not a numerical algorithm – is corresponds to being well-conditioned<sup>3</sup>. This means the problem's inherent sensitivity to initial conditions, or rather, a measure of its output variance under input perturbation.

When solved separately by longitudinal and transverse components, the Bloch equations are considered to be well-conditioned because the solutions constantly decay towards the equilibrium configuration. When the full equation is solved in the lab frame, the system is not so well-behaved because of the ensemble of very large/small numbers and fast/slow moving components<sup>4</sup>. It is unknown if the Bloch equations are well-conditioned for field-cycling applications.

Numerical stability is concerned with how an algorithm handles the growth of approximation errors when calculating the solution. Thus, if a method has local truncation error has rate of convergence  $O(h^n)$ , it is considered numerically stable if the global error has the same rate of convergence<sup>5</sup>. If a fixed time-step method with step size  $h$  has residual  $O(h^n)$  as  $h$  approaches zero, it said to be an  $n$ th-order method. In general, the higher order a method is, the more accurate it is.

### B.1.3 Stiffness

There is no rigorous definition of stiffness. Stiffness can occur when the problem is *too* well-conditioned, or when the stability becomes the constraint on time rather than

accuracy, making the step-size very small and inefficient for explicit methods like *ode45*. The solver can fail, diverge, or take a very long time to complete. There is no explicit definition of stiffness, but factors in what makes a problem stiff are: the equations to be solved, the ODE solver, the initial conditions, the error tolerance, the time interval. Implicit solvers designed for stiff problems, like *ode15s*, do more work per step, but are able to take larger steps<sup>6</sup>.

### B.1.4 Tolerance

For fixed-step solvers, error is controlled by setting the step size. For adaptive step methods like *ode45* and *ode15s* error is controlled by setting the tolerance. *RelTol* is the relative accuracy tolerance and controls the number of correct digits in the computed answer. *AbsTol* is the absolute error tolerance and controls the difference between the computed answer and the true solution. At each step, the error  $e$  in component  $i$  of the solution satisfies

$$|e(i)| \leq \max[\text{RelTol} * \text{abs}(y(i)), \text{AbsTol}(i)].$$

If the absolute tolerance is bigger than the solution component, this specifies that no digits in the component need to be correct. The solver might have to get some correct digits in this component to compute other components accurately still.

This point is crucial when solving the longitudinal magnetization function for realistic values of magnetization. These values are on the order of  $10^{-5}$  and smaller, therefore the relative tolerance must be set significantly smaller than this. This is an even

bigger problem when calculating transverse magnetization, since the solution approaches zero with an exponential envelope and passes through zero sinusoidally.

## B.2 Solving for Longitudinal Magnetization

The following will discuss candidate solutions and implementations of the time-varying Bloch equations.

### B.2.1 Analytical Expressions

Equation (A.6) is the analytical solution for longitudinal magnetization after a  $90^\circ$  RF pulse for a static external magnetic field. This is considered to be the exact answer, when applicable. An adaptation of this equation is given by Equation (3.5), which can be implemented using a *for-loop*. The effect this has is similar to splitting the sequence into a left Riemann sum – that is, the magnetic field is approximated at the left-end point of a series of rectangular shapes. Therefore, this method should underestimate the result when the sequence is increasing, and overestimate when it is decreasing. However, since the  $j+1$  solution depends on the  $j^{\text{th}}$  component, there may be a build-up of error.

```
Mz_loop = zeros(size(Meq)); % preallocate space
Mz_loop(1) = Mz0; % set initial condition Mz(t=0)
rlx = R1(2:end).*diff(bTime); % Incremental R1 * increment
time step
for j = 1:length(bTime)-1
    Mz_loop(j+1) = Meq(j+1).*(1-exp(-
rlx(j)))+Mz_loop(j).*exp(-rlx(j));
end
```

**Code 1:** Loop method.

Equation (A.5) is the solution in the general case (still no transverse components of magnetic field). Implementation of this equation is very straightforward and used the

cumulative trapezoidal integration method, *cumtrapz*, to calculate magnetization. Note  $Mz_0$  is  $Mz(t=0)$ .

```
R1cumulative = cumtrapz(bTime,R1); % integrate for R1
bigIntegral = cumtrapz(bTime,Meq.*R1.*exp(R1cumulative));
Mz_int = exp(-R1cumulative).*bigIntegral + Mz0.*exp(-
R1cumulative);
```

**Code 2:** Integral method.

Another method to be compared is the one proposed by Hoelscher et al. for a typical dreMR subtraction-method sequence<sup>7</sup>. The expression is given as

$$M_{z\pm} = M_0 \cdot \frac{B_0 \pm \Delta B_{eff}}{B_0} [1 - \exp(-(R_1 \pm \Delta B_{eff} R_d) T_{evol})] \quad (B.1)$$

where

$$\Delta B_{eff} = \Delta B \left[ \frac{t_3 + 0.5(t_2 + t_4)}{t_2 + t_3 + t_4} \right] \cdot e^{-R_1' t_5}, R_d = \frac{dR_1}{dB}, \text{ and } R_1' = R_1 \cdot (1 - e^{-R_1 T_{evol}})^{-1}. \quad (B.2)$$

The trapezoid field shift is approximated by a step-function halfway through the ramps, and the effective B-field is supposed to correct the field with a ratio of time-on to time-off multiplied by an exponential decay term during the wait-time after a field shift but before imaging.

## B.2.2 Numerical Methods

Euler's method is the most basic method for explicit numerical integration of ordinary differential equations. This method uses the slope of the tangent at the current point to predict the slope at the next point. For example, given an initial value problem

$y'(t) = f(t, y(t))$ , where  $y(t_0) = y_0$ , the fundamental theorem of calculus tells us that  $y(t_{i+1}) = y(t_i) + \int_{t_i}^{t_{i+1}} y'(u) du$ . Euler's method will solve this by

$$\tilde{y}_{i+1} = y_i + hf(t_i, y_i) \quad (\text{B.3})$$

where  $h$  is the step size between two successive points,  $t_{i+1} = t_i + h$ . This fixed-step, first-order method has poor efficiency. The local error (error per step) is proportional to  $h^2$ , but the global error is proportional to  $h$ . This solver produces exact answer for constant functions, but anything of higher order loses accuracy.

A modification of this is given as Heun's method, called a predictor-corrector method. Euler's method is used to predict the slope at the next point, and the trapezoid rule is used to correct the slope of the line tangent, combining a forward and backward method. Heun's method has local error on the order of  $O(h^3)$  and is exact for linear functions. The solution is given by the following equation and the implementation is shown in Code 3.

$$y_{i+1} = y_i + \frac{h}{2} [f(t_i, y_i) + f(t_{i+1}, \tilde{y}_{i+1})] \quad (\text{B.4})$$

```

% Write the anonymous function
func = @(MZ,R1,Meq) R1.*(Meq-MZ); % dMzdt = 1/T1.*(m0-mz);
n = length(timePoints); % number of steps
R1 = inputStruct.R1; % relaxation rate
Meq = inputStruct.Meq; % equilibrium magnetization

MZ = zeros(1,n); % solution for Mz, same length as B
MZ(1) = obj.tissue.Mz0; % set initial condition

% Perform the fixed step calculations
for i = 1:n-1
    h = timePoints(i+1)-timePoints(i); % step size
    k1 = func(MZ(i),R1(i),Meq(i));
    mz_interm = MZ(i) + h*k1; % predictor (Euler)
    MZ(i+1) = MZ(i) + h/2*(k1 +
func(mz_interm,R1(i+1),Meq(i+1)));
    % ^ corrector, (trapezoid)
end

```

**Code 3:** Heun's method.

The Runge-Kutta (fourth and fifth order) method, as implemented in MATLAB as *ode45* using the Dormand-Prince method<sup>8,9</sup>, estimates the value  $y_{i+1}$  by using a weighted average of four increments between  $y_i$  and  $y_{i+1}$ .

$$\begin{aligned}
 s_1 &= f(t_i, y_i) \\
 s_2 &= f\left(t_i + \frac{h}{2}, y_i + \frac{h}{2}s_1\right) \\
 s_3 &= s_2 \\
 s_4 &= f(t_i + h, y_i + hs_3) \\
 y_{i+1} &= y_i + \frac{h}{6}(s_1 + 2s_2 + 2s_3 + s_4). \tag{B.5}
 \end{aligned}$$

This solver has error on the order of  $O(h^4)$  from the RK4 method, and uses an estimation of the local truncation error with the RK5 method to adaptively choose the step-size to control the error as well as the speed of the algorithm. This is implemented in MATLAB using the function *ode45* with a nested anonymous function to pass in time-varying parameters, shown in Code 4. When the problem is considered stiff, for example possibly

when the time span is very long, the solver *ode15s* should be tried instead; a variable-step, variable-order solver.

```

func = @(tissueAnon,bTimeAnon,bFieldAnon) (@(t,mz)
MagPrep.calc_Mz(t,mz,tissueAnon,bTimeAnon,bFieldAnon));
opts = odeset('RelTol',tol1,'AbsTol',tol1); % set tol

% Calculate magnetization using ode45.
[T,Mz] = ode45(func(Tissue,bTime,bField),bTime,Mz0,opts);

function [dMzdt] = calc_Mz(t,mz,tissue,bT,bF)
    B = interp1(bT,bF,t); % interp to internally chosen time
    m0 = calculateM0(tissue,B); % get M0 at this field
    R1 = get(tissue,'R1',B); % get R1 at this field
    dMzdt = R1.*(m0-mz); % Eval ODE. R1 = 1/T1;
end

```

**Code 4:** ode method.

### B.2.3 Analysis of Algorithms

With the fixed-step solvers (loop, integral, Heun), one needs to be careful not to make the step size too small, else there is a concern for rounding errors and cancellation. The loop method can be thought of as a left Riemann sum and this method has error on the order of  $O(h)$ . The integral method uses trapezoidal integration, which has error on the order of  $O(h^2)$ . Euler's method is  $O(h)$ , but Heun's method improves upon this and is  $O(h^2)$ , in both cases the local error of these methods is one order higher. The MATLAB method *ode45* has error on the order of  $O(h^4)$  and *ode15s* is a variable order method, ranging from one to five. The method proposed by Hoelscher et. al. is difficult to assess numerically. Likely the dominant errors will be due to poor modeling of the problem.

In all methods, linear interpolation is used to obtain the values of time-varying relaxation rate and equilibrium magnetization. Furthermore, for the ode methods, when

specifying the solution at times other than the internally chosen steps, the algorithm uses polynomial interpolation.

### B.3 Evaluation of Longitudinal Magnetization Methods

The evaluation of the candidate longitudinal calculation methods will take place over the following cases of magnetic field:

1. Flat field, short time scale.
2. Flat field, long time scale.
3. A field-shift with modest amplitude and ramp times.
4. A large field-shift with quick ramp times.
5. The case described by Hoelscher et. al. to test their method.

These sequences (except for case 2 – which is the same as case 1, but for 10 seconds) and solutions are shown in Figure B.1. For each case, testing will occur at millisecond sampling as well as at 2.1 times the Nyquist rate. This corresponds to the step size for the relevant methods. For the ode methods, the tolerance values are set as follows:  $\text{RelTol} = 2.22045\text{e-}14$ ,  $\text{AbsTol} = 2.22045\text{e-}16$ , which are the lowest possible relative tolerance to set, and the floating pointing relative accuracy  $\text{eps}$ . Although, probably a better *arbitrary* absolute tolerance would be  $\text{eps}(x)$  where  $x$  is the value of equilibrium magnetization, and is on the order of  $1\text{e-}5$ .

Evaluation will be in the form of accuracy, speed, and a qualitative description of convergence. Various plots of errors, step sizes, and residuals are shown in the remaining figures of Section B.3. The percent error is taken with respect to the accepted solution – for cases 1 and 2, this is the analytical expression of Equation (A.6). For the other cases, this expression is invalid, and the ode45 solution is used. A summary of maximum percent

error, end-point percent error, and runtime for each case are given in the tables associated with each figure.

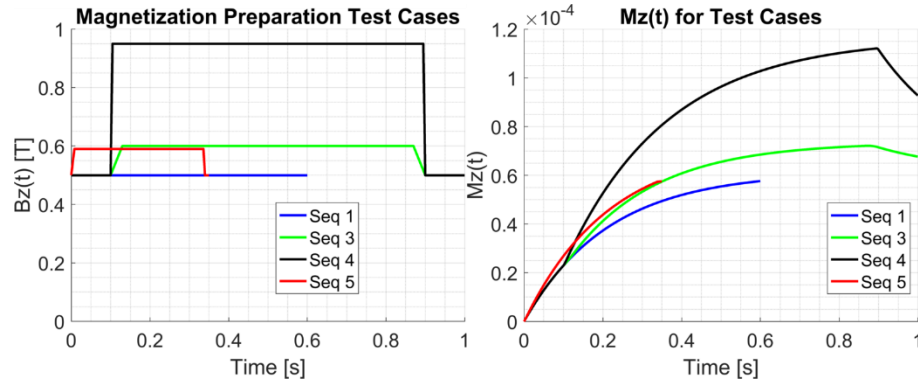


**Figure B.1:** a) Test sequences for evaluating longitudinal magnetization calculation methods, with b) their corresponding  $M_z(t)$  calculated with the integral method, for a tissue with a large  $R_1$  dispersion.

### B.3.1 Case 1

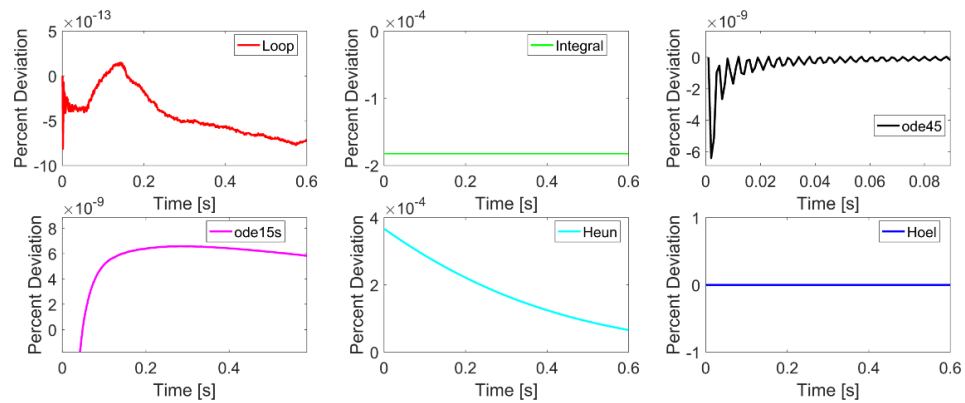


**Figure B.2:** Percent error of different methods with respect to the analytical solution. In this case, the Hoelscher solution reduces to the analytical expression. The integral method has a constant offset. The ode45 method converges and oscillates within the specified tolerance, while the ode15s method is more smooth. Heun's method also has a smooth approach, but it is quite slow.

Method	ms sampling			Nyquist sampling		
	Max [%]	End [%]	Time [s]	Max [%]	End [%]	Time [s]
Loop	8.14E-13	7.17E-13	0.0015	2.64E-08	3.24E-09	4.4
Integral	0.00018	0.00018	0.0017	4.33E-08	4.33E-08	1.9
ode45	6.40E-09	4.00E-11	0.1478	1.64E-08	4.03E-11	214
ode15s	1.04E-07	5.77E-09	0.1471	4.00E-05	5.74E-09	362
Heun	0.00037	6.60E-05	0.0019	1.64E-08	1.12E-12	31
Hoelscher	0	0	0.0023	0	0	1.1

**Table B.1:** Data summary for case 1. The integral method is still a constant offset with more steps, but that constant is much smaller. Heun’s method shows significant improvement with more steps. The ode methods generally result in the same accuracy regardless of step size (with constant tolerances), however the significant time difference is a result of passing large amounts of data through the algorithms of *ode*, various interpolation, and *get* functions.

### B.3.2 Case 2

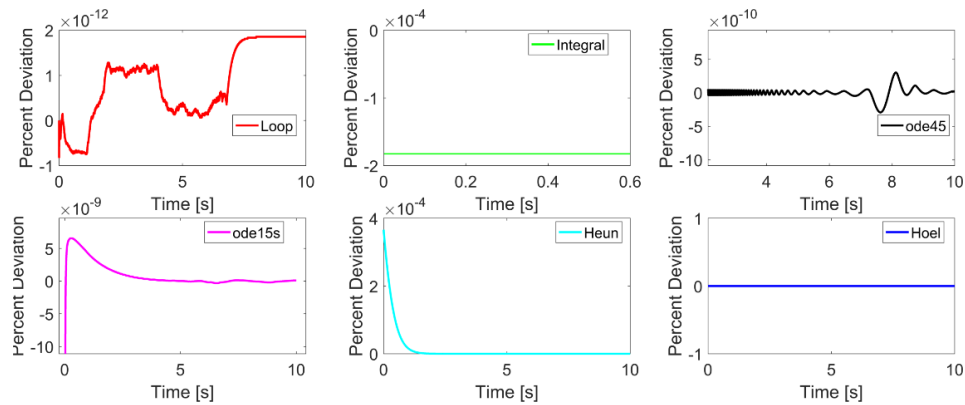


**Figure B.3:** Percent error of different methods with respect to the analytical solution. After a certain time, the problem may perhaps show stiffness as the solutions for ode45, ode15s, and Heun all tend to show instability. The ode solutions are still within the bounds of their tolerance, else the calculation would fail. However, it is not clear the extent to which Heun’s solution would grow – even though the instability occurs of the order of 1e-10 (not shown).

Method	ms sampling		
	Max [%]	End [%]	Time [s]
Loop	1.86E-12	1.86E-12	0.0021
Integral	0.00018	0.00018	0.0064
ode45	6.40E-09	2.09E-11	0.42
ode15s	1.04E-07	8.29E-11	0.40
Heun	0.00037	2.36E-12	0.017
Hoelscher	0	0	0.0024

**Table B.2:** Data summary for case 2. Nyquist sampling could not be obtained for this case due to the large amounts of memory required. The runtime for the ode45 and ode15s methods were

3811 and 5606 seconds, respectively, again not due to calculation time but to interpolation time and handling of the large arrays.

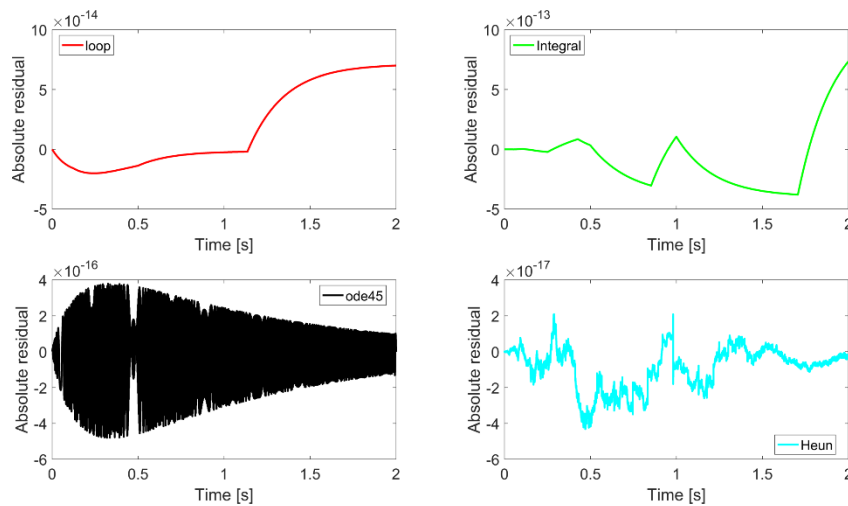


**Figure B.4:** Absolute residual error for case 2 with respect to the analytical solution. The fixed-step solvers were computed at Nyquist sampling, while the ode45 method used the chosen time points and deval to interpolate onto the same steps as the others. All methods show very small residuals and are approximately on the same order as their absolute forward error (not shown).

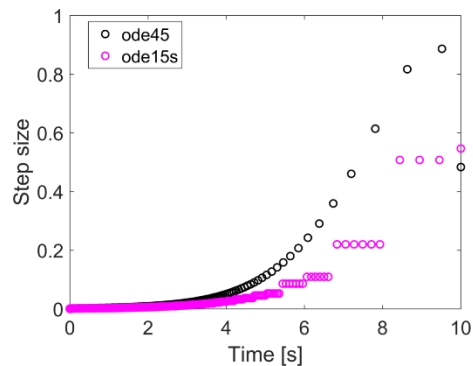


**Figure B.5:** True step size for the ODE methods of case 2. As the solution converges to equilibrium magnetization, the step size increases for both methods. This is an indication that the problem is non-stiff, and the apparent growth of oscillation in the percent error plot above is due to polynomial interpolation between the points chosen by MATLAB to evaluate the ODE.

### B.3.3 Case 3

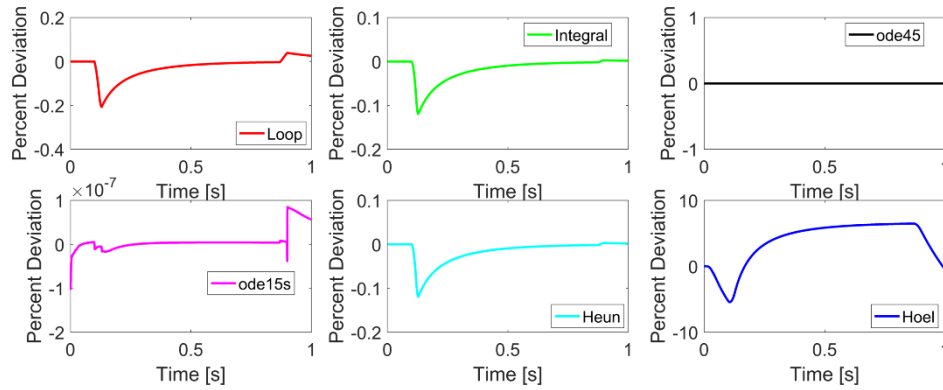


**Figure B.6:** Percent error of different methods with respect to the ode45 solution. The small oscillations characteristic of ode45 is present in all solutions, but on an order much smaller than is visually present. The fixed step solvers (loop, integral, and Heun) all show the same shape of residual – that is, they over-predict during ramp-up, and under-predict during ramp-down.

Method	ms sampling			Nyquist sampling		
	Max [%]	End [%]	Time [s]	Max [%]	End [%]	Time [s]
Loop	0.21	0.026	0.0051	0.12	0.0020	10
Integral	0.12	0.0019	0.017	0.12	0.0020	4.5
ode45	0	0	0.56	0	0	463
ode15s	8.48E-08	5.65E-08	0.60	1.80E-08	1.02E-08	635
Heun	0.12	0.0020	0.0083	0.12	0.0020	87
Hoelscher	6.5	0.49	0.0094	6.5	0.49	2.1

**Table B.3:** Data summary for case 3. The loop method improves by an order of magnitude with more steps. It is not clear by the other methods do not.

### B.3.4 Case 4

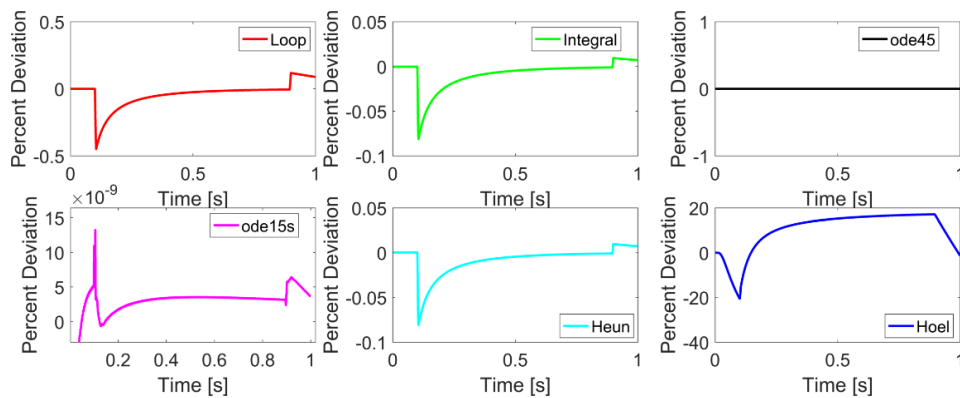


**Figure B.7:** Percent error of different methods with respect to the ode45 solution.

Method	ms sampling			Nyquist sampling		
	Max [%]	End [%]	Time [s]	Max [%]	End [%]	Time [s]
Loop	0.45	0.089	0.0048	0.091	0.0067	17
Integral	0.081	0.0071	0.018	0.091	0.0067	7.1
ode45	0	0	0.55	0	0	701
ode15s	1.33E-08	3.68E-09	0.66	1.77E-08	3.39E-09	1060
Heun	0.081	0.0072	0.0094	0.091	0.0067	137
Hoelscher	21	1.3	0.0100	20	1.3	3.9

**Table B.4:** Data summary for case 4.

### B.3.5 Case 5

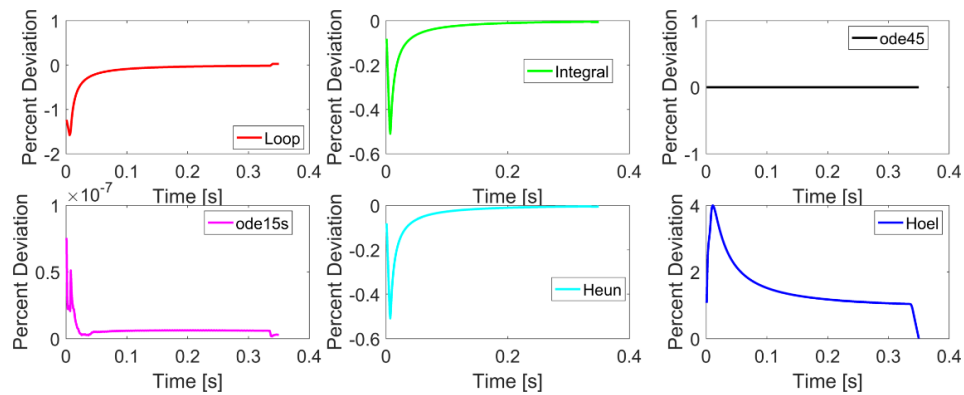


**Figure B.8:** Percent error of different methods with respect to the ode45 solution.

Method	ms sampling			Nyquist sampling		
	Max [%]	End [%]	Time [s]	Max [%]	End [%]	Time [s]
Loop	1.5	0.028	0.0055	0.41	0.0056	3.8
Integral	0.47	0.0057	0.020	0.41	0.0056	1.8
ode45	0	0	0.43	0	0	193
ode15s	5.12E-08	2.85E-09	0.46	6.73E-07	3.21E-08	203
Heun	0.47	0.0053	0.0075	0.41	0.0056	27
Hoelscher	4.0	0.0027	0.013	4.0	0.0027	0.89

**Table B.5:** Data summary for case 5. The fixed-solvers are effectively identical, both in terms of shape and accuracy. The longitudinal magnetization calculated with the Hoelscher method (which is never actually evaluated in that paper) is surprisingly accurate by the end of the sequence, but has a large maximum error, and does not behave smoothly.

### B.3.6 Discussion

It is unfortunate that there is no closed-form solution to the Bloch equations for a time-varying external magnetic field. It brings uncertainty to the evaluation of cases 3-5.

One method must be chosen to be the accepted solution, from which the other methods will be compared. It is noted that the evaluations are no longer for the original problem, but on the nearby problem of which the accepted solution is taken to be exact.

The integral method, Equation (A.5), is the best analytical solution to the problem, but must be evaluated numerically (Code 2), and since this has not been tested previously it is not prudent to use this as the accepted solution. The reason ode45 was chosen as the accepted solution is because of the consistency with which this method yields accurate solutions, and because it is a well-established built-in MATLAB function which has been optimized over years. Furthermore, based on cases 1 and 2, in short time-intervals this method will yield well-behaved solutions to within the specified tolerance, with small residual error. The apparent oscillations in the ode45 solution are due to polynomial interpolation that is used to produce points in between the true steps that ode45 takes, and is bound by the tolerance values. In all cases, ode45 was faster than ode15s indicating, along with Figure (B.5), that the longitudinal Bloch equation is non-stiff.

In general, all fixed-step methods have the same or improved accuracy with an increased number of steps. An exception sometimes occurs for the loop method, in which it is suspected that a build up of round-off errors have been introduced with the decreased step-size. For cases 1 and 2, all methods would be deemed acceptable for use in this application at millisecond sampling, including the integral method if it could be shown that the systematic offset occurs for all tissues equally and the effect this has on sequence design is negligible. The downside of increased accuracy at the higher sampling rate is the large amounts of memory required to compute and store the solution.

Cases 3 and 4 indicate that varying ramp times do not have a drastic effect on accuracy. However, field-cycling in general does reduce accuracy overall (compare to case 2). All fixed-step solvers would be considered acceptable for these cases. The Hoelscher method has unacceptably large error and shows little consistency in its solutions. A maximum percent error of 4, 6, and even 20 is very poor, and even though the percent error at the end points are much lower, the solution seems superficial and is not considered to be in the same class as the other methods. Furthermore, the cases to which the Hoelscher method can be applied are limited. This method is not designed to handle arbitrary pulse sequences, and can barely keep up with simple numerical methods in the cases for which it was designed.

To conclude, for future simulations, the ode45 method should be used for best accuracy and consistency. However, if time is a constraint, the integral method could be used instead.

## B.4 Solving for Transverse Magnetization

This section will compare three ways to solve for transverse magnetization, both in terms of speed and accuracy. Solving the differential equations numerically is orders of magnitude faster when computed in the rotation frame, with no loss in accuracy. Note that the implementations shown below assume the rotating frame is on-resonance (neglecting the field-shifts themselves).

Note that when solving for transverse magnetization, it is important to adhere to the Nyquist-Shannon sampling theorem which states that in order to accurately represent all frequencies in a time signal, the sample rate must be higher than twice the highest

frequency in the signal, in order to avoid aliasing. That is, for a magnetization preparation sequence with  $B_z(t) = B_0 + \Delta B(t)$ , the sampling frequency must be  $\nu \geq 2 \left( \frac{\gamma}{2\pi} \right) \cdot \max(B_z(t)) = 2 \cdot \left( 42.577 \frac{\text{MHz}}{\text{T}} \right) \cdot \max(B_z(t))$ . Implementing the combined Bloch equations is an extension of the approach shown in Code 4.

```
function [dMdt] = calc_Mrot(t,M,bT,bF,R1all,R2all,m0all)
B0 = tissue.B0;
gamma = 2.675*10^8; % gyromagnetic ratio for proton
Bx = interp1(bT,bF(1,:),t); % Bx at time point t
By = interp1(bT,bF(2,:),t); % By
Bz = interp1(bT,bF(3,:),t); % Bz
m0 = interp1(bT,m0all,t); % get m0 at chosen t
R1 = interp1(bT,R1all,t);
R2 = interp1(bT,R2all,t);

% Perform cross product MxB
MxB = cross([M(1),M(2),M(3)], [Bx,By,Bz-B0]);

% Solve linear system of equations
dM1 = gamma.*MxB(1) - R2.*M(1);
dM2 = gamma.*MxB(2) - R2.*M(2);
dM3 = gamma.*MxB(3) + R1.*(m0-M(3));

dMdt = [dM1;dM2;dM3];
end
```

**Code 5:** full ode method.

It is faster still to solve both individual components separately than to solve equation them together. Solving for Equation (3.2) is done with the following function. Recall that  $M_x = \text{Re}(M_{xy})$  and  $M_y = \text{Im}(M_{xy})$ .

```

function [dMxy] = calc_Mxyrot(t,Mxy,bT,bFz,R2all,B0)
gamma = 2.675*10^8; % gyromagnetic ratio for proton
Bz = interp1(bT,bFz,t); % Bz
R2 = interp1(bT,R2all,t);

dMxy = -Mxy.*(complex(R2,gamma.*(Bz-B0)));
end

```

**Code 6:** xy ode method.

The transformation from rotating frame to laboratory frame is completed by multiplying the vector  $M$  with rotation matrix  $R$ , where

$$R_z(\theta) = \begin{bmatrix} \cos \theta & -\sin \theta & 0 \\ \sin \theta & \cos \theta & 0 \\ 0 & 0 & 1 \end{bmatrix}, \theta = -\omega_0 t. \quad (6)$$

Finally, implementing the expression shown in equation (A.7) is done with cumulative trapezoidal integration.

```

phaseRot = gamma.*cumtrapz(bT,[bF(3,:)-B0]); % rot frame
phase
[keys,~,IC] = unique(bF(3,:)); % Bz(t)
uR2 = 1./(get(flat,'T2',keys)); % R1 values at unique Bz
R2 = uR2(IC); % mapping unique R1 to R1(t)

Mxyrot = Mz0.*exp(-i.*phaseRot).*exp(-cumtrapz(bTime,R2));

```

**Code 7:** Integral method.

It would be extremely incorrect to write the second exponential as  $\exp(-R_2 \cdot t)$ , without the integration. Most of the time it would have no effect (that is, for tissues with small  $R_2$  dispersion, or for small field shifts), nonetheless it is quite inaccurate, and leads to a qualitatively different looking signal.

## B.5 Evaluation of Transverse Magnetization Methods

The evaluation of the transverse methods will take place over the following cases:

1. Flat field, short time scale.
2. Flat field, long time scale.
3. A very small field-shift.
4. A very large field-shift.

These sequences and solutions are shown in Figure B.9. For each case, testing will occur at 2.1 times the Nyquist rate. Evaluation will be in the form of accuracy, speed, and a qualitative description of convergence. The error for each method, for each case, are shown in the remaining figures in Section B.5. The accepted solution for cases 1 and 2 are given in Equation (1.6a). This expression is invalid when field-cycling occurs (cases 3 and 4), and the integral method is used then. A summary of maximum absolute error, end-point absolute error, and runtime for each case are given in the following tables.

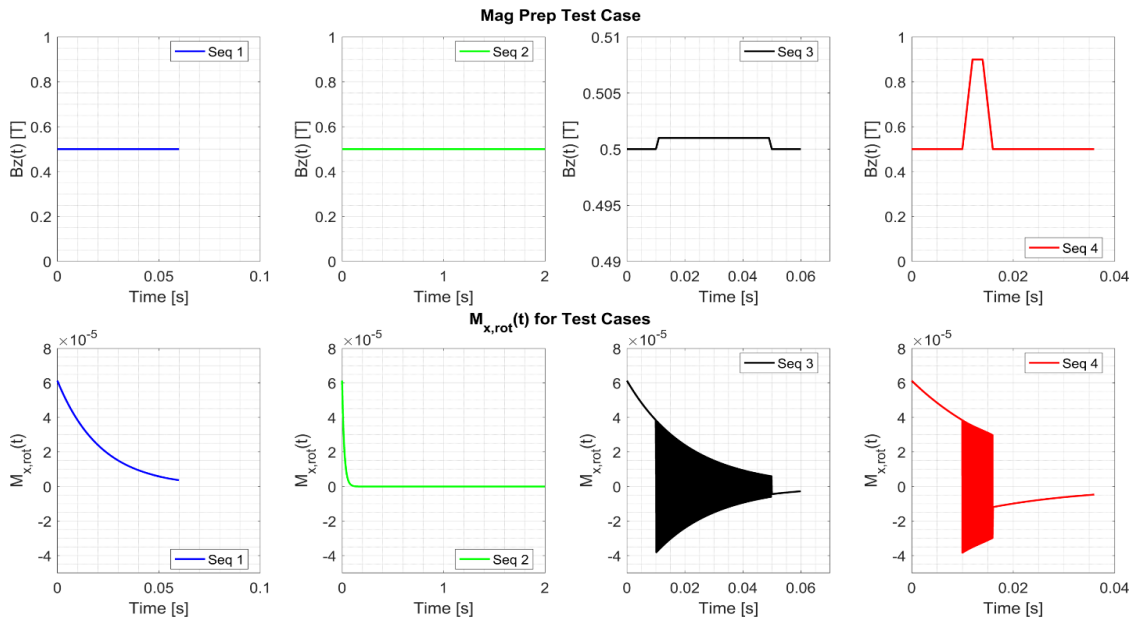


**Figure B.9:** Test sequences for evaluating transverse magnetization calculation methods (top row), with their corresponding  $M_x(t)$  calculated with the integral method in the rotating frame (bottom row).

### B.5.1 Case 1

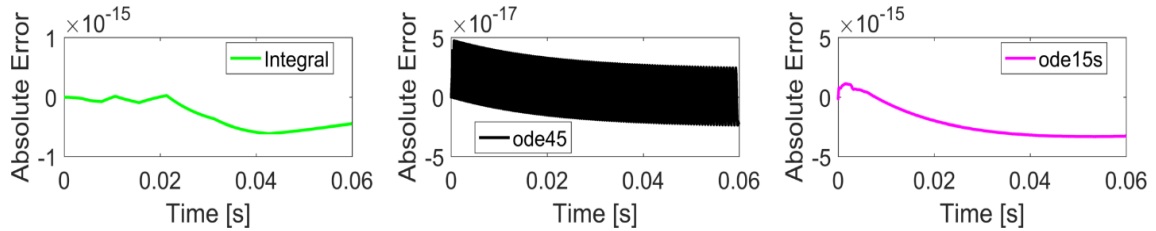


**Figure B.10:** Absolute error of different methods with respect to the analytical solution. All methods have similar overall shape. ode45 has the smallest absolute error, and also its characteristic oscillatory solution.

Method	abs Err Max	abs Err End	Time [s]
Integral	6.11E-16	4.45E-16	0.30
ode45	4.76E-17	2.30E-17	20
ode15s	3.31E-15	3.24E-15	32

**Table B.6:** Data summary for case 1. All methods show small and similar values for absolute error. The analytical solution at the final time point is on the order of  $1e-6$ , thus there is good relative error too. The relative error for the ode45 method is  $6.34e-10$ .

### B.5.2 Case 2

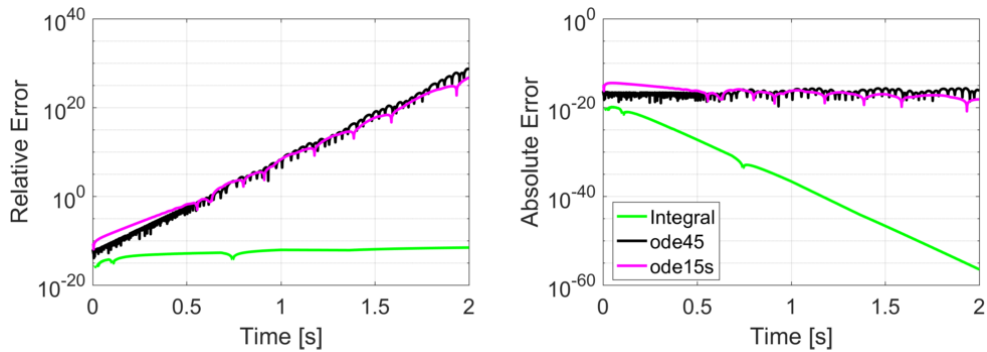


**Figure B.11:** Relative (left) and absolute (right) error of different methods with respect to the analytical solution. Since the solution approaches zero, the ode methods have poor relative error once the exact solution is less than the relative tolerance. The stability of the ode45 method is again questioned for long time spans.

Method	abs Err Max	abs Err End	Time [s]
Integral	6.11E-16	9.93E-53	9
ode45	2.47E-16	4.20E-17	803
ode15s	3.31E-15	6.21E-20	1118

**Table B.7:** Data summary for case 2. The analytical solution at the end is on the order of  $1e-45$ , so an absolute error of  $1e-17$  is terrible. The time required by the ode methods is not related to

stability, but rather to the handling of large arrays passed between the various algorithms including: ode45, ode15s, interp1, get, ntrp45, etc.

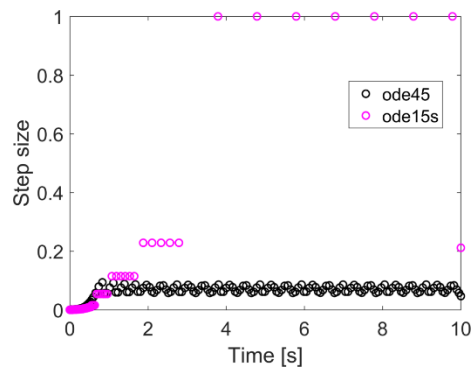


**Figure B.12:** True step size for the ODE methods of an extended case 2. As the solution converges to zero (this is a well-conditioned problem), the step size increases for ode15s but stays small for ode45. This is an indication that the problem is stiff. The time taken for the two methods when the time span contains only the initial and final times was 0.62 s and 0.17 s for ode45 and ode15s, respectively. The fact that ode15s performed faster is further evidence of stiffness.

### B.5.3 Case 3

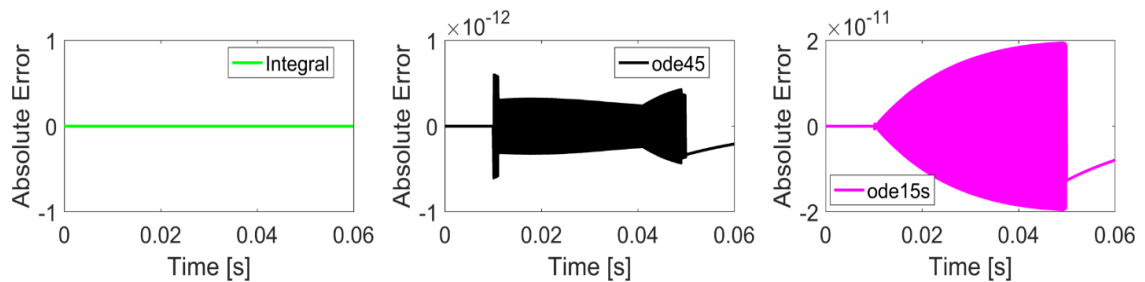


**Figure B.13:** Absolute error of different methods with respect to the integral solution. The error is drastically higher during the field-cycling portion, but approaches zero once the field ramps back down. It may be that there is a simple offset in amplitude or in phase which causes the error, but considering the different shapes of the residuals, it is unclear. An attempt was made to solve the ode at the chosen time step, then interpolate onto the time step of the integral method to see the effect on absolute error. While the shape of the residuals is more consistent, the absolute error is several orders of magnitude larger trying both linear and cubic interpolation.

Method	abs Err Max	abs Err End	Time [s]
Integral	0	0	0.33
ode45	4.28E-13	2.08E-13	816
ode15s	1.95E-11	7.91E-12	592

**Table B.8:** Data summary for case 3. The integral method is still very fast even with field-cycling. The time to solve without dictating the evaluated time steps was 325 and 106 seconds for ode45 and ode15s, respectively.

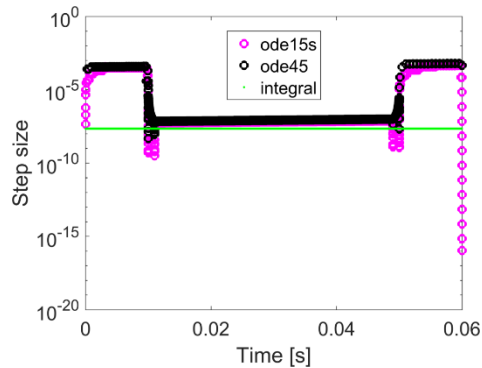


**Figure B.14:** True step size for the ODE methods of an extended case 3. Note that the fixed-step solver maintains equal step size throughout the solution, and that the adaptive methods have step sizes generally larger than this. As the problem becomes ill-conditioned during the field-cycling phase, the step size decreases for both methods. This is not an indication of stiffness, just instability. The ode15s method takes many small steps at the very end to meet some internal exit criteria.

#### B.5.4 Case 4

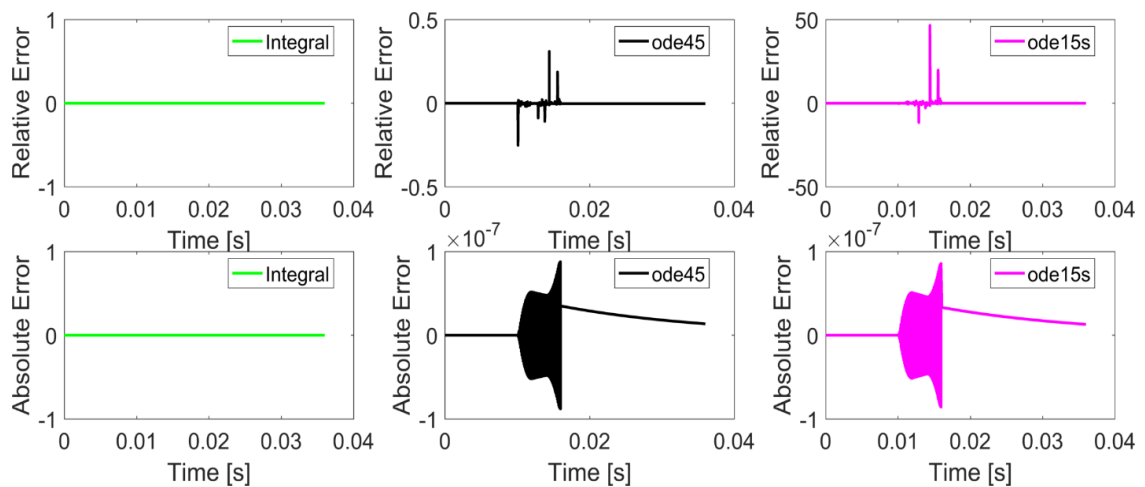


**Figure B.15:** Relative (top) and absolute (bottom) error of different methods with respect to the integral solution. The spikes in relative error are due to catastrophic cancellation because the solution

passes through zero. It is unclear why the shape of the absolute error curves are similar here while being different in the above case. It may be because after the first spike, the ode solutions are effectively meaningless.

Method	abs Err Max	abs Err End	Time [s]
Integral	0	0	0.31
ode45	8.78E-08	1.38E-08	23084
ode15s	8.57E-08	1.31E-08	6862

**Table B.9:** Data summary for case 4. The solution at the end of the test is on the order of  $1e^{-6}$ , so an absolute error of  $1e^{-8}$  is on the order of 1%. Due to the high field shift and consequent sampling rate, the ode solutions took a substantial amount of time to complete.

### B.5.5 Discussion

It is immediately clear that when solving the transverse Bloch equation, the integral method is best. It is consistently orders of magnitude faster than the ode methods. On short time intervals, with no field-shifting (case 1) it is just as accurate as the ode methods. But the winning trait is its reliability. The solution converges smoothly and quickly and is not affected by stiffness. In case 2 the differences are clear. The integral method has continually smaller absolute error as the solution approaches zero, with essentially constant relative error. This behaviour is the opposite for the ode methods making them essentially useless. The trade-off is the memory it takes to store these solutions. In case 4, the integral method uses 20 MB and the ode methods use 0.2 KB of memory – a ratio of 100,000 between the two.

In general, calculating in the rotating frame is much faster than in the laboratory frame. There may be a technique available that uses a secondary rotating frame (during field-shifting) to increase the speed of calculation, although the effect on accuracy is unknown. Furthermore, calculation of the full Bloch equations is much slower than the sum of individual calculations. Unfortunately, this isn't always possible, especially during excitation by an RF pulse. However, when it is possible, it is best to use the ode45 or

integral method to calculate longitudinal magnetization, and the integral method to calculate transverse magnetization.

## C. References for Appendices

1. Shampine LF. Error Estimation and Control for ODEs. *J Sci Comput.* 2005;25(1):3-16. doi:10.1007/s10915-004-4629-3.
2. Corless RM. A new view of the computational complexity of IVP for ODE. *Numer Algorithms.* 2002;31(1-4):115-124. doi:10.1023/A:1021108323034.
3. Corless RM, Fillion N. *A Graduate Introduction to Numerical Methods: From the Viewpoint of Backward Error Analysis.* Springer Science+Business Media; 2013. doi:10.1007.
4. Balac S, Chupin L. Fast approximate solution of Bloch equation for simulation of RF artifacts in Magnetic Resonance Imaging. *Math Comput Model.* 2008;48(11-12):1901-1913. doi:10.1016/j.mcm.2007.05.021.
5. Burden RL, Faires JD. *Numerical Analysis.* Ninth Edit.; 2011. [http://www.lavoisier.fr/livre/notice.asp?ouvrage=1248244%5Chttp://books.google.es/books/about/Numerical\\_Analysis.html?id=zXnSxY9G2JgC&pgis=1](http://www.lavoisier.fr/livre/notice.asp?ouvrage=1248244%5Chttp://books.google.es/books/about/Numerical_Analysis.html?id=zXnSxY9G2JgC&pgis=1).
6. Moler C. *Numerical Computing with MATLAB.* Philadelphia; 2004.
7. Hoelscher UC, Lothar S, Fidler F, Blaimer M, Jakob P. Quantification and localization of contrast agents using delta relaxation enhanced magnetic resonance at 1.5 T. *Magn Reson Mater Physics, Biol Med.* 2012;25(3):223-231. doi:10.1007/s10334-011-0291-6.
8. Dormand JR, Prince PJ. A reconsideration of some embedded formulae. *J Comput Appl Math.* 1986;15:203-211. doi:10.1016/0377-0427(86)90027-0.
9. Shampine LF, Reichelt MW. The MATLAB ODE Suite. *SIAM J Sci Comput.* 1997;18(1):1-22. doi:10.1137/S1064827594276424.

## Curriculum Vitae

**Name:** Daniel Martire

**Post-secondary Education and Degrees:**

Western University  
London, Ontario, Canada  
2016- Present  
M.Sc. Candidate, Physics

Western University  
London, Ontario, Canada  
2010- 2015  
B.Sc., Specialization in Physics

**Honours and Awards:**

Western Graduate Research Scholarship, Western University  
2016- Present

ISMIRM Educational Stipend  
2016- Present

Ontario Scholar  
2009

**Related Work Experience:**

Graduate Teaching Assistant, Nuclear Magnetic Resonance  
Physics and Astronomy, Western University, London, Ontario,  
Canada  
Supervisor: Dr. Blaine Chronik  
2016/9- 2016/12

Research Assistant  
Physics and Astronomy, Western University, London, Ontario,  
Canada  
2015/5- 2015/12

Undergraduate Research Student  
Physics and Astronomy, Western University, London, Ontario,  
Canada  
Thesis: *Characterization of Eddy-current Induced Vibration of  
Medical Devices in MRI*  
2014/5- 2014/8

Physics Intern  
 Global R&D, Lanxess Inc.  
 Western University Research Park, London, Ontario, Canada  
 2013/5- 2013/12

Summer Student  
 Meteor Group, Physics and Astronomy, Western University,  
 London, Ontario, Canada  
 2014/5- 2014/8

**Presentations:**

**Martire D.J.**, Peterson J.C., McCurdy C.M., Handler W.B., Chronik B.A. “Design of an MRI Gradient Field Exposure System for Medical Device Testing.” Abstract 4334, ISMRM 25<sup>th</sup> Annual Meeting, Honolulu, Hawaii, USA, (April 2017).

Tarapacki C.M., **Martire D.J.**, McCurdy C.M., Handler W.B., Chronik B.A. “Comparison of Laser Doppler Vibrometer and Accelerometer Measurements of MRI Gradient Field Induced Vibration in Conductive Materials.” Abstract 2621, ISMRM 25<sup>th</sup> Annual Meeting, Honolulu, Hawaii, USA, (April 2017).

**Martire D.J.**, Peterson J.C., McCurdy C.M., Handler W.B., Chronik B.A. “Design of a High dB/dt Pulsed Magnetic Field Generator for MRI Device Testing” London Health Research Day, London, Ontario, Canada, (March 2017).

**Martire D.J.**, Peterson J.C., McCurdy C.M., Handler W.B., Chronik B.A. “Audio-frequency dB/dt Exposure System for MRI-conditional Device Testing: A Design Study”. Imaging Network Ontario 15<sup>th</sup> Symposium, London, Ontario, Canada, (March 2017).

**Martire D.J.**, Wawrzyn K., Handler W.B., Chronik B.A. “Measuring Gradient-induced Vibration of a Conductive Device using Laser Doppler Vibrometry at 3T.” Abstract 3655, ISMRM 24<sup>th</sup> Annual Meeting, Suntec City, Singapore, (May 2016).

**Martire D.J.**, Wawrzyn K., Handler W.B., Chronik B.A. “Measuring Gradient-induced Vibration of Conductive Devices using Laser Doppler Vibrometry in a 3T MRI System.” London Health Research Day, London, Ontario, Canada, (April 2016).